Title
Electronic transport in atomically precise graphene nanoribbons

Author
Llinas, Juan Pablo

Publication Date
2020

Electronic transport in atomically precise graphene nanoribbons

By

Juan Pablo Llinas

A dissertation submitted in partial satisfaction of the

requirements for the degree of

Doctor of Philosophy

in

Engineering- Electrical Engineering and Computer Sciences

in the

Graduate Division

of the

University of California, Berkeley

Committee in charge:

Professor Jeffrey Bokor, Chair
Professor Ali Javey
Professor Michael Crommie

Spring 2020

Electronic transport in atomically precise graphene nanoribbons

Abstract

Electronic transport in atomically precise graphene nanoribbons

by

Juan Pablo Llinas

Doctor of Philosophy in Electrical Engineering and Computer Sciences

University of California, Berkeley

Professor Jeffrey Bokor, Chair

Advancements in on-surface materials synthesis have led to the development of atomically precise graphene nanoribbons (GNRs). Bottom-up synthesized GNRs have promising electronic properties for high performance field effect transistors (FETs) and ultra-low power devices such as tunneling FETs. However, the short length, wide band gap, and random orientation of GNRs have impeded the fabrication of devices with the expected performance and switching behavior. In this dissertation, progress towards integration of bottom-up synthesized GNRs into electronic devices is presented. The understanding of GNR growth and band structure is surveyed and analyzed with a focus on the implications on device yield and performance. The development of a device fabrication strategy for on-surface synthesized materials is shown, with a focus on the fabrication of high on-current and high on-off ratio 9-atom wide GNR FETs. Furthermore, device fabrication is developed for FETs with parallel arrays of GNRs transferred from single crystal Au(788), which greatly improves device yield. Finally, theoretical charge transport in GNR heterostructures is employed to demonstrate exotic device behavior such as ultra-sharp switching and negative differential resistance. The path towards state-of-the-art GNR-based logic circuits is charted in this work.

This work is dedicated to my mother, Nilsa Mesa.

Contents

1 Introduction 1

- 1.1 Electronic structure of graphene, carbon nanotubes, and graphene nanoribbons 1
- 1.2 Field-effect transistors with 1-dimensional semiconductors 3
- 1.3 Dissertation organization 4
- 1.4 References 4

2 Bottom-up chemical synthesis of graphene nanoribbons 6

- 2.1 GNR precursor 8
- 2.2 Growth surface 10
- 2.3 Polymerization dynamics and improving length distribution 11
- 2.4 Solution synthesis 13
- 2.5 Growth of GNR heterostructures 14
- 2.6 Conclusions 15
- 2.7 References 16

3 GNR transfer and device fabrication 18

- 3.1 Optical lithography of the device substrate 18
- 3.2 GNR transfer 20
- 3.3 Electron beam lithography 21
- 3.4 Conclusion 22
- 3.5 References 22

4 Band gap of graphene nanoribbons 24

- 4.1 Scanning Tunneling Spectroscopy 24
- 4.2 First principles calculations 25
- 4.3 Photoluminescence-emission spectroscopy of solution GNRs 27
- 4.4 Resonant Raman spectroscopy of 7AGNRs 29
- 4.5 Conclusion 32
- 4.6 References 32

5 Field effect transistors with atomically precise armchair graphene nanoribbons 34

- 5.1 Fabrication of FETs with 50 nm back gates 35

5.2 9AGNRFET and 13AGNRFET characteristics and contact analysis........................37
5.3 Improving transmission across Schottky barrier via efficient electrostatic gating ..40
5.4 Device yield and variability..41
5.5 Conclusion 43
5.6 References...43
6 Field effect-transistors with dense, aligned graphene nanoribbons.............................46
6.1 Aligned GNR transfer and device fabrication...46
6.2 Transfer characteristics of FETs with parallel arrays of 7AGNRs.......................48
6.3 Transfer characteristics of 9AGNR and 5AGNRFETs 49
6.4 Device yield and variability modeling..51
6.5 Conclusion 53
6.6 References...54
7 Towards high performance FETs: narrow band gap graphene nanoribbons...............55
7.1 Band gap engineering using topological protected states in GNRs 55
7.2 Field-effect transistors with a TE-GNR 57
7.3 TE-GNR FETs..58
7.4 Conclusion 60
7.5 References...60
8 Super-lattice graphene nanoribbon field effect transistors 62
8.1 Band structure of SL-GNRs...63
8.2 Atomistic calculations of a SL-GNR FET 64
8.3 Analytical transport model using Landauer formalism 66
8.4 Bistable inverter with SL-GNR FETs 72
8.5 Requirements for experimental demonstration of SL-GNR FETs.........................73
8.6 Conclusion 73
8.7 References...74
9 Conclusion 75

Table of figures

Figure 1.1 | Band structure of graphene and CNTs. 2
Figure 1.2 | Transport in p-type GNR Schottky barrier transistors. 3
Figure 2.1 | Top-down patterning of GNRs. 6
Figure 2.2 | Bottom-up chemical synthesis of 7AGNRs. 7
Figure 2.3 | Bond-length resolution images with non-contact AFM. 8
Figure 2.4 | Various GNR precursors and the resulting GNR structure. 9
Figure 2.5 | Aligned 7AGNRs on Au(788). 10
Figure 2.6 | 5AGNRs grown on Au(111). 11
Figure 2.7 | Length distribution from a typical GNR growth and device yield. 12
Figure 2.8 | Improving GNR length by replacing the halogen in the precursor molecule. 13
Figure 2.9 | Solution synthesis of chevron type GNR. 14
Figure 2.10 | STM of 7-13 AGNR heterostructures. 15
Figure 3.1 | Fabrication of local back gate GNR FET. 19
Figure 3.2 | GNR transfer from Au/mica onto an arbitrary substrate. 20
Figure 3.3 | Raman spectrum of 9AGNRs before and after transfer. 21
Figure 3.4 | Micrograph of electrode pair patterned with electron beam lithography. 22
Figure 4.1 | Tight binding and DFT-LDA gaps. 26
Figure 4.2 | DFT-GW calculation of GNRs in vacuum. 27
Figure 4.3 | Photoluminescence-emission spectroscopy of a CNT ensemble. 28
Figure 4.4 | Photoluminescence-emission spectroscopy of cGNRs. 29
Figure 4.5 | GNR degradation during Raman acquisition. 30
Figure 4.6 | Resonant Raman spectroscopy of 7AGNRs. 31
Figure 4.7 | Resonant Raman spectroscopy of 9AGNRs. 32
Figure 5.1 | High resolution STM GNR characterization and FET structure. 34
Figure 5.2 | Raman spectra of as-grown GNRs and after transfer. 36
Figure 5.3 | Transfer characteristics of FETs with 9AGNRs and 13AGNRs. 37
Figure 5.4 | Cumulative distribution function (CDF) of GNRFET I_{on}. 38
Figure 5.5 | Band diagram comparing devices with different gate oxide thickness. 40
Figure 5.6 | Ionic liquid gating of a 9AGNRFET at room temperature. 40
Figure 5.7 | Transfer characteristics of a scaled, high performance 9AGNRFET. 41
Figure 6.1 | Aligned GNR bubble transfer and Raman spectroscopy. 47
Figure 6.2 | Transfer characteristics of FETs with aligned 7AGNRs. 48
Figure 6.3 | STM of 5AGNRs grown on Au(111) and Au(788). 49
Figure 6.4 | I_d-V_g characteristics of FETs with aligned 5AGNRs. 50
Figure 6.5 | I_d-V_g characteristics of a FET with aligned 9AGNRs. 51
Figure 6.6 | Statistics of aligned 5AGNR and 9AGNR FETs. 52
Figure 6.7 | Monte Carlo calculation of device yield with aligned GNRs. 53

Figure 7.1 | STM of topically engineered GNRs. 56
Figure 7.2 | TE-GNR STM and Raman spectroscopy for device fabrication. 58
Figure 7.3 | TE-GNRFET transport characteristics. 59
Figure 7.4 | Chemical passivation of TE bands. 60
Figure 8.1 | 7-13-7 AGNR quantum dot. 63
Figure 8.2 | Chevron GNR band structure. 64
Figure 8.3 | DOS and device structure of a chevron GNR FET calculated via NEGF. 65
Figure 8.4 | NEGF calculation of transfer curves of chevron GNRFET. 66
Figure 8.5 | Top of the barrier model band diagram. 67
Figure 8.6 | Ballistic conduction through finite and infinite bandwidth at 0 K. 68
Figure 8.7 | Validation of analytical transport model of SLFET. 69
Figure 8.8 | Band diagrams of SL-GNRFET with B-doped 7AGNRs. 70
Figure 8.9 | Transfer characteristics of B-doped 7AGNR SL-FET from analytical model. 71
Figure 8.10 | SL-FET inverter transfer curves from compact model. 72
Figure 8.11 | SL-FET structure for experimentally demonstrating NDR and sharp switching. 73

Acknowledgments

First, I would like to thank my PhD advisor, Jeff Bokor, for support, mentorship, and for giving me the freedom to work on challenging and rewarding projects. I have grown tremendously as a scientist and as a person due to my excellent graduate school experience in the Bokor group.

The work presented here is the result of a large, international collaboration, and I am fortunate to call many of the people involved friends, colleagues, and mentors. I would like to thank Prof. Roman Fasel, Prof. Michael Crommie, and Prof. Felix Fischer for advice, materials, and for spearheading major advancements that enabled this thesis to be possible. The students, post-docs, and research scientists in their groups were a joy to work with and to learn from. It is a long list that includes Dr. Gabriela Borin Barin, Dr. Zahra Pedramrazi, Dr. Andrew Fairbrother, Dr. Chen Chen, and Dr. Akimitsu Narita. I would also like to thank my mentees Rohit Braganza and Ailin Chen for all their contributions and curiosity.

I would like to thank Prof. Ali Javey for chairing my qualifying exam committee and for giving me the opportunity to be a graduate student instructor for his course, EE 143.

To the members of the Bokor group and fellow graduate students, thank you for the thoughtful discussions, advice, and necessary distractions. In particular, I want to thank the Bokor group members Ms. Charlotte Jones, Dr. Zafer Mutlu, Dr. Kyunghoon Lee, Dr. Shuang Wu, Dr. Maite Goire, and Akshay Pattabi. To my wonderful mentors including Dr. Feifei Lian, Dr. Patrick Bennett, and Dr. François Léonard, who have provided me much scientific and life guidance over the years, thank you for your support and patience.

I want to thank the National Science Foundation, Berkeley Fellowship, and Office of Naval Research for their generous contributions to my research and to my career. To the staff of the labs and offices I worked in, including the staff of Berkeley EECS, Berkeley Nanolab, the Molecular Foundry, Stanford cleanrooms, and Sutardja-Dai Hall, thank you for your tireless efforts in keeping the programs and labs running as smoothly as possible.

I want to also thank my friends, family, and loved ones for all their support throughout my academic career. I will be eternally thankful to my mom, Nilsa Mesa, whose sacrifice made my career possible.

1 Introduction

Technological advancement in society has been predicated on the continuous scaling of silicon-based computing systems. Many challenges to continue the scaling trends have been met with ingenious solutions such as integration of high-k dielectrics with metal gates, non-planar multi-gate device structures, and strained semiconducting channels. Still, current silicon scaling developments are providing diminishing returns in cost and performance. This has motivated the exploration of alternative material systems that could be used to redesign the logic transistor and carry on with scaling. Carbon nanotubes (CNTs) are one of the most promising candidates to replace the silicon channel sub-10nm gate length devices, exhibiting high performance and excellent switching behavior owed to both the quasi-ballistic charge transport in the CNT at room temperature and its ultra-thin body (~1 nm)[1]. However, CNT growth for device fabrication is a top-down technique, where a particular growth yields an ensemble of CNT diameters that affect device to device variability[2]. The variation in device performance caused by the lack of control of the CNT molecular structure is so severe that it nullifies the performance benefits CNTs could provide over silicon. In contrast, graphene nanoribbons (GNR), can be grown with molecular precision via a bottom-up chemical synthesis technique[3–6], and provide a platform for minimizing device variability that arises from variations in material structure as well as enabling the creation of one dimensional semiconducting heterostructures at the nanoscale[7,8].

Bottom-up synthesized GNRs and GNR heterostructures have promising electronic properties for high performance field effect transistors (FETs)[9] and ultra-low power devices such as tunnelling FETs[10]. The electronic, optical and magnetic properties of GNRs can be engineered by varying their width and edge structure[11,12]. However, traditional methods to pattern GNRs, such as unzipping carbon nanotubes or lithographically defining GNRs from bulk graphene, yield GNRs with rough edges that degrade electronic transport[13]. Recent experiments have demonstrated bottom-up chemical synthesis of GNRs with uniform width and atomically-precise edges, in which the width and edge structure of the GNR is determined by the oligophenylene used in the polymerization step[3–6]. This synthetic uniformity produces GNRs with high structural and electronic homogeneity, which is required for integration of GNRFETs into large-scale digital circuits[14].

1.1 Electronic structure of graphene, carbon nanotubes, and graphene nanoribbons

Graphene is an isolated two dimensional layer of graphite, where the carbon atoms sit in a hexagonal honeycomb lattice. The carbon atoms bond via sp^2 hybridization, resulting in delocalized electrons in the overlapping p_z orbitals. The band structure arising from these states can be calculated with a simple, two element, tight binding calculation. As shown in Figure 1.1, the band structure of graphene near conduction band minimum forms two Dirac cones with linear dispersion relation near the Fermi level. The linear dispersion relation gives graphene its intriguing electronic properties since electrons behave like relativistic particles at low excitation energies. In fact, extremely high mobilities of $>10^6$ cm^2/Vs have been measured in graphene devices[15]. For logic devices, the high-current capabilities of graphene would translate to faster circuits. However, the lack of band gap in graphene is problematic for logic since it will cause yield devices with poor current on-off ratio. To open a band gap in graphene while maintaining some of its great conductive properties, charge carriers in graphene can be confined into a one dimensional structures such as CNTs or GNRs.

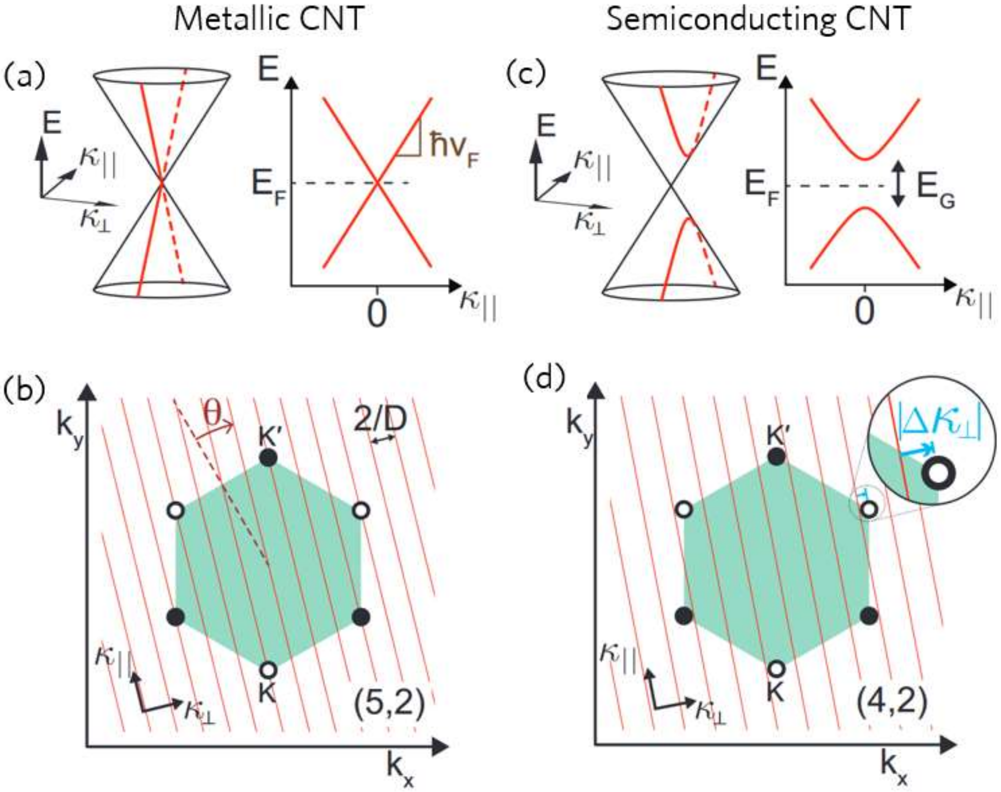

Figure 1.1 | Band structure of graphene and CNTs. The band structure of graphene (left a,c) is dissected into a series of one dimensional sub-bands in a CNT (b,d) by the wave-vector planes defined by the chirality. The CNT band gap (right a,c) is determined by the intersection of the wave-vector plane closest to the Dirac point, with metallic CNTs having the plane intersect exactly at the Dirac point[16].

In both semiconducting CNTs and GNRs, the band gap is a result of the boundary conditions to the electronic wavefunction introduced by the confinement[16]. For instance, rolling graphene into a CNT forces the electronic wavefunction to be periodic along the CNT circumference. In the band structure, the boundary condition translates to intersecting the graphene band structure with a plane in the *E-k* space, as shown in Figure 1.1, where the orientation of the plane depends on the chirality of the CNT. If the chirality of the CNT is such as the *E-k* introduced by the boundary conditions crosses the Dirac point of the graphene, the CNT is metallic (e.g. armchair CNTs). For other CNTs, the plane intersects away from the Dirac point and the band structure is defined by the intersecting curves with a band gap depending on the chirality. The sensitivity of the CNT band gap on the chirality is what poses a major challenge for integration into systems with a billion transistors. In a collection of CNTs with a uniform chirality distribution, a third of the CNTs would be metallic. Even with advancements in purification techniques, small variations in chirality can cause large variations in device characteristics[2]. Bottom-up synthesized GNRs can be thought as analogous to CNTs with a prescribed chirality. The band gap in GNRs also arises from the confinement and will be discussed in detail in Chapter 2. In contrast to graphene FETs, devices with CNTs and GNRs both show the high on-off ratios required for logic circuits.

1.2 Field-effect transistors with 1-dimensional semiconductors

A common transistor geometry with 1-dimensional semiconductors, such as CNTs or GNRs, involves placing the material on an insulator, contacting with metal electrodes, and gating with either a back gate or a top gate separated by an insulator[17]. A back gated GNRFET is shown in Figure 1.2. These devices are typically p-type Schottky barrier (SB) FETs, where the gate modulates the SB at the source-side contact and the device turns on for negative gate voltages. In the off-state, the source-side barrier blocks carriers from transmitting to the drain. As the gate is biased to the on-state, the barrier decreases and the carriers and transport across the channel. The on-state current roughly corresponds to the logic circuit speed and the on-off ratio corresponds to the power dissipation in the circuit (higher on-off ratio leads to lower power dissipation). A sub-10 nm channel length device with high on-current and on-off ratio and a small total footprint is desired to be competitive with state-of-the-art silicon technology[14].

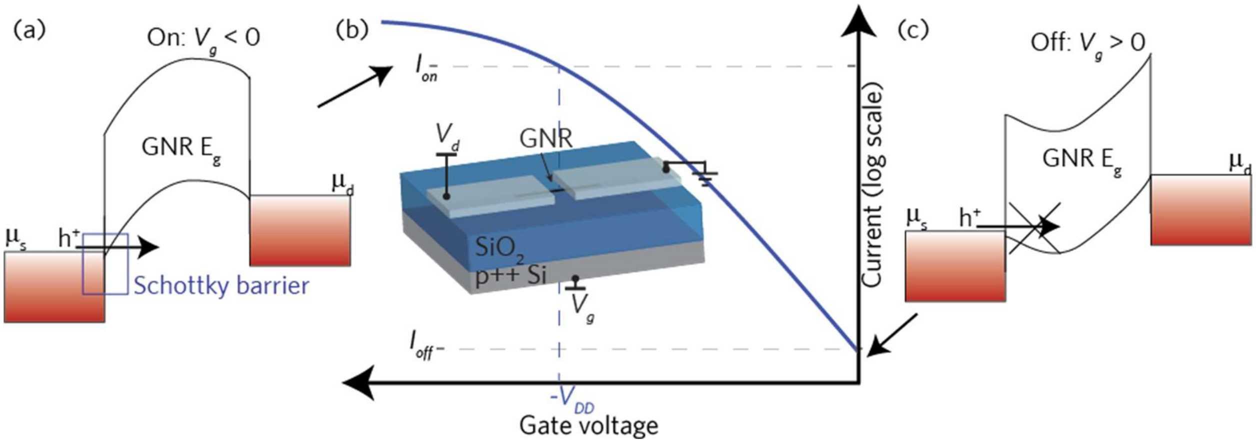

Figure 1.2 | Transport in p-type GNR Schottky barrier transistors. (a,c) Band diagram of (b inset) back gated device structure in the on-state and off-state respectively. (b) sketches the current versus gate voltage characteristics for such a device.

Given the ultra-thin body nature of CNTs and GNRs, the gate can efficiently modulate the potential of the channel even for short channel lengths. In fact, remarkable switching characteristics have been measured in CNTs with channel lengths <10 nm long[1]. One of the common limiting factors in the device performance is the SB height. A wide band gap semiconductor allows for a low-off current, but charge carriers must overcome a large SB at the source-side contact. This remains a challenge in GNR devices and will be discussed at length in this work.

1.3 Dissertation organization

This dissertation investigates the electrical transport and optical properties of self-assembled GNRs and GNR heterojunctions via device measurements, optical spectroscopy, and theoretical calculations for the development of high-performance and exotic electronic devices. Ultra-narrow GNRs are synthesized and integrated into device structures that enable the study of the all-important electrical contact to the GNR. By considering the limiting factors of the contact efficiency, the highest performance bottom-up synthesized GNRFETs to date are demonstrated. Finally, theoretical predictions of novel devices integrating GNR heterostructures are presented.

Chapter 2 discusses each step in the bottom-up synthesis growth of atomically precise GNRs on surfaces and in solution. Chapter 3 reports the baseline GNR device fabrication process used in this work. In Chapter 4, the band structure of ultra-narrow GNRs is discussed, surveying the various experimental and theoretical techniques that probe the GNR band gap and explaining the discrepancy in the band gap values. High-current GNRFETs with 9AGNRs and thin, high-k dielectrics are demonstrated and analysed in Chapter 5. In Chapter 6, aligned GNRs are grown on stepped Au surfaces, transferred, and contacted. Device data of aligned 5AGNR, 7AGNR, and 9AGNR devices is analysed and compared. Chapter 7 describes a novel way of engineering the band structure of GNRs by introducing chains of topologically protected states. Devices with one of these GNRs are reported and the prospect of integrating these materials into devices is discussed. In Chapter 8, a compact model for the transport of ballistic superlattice GNRs is reported with validation from atomistic calculations, and the requirements for experimental demonstration of superlattice GNR devices is discussed. Finally, Chapter 9 summarizes the work and discusses future directions.

1.4 References

1. Franklin, A. D., Luisier, M., Han, S.-J., Tulevski, G., Breslin, C. M., Gignac, L., Lundstrom, M. S. & Haensch, W. Sub-10 nm Carbon Nanotube Transistor. *Nano Lett.* **12,** 758–762 (2012). https://doi.org/10.1021/nl203701g
2. Tulevski, G. S., Franklin, A. D., Frank, D., Lobez, J. M., Cao, Q., Park, H., Afzali, A., Han, S.-J., Hannon, J. B. & Haensch, W. Toward High-Performance Digital Logic Technology with Carbon Nanotubes. *ACS Nano* **8,** 8730–8745 (2014). https://doi.org/10.1021/nn503627h
3. Cai, J., Ruffieux, P., Jaafar, R., Bieri, M., Braun, T., Blankenburg, S., Muoth, M., Seitsonen, A. P., Saleh, M., Feng, X., Müllen, K. & Fasel, R. Atomically precise bottom-up fabrication of graphene nanoribbons. *Nature* **466,** 470–473 (2010). https://doi.org/10.1038/nature09211

4. Chen, Y.-C., de Oteyza, D. G., Pedramrazi, Z., Chen, C., Fischer, F. R. & Crommie, M. F. Tuning the Band Gap of Graphene Nanoribbons Synthesized from Molecular Precursors. *ACS Nano* **7,** 6123–6128 (2013). https://doi.org/10.1021/nn401948e

5. Ruffieux, P., Wang, S., Yang, B., Sánchez-Sánchez, C., Liu, J., Dienel, T., Talirz, L., Shinde, P., Pignedoli, C. A., Passerone, D., Dumslaff, T., Feng, X., Müllen, K. & Fasel, R. On-surface synthesis of graphene nanoribbons with zigzag edge topology. *Nature* **531,** 489–492 (2016). https://doi.org/10.1038/nature17151

6. Kimouche, A., Ervasti, M. M., Drost, R., Halonen, S., Harju, A., Joensuu, P. M., Sainio, J. & Liljeroth, P. Ultra-narrow metallic armchair graphene nanoribbons. *Nat Commun* **6,** 10177 (2015). https://doi.org/10.1038/ncomms10177

7. Chen, Y.-C., Cao, T., Chen, C., Pedramrazi, Z., Haberer, D., Oteyza, D. G. de, Fischer, F. R., Louie, S. G. & Crommie, M. F. Molecular bandgap engineering of bottom-up synthesized graphene nanoribbon heterojunctions. *Nat Nano* **10,** 156–160 (2015). https://doi.org/10.1038/nnano.2014.307

8. Cai, J., Pignedoli, C. A., Talirz, L., Ruffieux, P., Söde, H., Liang, L., Meunier, V., Berger, R., Li, R., Feng, X., Müllen, K. & Fasel, R. Graphene nanoribbon heterojunctions. *Nat Nano* **9,** 896–900 (2014). https://doi.org/10.1038/nnano.2014.184

9. Luisier, M., Lundstrom, M., Antoniadis, D. A. & Bokor, J. Ultimate device scaling: Intrinsic performance comparisons of carbon-based, InGaAs, and Si field-effect transistors for 5 nm gate length. in *Electron Devices Meeting (IEDM), 2011 IEEE International* 11.2.1-11.2.4 (2011). https://doi.org/10.1109/IEDM.2011.6131531

10. Zhao, P., Chauhan, J. & Guo, J. Computational Study of Tunneling Transistor Based on Graphene Nanoribbon. *Nano Lett.* **9,** 684–688 (2009). https://doi.org/10.1021/nl803176x

11. Nakada, K., Fujita, M., Dresselhaus, G. & Dresselhaus, M. S. Edge state in graphene ribbons: Nanometer size effect and edge shape dependence. *Phys. Rev. B* **54,** 17954–17961 (1996). https://doi.org/10.1103/PhysRevB.54.17954

12. Yang, L., Park, C.-H., Son, Y.-W., Cohen, M. L. & Louie, S. G. Quasiparticle Energies and Band Gaps in Graphene Nanoribbons. *Phys. Rev. Lett.* **99,** 186801 (2007). https://doi.org/10.1103/PhysRevLett.99.186801

13. Yoon, Y. & Guo, J. Effect of edge roughness in graphene nanoribbon transistors. *Applied Physics Letters* **91,** 073103 (2007). https://doi.org/10.1063/1.2769764

14. Franklin, A. D. Electronics: The road to carbon nanotube transistors. *Nature* **498,** 443–444 (2013). https://doi.org/10.1038/498443a

15. Wang, L., Meric, I., Huang, P. Y., Gao, Q., Gao, Y., Tran, H., Taniguchi, T., Watanabe, K., Campos, L. M., Muller, D. A., Guo, J., Kim, P., Hone, J., Shepard, K. L. & Dean, C. R. One-Dimensional Electrical Contact to a Two-Dimensional Material. *Science* **342,** 614–617 (2013). https://doi.org/10.1126/science.1244358

16. Laird, E. A., Kuemmeth, F., Steele, G. A., Grove-Rasmussen, K., Nygård, J., Flensberg, K. & Kouwenhoven, L. P. Quantum transport in carbon nanotubes. *Rev. Mod. Phys.* **87,** 703–764 (2015). https://doi.org/10.1103/RevModPhys.87.703

17. Llinas, J. P., Fairbrother, A., Barin, G. B., Shi, W., Lee, K., Wu, S., Choi, B. Y., Braganza, R., Lear, J., Kau, N., Choi, W., Chen, C., Pedramrazi, Z., Dumslaff, T., Narita, A., Feng, X., Müllen, K., Fischer, F., Zettl, A., Ruffieux, P., Yablonovitch, E., Crommie, M., Fasel, R. & Bokor, J. Short-channel field-effect transistors with 9-atom and 13-atom wide graphene nanoribbons. *Nature Communications* **8,** 633 (2017). https://doi.org/10.1038/s41467-017-00734-x

2 Bottom-up chemical synthesis of graphene nanoribbons

The interest of opening the band gap in graphene quickly led to the fabrication of the first GNRs from bulk sheets of graphene or from CNTs. These GNRs were fabricated by either etching a bulk sheet of graphene down to thin strips or unzipping carbon nanotubes. While such "top-down" methods were successful at yielding semiconducting material, charge transport was hindered by the variation in width and edge structure along the GNRs as shown in Figure 2.1. The electronic structure and charge transport is so sensitive to the GNR structure, that even a few missing carbon atoms or adding an extra hydrogen atom at the end a ~10 nm long GNR would completely change the electronic properties[1,2]. Addressing the lack of atomic control in the GNR would require a new fabrication technique that was developed in 2010. As shown in Figure 2.2, the technique yields GNRs with atomically precise edges and a uniform width along the ribbon which can be characterized with high resolution scanning tunnelling microscopy (STM). This chapter will discuss the details of the on-surface and solution grown GNRs and the recent advancements in the growth of GNRs with various electronic properties.

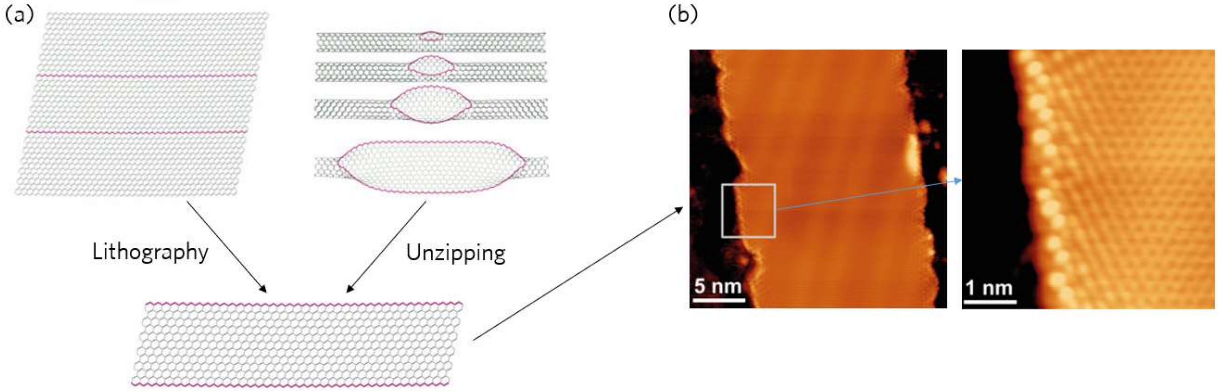

Figure 2.1 | Top-down patterning of GNRs. (a) GNRs from lithography of bulk graphene and unzipping of CNTs[3]. (b) Scanning tunnelling microscopy image of a GNR from an unzipped CNT. Unzipping of GNRs causes rough edges that affect the electronic structure and degrade transport[4].

The on-surface synthesis of GNRs starts in the synthetic chemistry lab, where a carefully chosen monomer is synthesized and purified. The monomer powder is then brought into an ultra-high vacuum (UHV) STM chamber where a metal crystal (or film) is cleaned to obtain an atomically smooth metal surface (typically Au(111)). The monomer is evaporated onto the metal surface and annealed, where it radicalizes from dehalogenation. Monomers diffuse along the surface and bond with each other to form polymers as shown in Figure 2.2. With another annealing step at a higher temperature, the polymers go under a process called cyclodehydrogenation. The polymer cyclizes into a flat, atomically smooth GNR by losing some of its hydrogens and forming new C-C bonds. This completes the synthesis. After this stage, various methods are used to characterize the GNR in-situ, such as STM, scanning tunnelling spectroscopy (STS), and non-contact atomic force microscopy (nc-AFM).

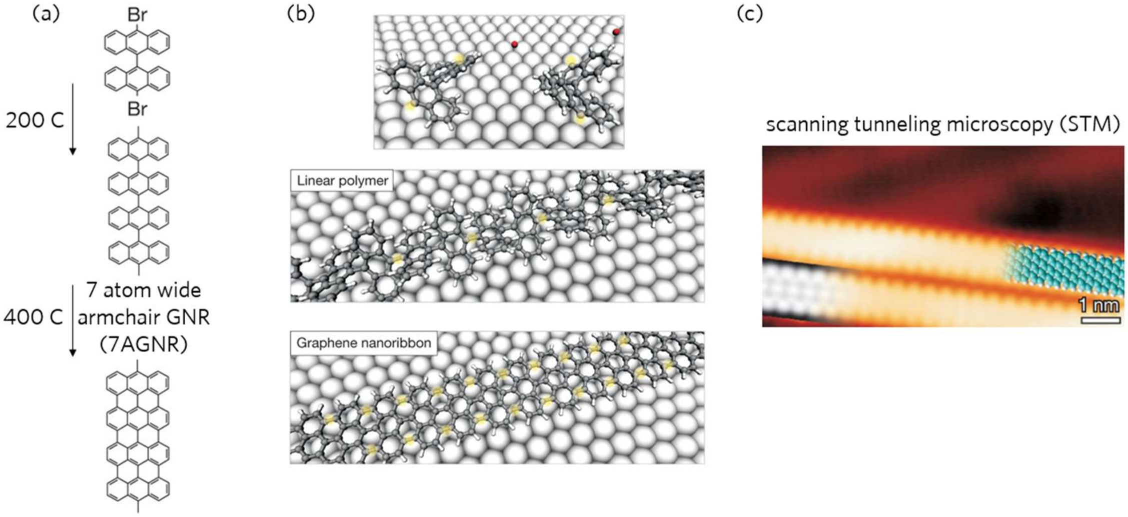

Figure 2.2 | Bottom-up chemical synthesis of 7AGNRs. (a) GNR precursor (DBBA) is evaporated onto the Au surface, annealed to create a linear polymer, and annealed further to finalize the GNR synthesis with cyclodehydrogenation. (b) 3D rendering of growth process on the Au surface. (c) High resolution STM image of 7AGNRs showing uniform length and smooth, armchair edges[5].

Since this process is performed under UHV conditions in a STM chamber, the sample can be cooled down after each step and a high resolution STM image can be obtained as shown in Figure 2.2**.** The edge structure and uniformity of the GNR is determined from the image. But to prove that the GNR has the expected semiconducting density of states, STS is performed, which will be discussed in Chapter 4. Some UHV systems used are equipped with a nc-AFM set-up which takes images with remarkable bond-length resolution[6]. These images are more challenging to obtain than typical STM images, but the payoff is clear proof that the GNR has the expected molecular structure, as shown in the 9AGNRs in Figure 2.3**.**

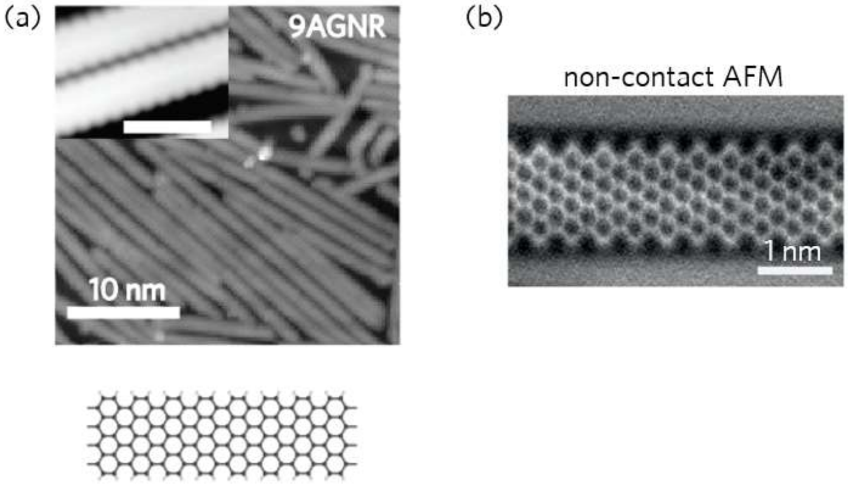

Figure 2.3 | Bond-length resolution images with non-contact AFM. (a) Room temperature STM of 9AGNRs on Au(111). (b) non-contact AFM on 9AGNRs on Au(111) showing the pristine 9AGNR structure[6].

After the 2010 report of the first bottom-up synthesized GNR, many research groups around the world raced to synthesize bottom-up GNRs as a platform for the study of novel physics and chemistry or for integration in practical applications, such as FETs for logic systems. However, not every monomer designed in the chemistry lab can be synthesized. Even if the monomer is synthesized, the monomer may not behave as expected under UHV or on a surface and may not grow GNRs. Finally, on-surface synthesis grows GNRs that are limited in length, which can hinder the development of GNR devices. This led to the development of solution based GNR growth.

2.1 GNR precursor

The chemical and physical properties of the monomer dictate whether the GNR growth will be successful and what the resulting molecular structure of the GNR. Therefore, it has been a focus to understand the synthesis of monomers that produce GNRs and the types of GNRs that these monomers yield. This quest to build a monomer:GNR "library" is key for studying novel physics with the GNRs as a platform and for the development of high-performance GNR devices. For example, Figure 2.4 shows the first set of synthesized GNRs from monomers: 10,10'-dibromo-9,9'-bianthryl (DBBA) which yields 7-atom wide armchair GNR (7AGNR) and 6,11-dibromo-1,2,3,4-tetraphenlytriphenylene which yields the chevron GNR.

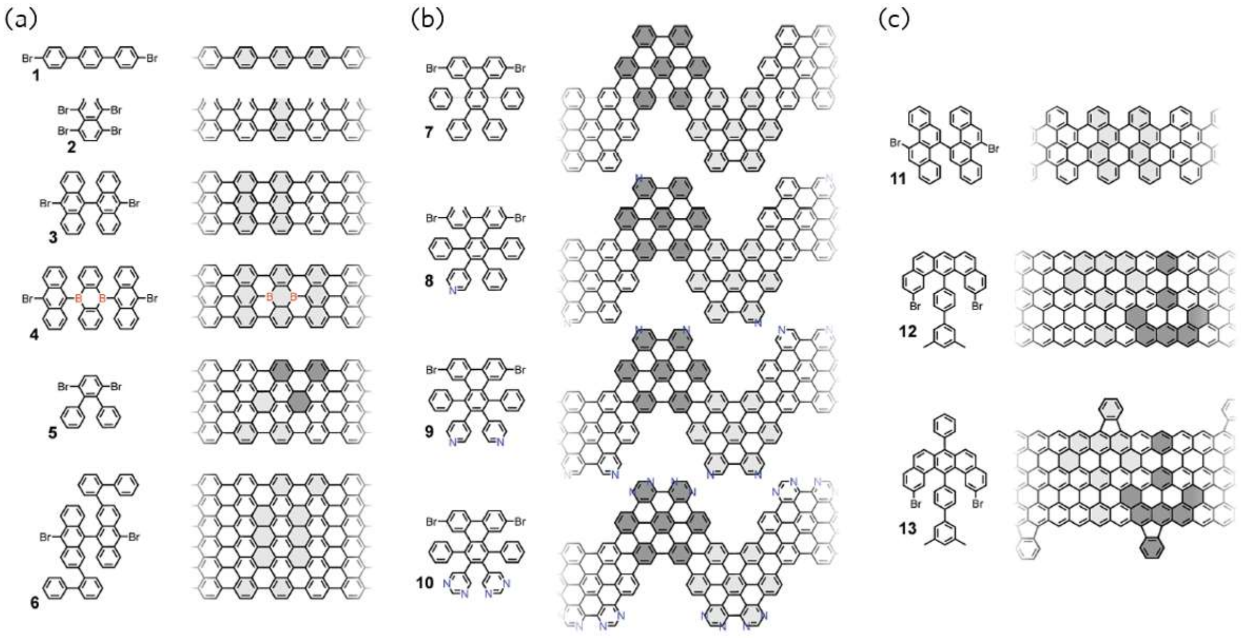

Figure 2.4 | Various GNR precursors and the resulting GNR structure. (a) Armchair GNRs 3, 5, 7, 7 (B-doped), 9, 13 atoms wide. (b) Chevron-type GNRs with different nitrogen doping configurations on the edges. (c) Zigzag-like edged GNRs[7].

While many different types of GNRs have been successfully synthesized using this technique, there is a collection of potential GNR precursors that never grew any GNRs for various reasons: First, after a candidate precursor is designed, it must be chemically synthesized. The fabrication of some monomers requires multiple, challenging steps in their synthesis that can inhibit their yield and final purification (i.e. not any monomer can be practically synthesized). Milligrams of precursor material must be realized for the development of the on-surface GNR growth in UHV. Second, the precursors must sublime at moderate temperatures (~200 C) under UHV conditions without decomposing. Third, the monomer must land on the surface so that the reactive sites where the halogen (Cl or I) sites line up as the monomer diffuses on the surface. If the halogen sites of two monomers do not line up, the monomers may physically approach while diffusing on the surface but will not polymerize due to misalignment of the reactive sites, also known as steric hindrance. Fourth, the halogen must cleave off the monomer (dehalogenation) at a temperature lower than cyclodehydrogenation (otherwise diffusivity goes to zero before the monomer can polymerize) and the monomer must have some diffusivity on the surface at the dehalogenation temperature. Ideally the cyclodehydrogenation temperature is much larger than dehalogenation temperature so that the polymerization is not prematurely stopped by the cyclodehydrogenation[8].

Once the monomer is on the surface, the temperatures of the dehalogenation, polymerization, and cyclodehydrogenation must be low enough for the growth to occur without desorption or decomposition of the monomer molecules. The temperatures required for growth are mediated by the monomer's interaction with the surface. Therefore, the choice of surface can determine whether the GNR grows, with metals being the most commonly used surface due to their catalytic properties and the ability to perform STM on them.

2.2 Growth surface

Different metal surfaces have been used for the growth of GNRs. The metal plays a critical role in the growth by (1) efficiently adsorbing the precursor molecule, (2) catalyzing the dehalogenation, (3) promoting surface diffusion of the monomers (templating the growth), and (4) catalyzing the cyclodehydrogenation. Growths have been demonstrated on various metal surfaces. Most notably, the low cost, wide availability, and favorable surface properties for GNR growth of Au(111) has made it the metal of choice for most GNR growths. The Au(111) promotes the growth of randomly oriented GNRs but Au can be engineered to template aligned growth. A stepped, Au(788), surface can be obtained from a mis-cut single crystal Au to template the growth of aligned GNRs[9], as shown in Figure 2.5.

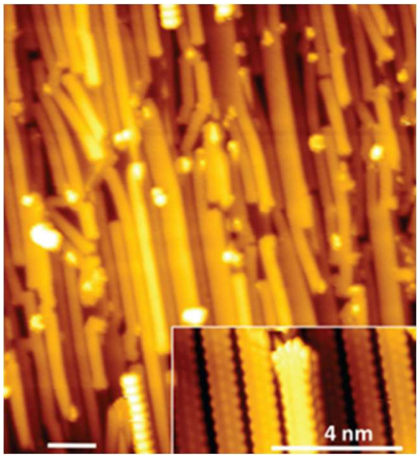

Figure 2.5 | Aligned 7AGNRs on Au(788). STM of templated, aligned 7AGNR growth on Au(788)[9].

The availability of Au(111) thin films on Mica allows for growth on the sacrificial Au that can be exploited for transfer to an insulating material, a critical step in device fabrication as described in Chapter 5. Growing GNRs on an insulating surface has attracted attention over the years because it would enable direct device fabrication on the growth surface, limiting the possibility of GNR damage during the metal to insulator layer transfer.

Growth on insulators has yet to be demonstrated, and it continues to be an active area of research. Metals provide plenty of electrons that can promote the dehalogenation and cyclodehydrogenation. Without all those free electrons on an insulator surface, the design of the monomer should allow the dehalogenation to happen at a reasonable temperature (~200 C), because molecules adhere less readily to the insulating surface causing the desorption temperature of the molecules to drop significantly when compared to molecules sitting on metal. Furthermore, cyclodehydrogenation temperature needs to be low without the presence of the metallic substrate.

One strategy is to design the growth to avoid cyclodehydrogenation all-together, by growing a monomer that polymerizes already conjugated, as some 5-atom wide GNRs (5AGNR)[10] grow as shown in Figure 2.6. Even though there has been limited progress on growth on insulators, there has been progress on understanding the growth kinetics on the surface which correlates to GNR length.

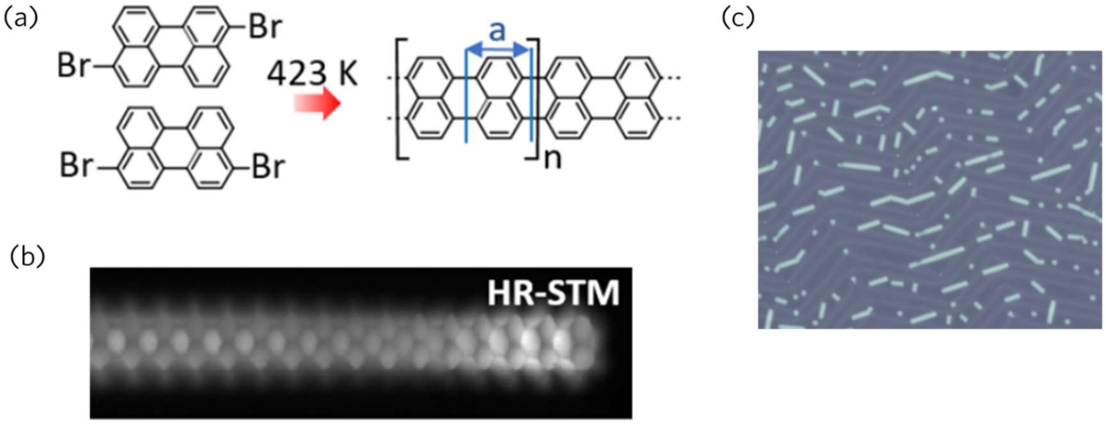

Figure 2.6 | 5AGNRs grown on Au(111). (a) Synthesis of the GNRs using the 5AGNR precursor. A single annealing step is needed since it polymerizes already planarized. (b) High resolution STM of 5AGNRs grown and (c) High field of view STM image of 5AGNRs. The ribbons appear to grow aligned along the herringbone reconstruction of the Au(111) surface[2].

2.3 Polymerization dynamics and improving length distribution

Long GNRs (>100 nm) enable in-depth studies of the intrinsic GNR charge transport and facilitate the integration of GNR devices into circuits. The yield of working GNR devices increases dramatically as the average GNR length increases, as shown in Figure 2.7. However, bottom-up GNR synthesis yields GNRs with lengths on the order of 10s of nanometers. The quality of the precursor used and the growth dynamics on the surface inhibit the growth of long GNRs. If the precursor molecules are not pure after isolation, there may be monomers on the surface with only one halogen. The polymerization ends once the defective monomer reacts. Therefore, purifying the precursor after synthesis as much as possible is critical in optimizing the length distribution of the GNRs.

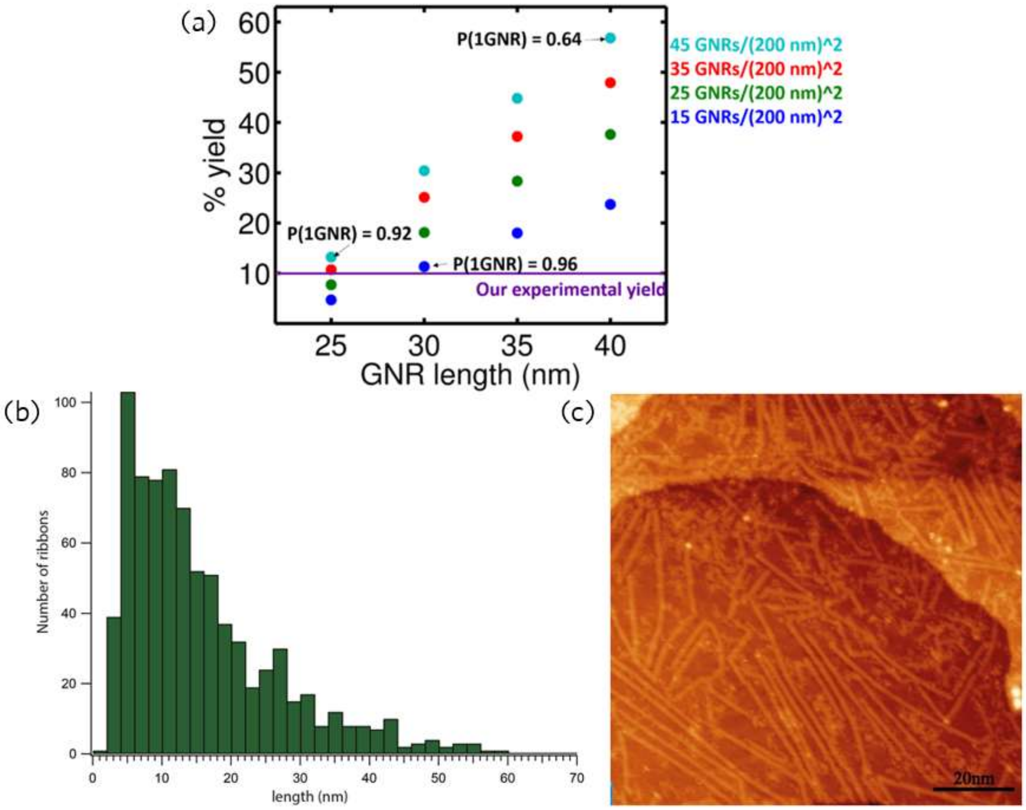

Figure 2.7 | Length distribution from a typical GNR growth and device yield. (a) Calculated device yield rises dramatically as GNR length increases. (b) Experimental length distribution of 9AGNRs grown on Au(111) using room temperature STM images like the one shown in (c).

To further optimize GNR length, passivation of the precursor molecules during polymerization must be minimized. Ideally, polymerization occurs without passivation of the reactive sites in the monomers. Remnant hydrogen or other unwanted species in the UHV chamber can limit polymer length by passivating the radicals[11]. One proposed approach to minimize this effect is to introduce a hydrogen getter, such as Ti or Co, near the growth surface to decrease the hydrogen concentration. But improving GNR length by lowering hydrogen partial pressure has yet to be demonstrated. A proven approach to improve length distribution is to separate the temperatures of polymerization and cyclodehydrogenation[8].

GNR length can be somewhat improved by optimizing the parameters in the growth (temperatures and times of sublimation, polymerization, cyclodehydrogenation)[11]. The stochastic nature of polymerization and cyclodehydrogenation leads to a non-negligible amount of cyclodehydrogenation occurring during polymerization. The polymerization temperature is typically dominated by the temperature where the halogen cleaves off from the monomer, so to increase the separation of polymerization and cyclodehydrogenation, the dehalogenation temperature should be minimized. Iodine has been shown to cleave from the monomer more readily on Au, thereby reducing the dehalogenation temperature and improving GNR length, as shown in Figure 2.8. Further separation of these temperatures could potentially be realized by using a different metal surface that catalyzes dehalogenation more readily than cyclodehydrogenation. Nevertheless, monomers are only able to move in two dimensions during on-surface polymerization and may be trapped by adjacent, passivated molecules which makes significant improvements in length distribution challenging. Moving the GNR growth to a solution lifts the restrictive diffusion of the surface polymerization and removes the need to account for steric hindrance during monomer design.

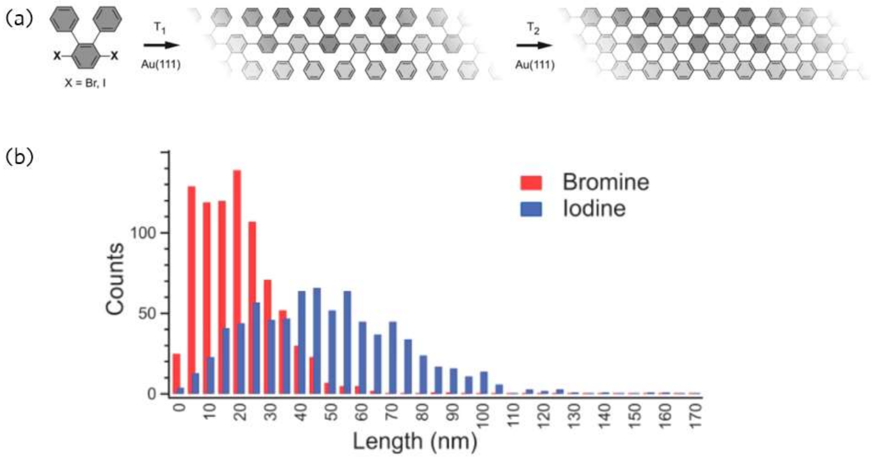

Figure 2.8 | Improving GNR length by replacing the halogen in the precursor molecule. (a) 9AGNR growth used to optimize length by changing the halogen in the X position of the precursor. (b) GNR length distribution shows an improvement in average length with iodine as in the monomer due to its lowered dehalogenation temperature[8].

2.4 Solution synthesis

Solution synthesis of atomically precise GNRs followed the first on-surface growth of 7AGNRs[12]. Some of the first GNRs demonstrated with surface synthesis are shown on Figure 2.9. The solution growth follows the same steps except for sublimation as its on-surface counterpart: precursor design and synthesis, dehalogenation, polymerization, and cyclodehydrogenation. Instead of a surface to template and catalyze the growth, GNRs that may not grow on a surface, due to steric hindrance of the monomers, will readily grow in solution, with the assistance of catalysts. This expands the GNR library by introducing new types of GNRs unattainable from surface reactions. Furthermore, growth kinetics in three dimensions are more favorable for realizing long polymers. Indeed, long GNRs (50-100 nm) have been demonstrated by solution synthesis[12,13].

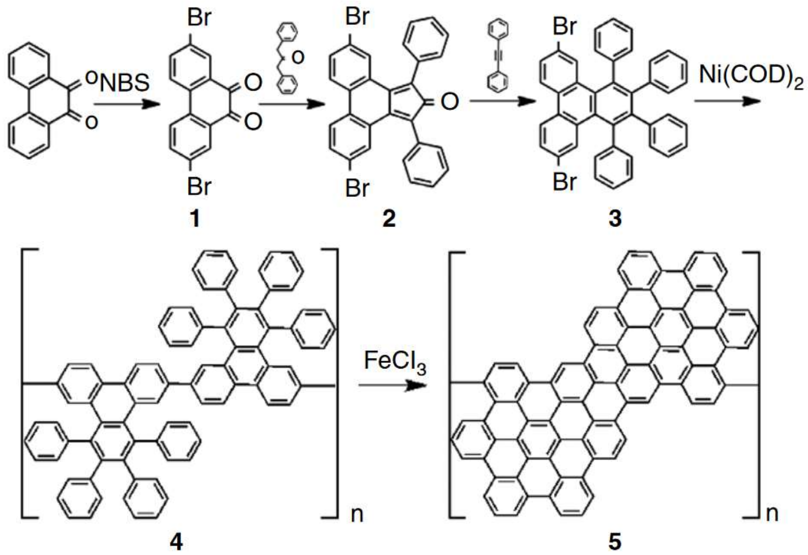

Figure 2.9 | Solution synthesis of chevron type GNR. Similar to on-surface growth, GNRs can be polymerized and cyclized in solution by employing the use of catalysts in solution[12].

While running the reaction in a solution prevents atomic resolution imaging via in-situ STM, other avenues of manipulation characterization are opened. For instance, long polymers can be sorted and purified by using common polymer chemistry techniques such as column chromatography[13], and the optical properties of suspended GNRs in solution can be characterized with optical absorption and photoluminescence-emission measurements. However, on-surface characterization of solution synthesized GNRs is elusive mainly due to the challenges in suspending the GNR in solution and the deposition of isolated GNR or well dispersed GNR networks on a surface.

Solution GNRs are attractive for device applications for the reasons described above and for their scalability. Scaling the growth to produce milligrams or grams of GNRs is much simpler done in solution than on a surface in UHV conditions. However, GNRs interact strongly with each other in solution (even more than CNTs due to GNR-GNR pi-pi stacking and the mechanical flexibility of GNRs), and weakly with surfaces. The most common GNRs grown in solution also suffer from a wide band gap[14]. As will be described in the next chapters, the development of high-performance devices is impeded by the wide band gap of bottom-up GNRs. While there has been moderate progress in the manipulation and deposition of solution based GNRs, the device behavior is poor and the on-surface characterizations, such as STM, are inconclusive[15,16]. The development of solution GNR devices and studies of the GNR electronic properties will require new approaches for the manipulation and deposition of solution GNRs.

2.5 Growth of GNR heterostructures

If different types of GNR precursors are introduced in the growth, the monomers sometimes copolymerize, resulting in GNRs made up of the covalently bonded GNR sections corresponding to each type of monomer used. On a surface, this means evaporating two different kind of monomers before polymerization[17,18]. For example, 7AGNR and 13AGNR monomers can be co-deposited on Au(111) and annealed to yield 7-13 heterostructures[17] such as the one shown in Figure 2.10. Key factors for a successful heterojunction growth are the dehalogenation and cyclization temperatures of the individual GNR components as well as the position of the halogens. If one section cyclizes before the other section has the opportunity to copolymerize, the GNRs will grow independently without interacting. Similarly, if the radical locations do not align on the surface due to steric hindrance, the GNRs will also grow without forming heterojunctions. Finally, this co-deposition technique leads to random co-polymer section lengths which may not be ideal for device design and fabrication. Progress has been made to control the length of the subunits[19], but the GNRs remain too short for device integration.

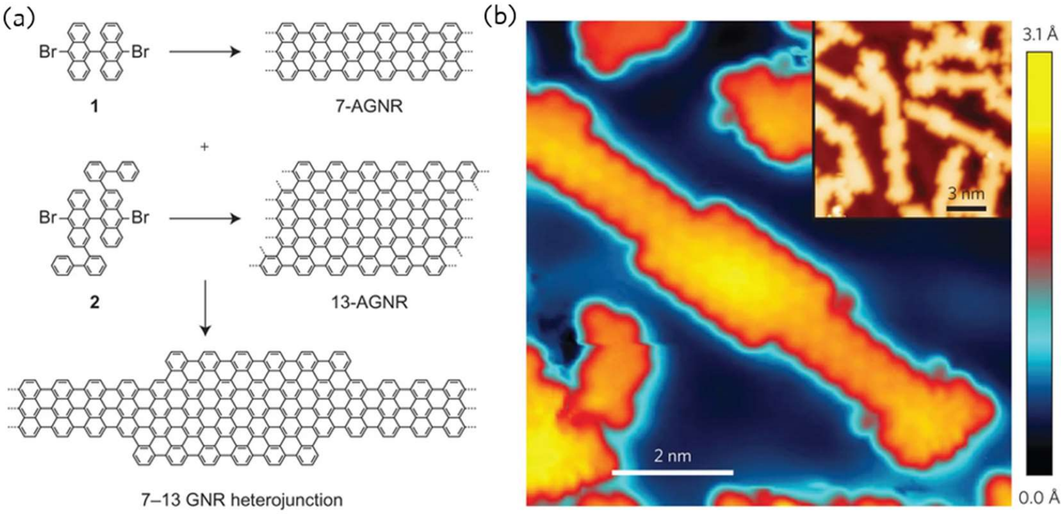

Figure 2.10 | STM of 7-13 AGNR heterostructures. (a) Synthesis of 7-13 AGNR heterojunction involves co-deposition of the 7AGNR and the 13AGNR monomer. (b) STM image of a 7-13-7 quantum dot created by co-deposition and growth[17].

2.6 Conclusions

Bottom-up chemical synthesis can be used to produce GNRs with precision at the molecular level. The GNR structure is determined by the monomer synthesized and purified. Various types of GNR structures have been realized using bottom-up synthesis. GNRs can be grown either in solution, with soluble catalysts introduced, or a surface, with the surface catalysing the growth. On a surface, the metal surface can template the growth and determine the structure of the GNR. Finally, if monomers of different types are introduced, the GNR heterostructures can form, which are promising for novel (opto)electronic device applications. For the study and development of GNR devices, GNRs must be transferred to an insulator and contacted with metal electrodes, as presented in the next chapter.

2.7 References

1. Talirz, L., Söde, H., Kawai, S., Ruffieux, P., Meyer, E., Feng, X., Müllen, K., Fasel, R., Pignedoli, C. A. & Passerone, D. Band Gap of Atomically Precise Graphene Nanoribbons as a Function of Ribbon Length and Termination. *ChemPhysChem* **20,** 2348–2353 (2019). https://doi.org/10.1002/cphc.201900313

2. Lawrence, J., Brandimarte, P., Berdonces-Layunta, A., Mohammed, M. S. G., Grewal, A., Leon, C. C., Sánchez-Portal, D. & de Oteyza, D. G. Probing the Magnetism of Topological End States in 5-Armchair Graphene Nanoribbons. *ACS Nano* **14,** 4499–4508 (2020). https://doi.org/10.1021/acsnano.9b10191

3. Segawa, Y., Ito, H. & Itami, K. Structurally uniform and atomically precise carbon nanostructures. *Nature Reviews Materials* **1,** 15002 (2016). https://doi.org/10.1038/natrevmats.2015.2

4. Zhang, X., Yazyev, O. V., Feng, J., Xie, L., Tao, C., Chen, Y.-C., Jiao, L., Pedramrazi, Z., Zettl, A., Louie, S. G., Dai, H. & Crommie, M. F. Experimentally Engineering the Edge Termination of Graphene Nanoribbons. *ACS Nano* **7,** 198–202 (2013). https://doi.org/10.1021/nn303730v

5. Cai, J., Ruffieux, P., Jaafar, R., Bieri, M., Braun, T., Blankenburg, S., Muoth, M., Seitsonen, A. P., Saleh, M., Feng, X., Müllen, K. & Fasel, R. Atomically precise bottom-up fabrication of graphene nanoribbons. *Nature* **466,** 470–473 (2010). https://doi.org/10.1038/nature09211

6. Talirz, L., Söde, H., Dumslaff, T., Wang, S., Sanchez-Valencia, J. R., Liu, J., Shinde, P., Pignedoli, C. A., Liang, L., Meunier, V., Plumb, N. C., Shi, M., Feng, X., Narita, A., Müllen, K., Fasel, R. & Ruffieux, P. On-Surface Synthesis and Characterization of 9-Atom Wide Armchair Graphene Nanoribbons. *ACS Nano* **11,** 1380–1388 (2017). https://doi.org/10.1021/acsnano.6b06405

7. Talirz, L., Ruffieux, P. & Fasel, R. On-Surface Synthesis of Atomically Precise Graphene Nanoribbons. *Adv. Mater.* 6222–6231 (2016). https://doi.org/10.1002/adma.201505738

8. Di Giovannantonio, M., Deniz, O., Urgel, J. I., Widmer, R., Dienel, T., Stolz, S., Sánchez-Sánchez, C., Muntwiler, M., Dumslaff, T., Berger, R., Narita, A., Feng, X., Müllen, K., Ruffieux, P. & Fasel, R. On-Surface Growth Dynamics of Graphene Nanoribbons: The Role of Halogen Functionalization. *ACS Nano* **12,** 74–81 (2018). https://doi.org/10.1021/acsnano.7b07077

9. Linden, S., Zhong, D., Timmer, A., Aghdassi, N., Franke, J. H., Zhang, H., Feng, X., Müllen, K., Fuchs, H., Chi, L. & Zacharias, H. Electronic Structure of Spatially Aligned Graphene Nanoribbons on Au(788). *Phys. Rev. Lett.* **108,** 216801 (2012). https://doi.org/10.1038/ncomms10177

10. de Oteyza, D. G., García-Lekue, A., Vilas-Varela, M., Merino-Díez, N., Carbonell-Sanromà, E., Corso, M., Vasseur, G., Rogero, C., Guitián, E., Pascual, J. I., Ortega, J. E., Wakayama, Y. & Peña, D. Substrate-Independent Growth of Atomically Precise Chiral Graphene Nanoribbons. *ACS Nano* **10,** 9000–9008 (2016). https://doi.org/10.1021/acsnano.6b05269

11. Fairbrother, A., Sanchez-Valencia, J.-R., Lauber, B., Shorubalko, I., Ruffieux, P., Hintermann, T. & Fasel, R. High vacuum synthesis and ambient stability of bottom-up graphene nanoribbons. *Nanoscale* **9,** 2785–2792 (2017). https://doi.org/10.1039/C6NR08975E

12. Vo, T. H., Shekhirev, M., Kunkel, D. A., Morton, M. D., Berglund, E., Kong, L., Wilson, P. M., Dowben, P. A., Enders, A. & Sinitskii, A. Large-scale solution synthesis of narrow graphene nanoribbons. *Nat Commun* **5,** (2014). https://doi.org/10.1038/ncomms4189

13. von Kugelgen, S., Piskun, I., Griffin, J. H., Eckdahl, C. T., Jarenwattananon, N. N. & Fischer, F. R. Templated Synthesis of End-Functionalized Graphene Nanoribbons through Living Ring-Opening Alkyne Metathesis Polymerization. *J. Am. Chem. Soc.* **141,** 11050–11058 (2019). https://doi.org/10.1021/jacs.9b01805

14. Radocea, A., Sun, T., Vo, T. H., Sinitskii, A., Aluru, N. R. & Lyding, J. W. Solution-Synthesized Chevron Graphene Nanoribbons Exfoliated onto H:Si(100). *Nano Lett.* (2016). https://doi.org/10.1021/acs.nanolett.6b03709

15. Abbas, A. N., Liu, G., Narita, A., Orosco, M., Feng, X., Müllen, K. & Zhou, C. Deposition, Characterization, and Thin-Film-Based Chemical Sensing of Ultra-long Chemically Synthesized Graphene Nanoribbons. *J. Am. Chem. Soc.* **136,** 7555–7558 (2014). https://doi.org/10.1021/ja502764d

16. Abbas, A. N., Liu, B., Narita, A., Dössel, L. F., Yang, B., Zhang, W., Tang, J., Wang, K. L., Räder, H. J., Feng, X., Müllen, K. & Zhou, C. Vapor-Phase Transport Deposition, Characterization, and Applications of Large Nanographenes. *J. Am. Chem. Soc.* **137,** 4453–4459 (2015). https://doi.org/10.1021/ja513207e

17. Chen, Y.-C., Cao, T., Chen, C., Pedramrazi, Z., Haberer, D., Oteyza, D. G. de, Fischer, F. R., Louie, S. G. & Crommie, M. F. Molecular bandgap engineering of bottom-up synthesized graphene nanoribbon heterojunctions. *Nat Nano* **10,** 156–160 (2015). https://doi.org/10.1038/nnano.2014.307

18. Cai, J., Pignedoli, C. A., Talirz, L., Ruffieux, P., Söde, H., Liang, L., Meunier, V., Berger, R., Li, R., Feng, X., Müllen, K. & Fasel, R. Graphene nanoribbon heterojunctions. *Nat Nano* **9,** 896–900 (2014). https://doi.org/10.1038/nnano.2014.184

19. Bronner, C., Durr, R. A., Rizzo, D. J., Lee, Y.-L., Marangoni, T., Kalayjian, A. M., Rodriguez, H., Zhao, W., Louie, S. G., Fischer, F. R. & Crommie, M. F. Hierarchical On-Surface Synthesis of Graphene Nanoribbon Heterojunctions. *ACS Nano* **12,** 2193–2200 (2018). https://doi.org/10.1021/acsnano.7b08658

3 GNR transfer and device fabrication

The GNR growth method, quality, and desired device configuration determine the best strategy for the device fabrication process. GNR placement onto an insulating surface (transfer) and contact with patterning techniques are the two critical steps in the device fabrication process. A layer transfer technique can be employed for placing GNRs on an insulating surface after growth on a metal surface[1–3]. Solution deposition techniques can be employed to place GNRs on any surface, albeit with limited success so far due to GNR aggregation. After placement, a GNR is contacted at each end for individual-GNR devices or bulk GNR films are contacted for thin film devices. The required feature size is usually dependent on the GNR length for single GNR devices. For example, the fabrication of a single-GNR devices using the surface growth process will require a layer transfer process to an insulator as well as patterning of contacts with ~20 nm gaps, due to the short length (10s of nanometers) of these GNRs. In contrast, feature size constraints are relaxed for the fabrication of devices with large scale GNR or CNT films that cover large areas (100s of micrometers) allowing for contact gaps that can be as large as 10s of micrometers. While the fabrication of thin film devices is significantly simpler, characterization of single-GNR nanoscale devices are critical in the understanding the intrinsic electron transport of GNRs and developing high-performance FETs.

In this chapter, the device fabrication of individual-GNR devices is described. As illustrated in Chapter 2, GNRs can be grown on Au(111) and imaged in-situ with high resolution STM. Unfortunately, resolving single-GNR has not been achieved once the sample is removed from the UHV chamber and transferred to an insulating surface. The short GNR length, GNR transfer, and inability to image individual GNRs are the main challenges in the device fabrication process. To overcome these challenges, GNRs are grown on a thin Au(111) film that can be used as a sacrificial and mechanical support layer during transfer to the device substrate. Then 100s of electrode pairs with ~20 nm spacing are patterned on the transferred region and probed in the search for a GNR in the electrode gap. This type of shotgun approach is commonly used in molecular electronics where individual molecules are also difficult to locate[4].

First, large patterns, such as the pads used for electrical probing, are patterned using optical lithography. Then, GNRs are transferred from their growth substrate and, finally, nanoscale contacts are patterned via electron beam lithography.

3.1 Optical lithography of the device substrate

The semiconductor industry has used optical lithography for the patterning and fabrication of integrated circuits for decades. In an academic lab, deep UV lithography steppers provide patterning with a resolution of ~200 nm. Our finest feature size is the source-drain gap that must be smaller than the GNR length, which is on the order of ~20 nm and must be patterned with electron beam lithography as a result. The larger patterns (probing pads, alignment markers) needed are on the order of 10s of μm and can be readily patterned with optical lithography.

The major advantage of optical lithography is the speed, reliability, and availability of standardized processes. The UC Berkeley Nanolab optical lithography baseline liftoff process for the patterning of large probing pads as well as alignment markers for subsequent patterning steps was employed to pattern the device substrates before GNR transfer. Two different types of device substrates are used in this work. Substrates with 50 nm SiO_2 global back gates were used for initial device studies, where the simplicity in the fabrication and robustness of the gate improved the yield. To improve the performance of devices, local back gate structures with 6.5 nm HfO_2 gate dielectrics with metal gate electrodes were patterned.

Preparation of device substrate with 50 nm SiO_2 back gates: Using dry oxidation, 50 nm SiO_2 was grown on heavily doped 150 mm silicon wafers. Alignment markers and large pads for electrical probing were patterned using standard photolithography and lift-off patterning of 3 nm Cr and 25 nm Pt. The wafer was then diced and individual chips were used for GNR transfer and further device processing.

Preparation of device substrate 6.5 nm HfO_2 local back gates. Using dry oxidation, 100 nm SiO_2 was grown on 150 mm silicon wafers. The local back gates were lithographically patterned and dry etched into the SiO_2 followed by lift-off of 3 nm Ti and 17 nm Pt to obtain a planar backgate. 6.5 nm HfO_2 was grown in an atomic layer deposition system at 135 °C. Alignment markers and large pads for electrical probing were patterned using standard photolithography and lift-off of 3 nm Cr and 25 nm Pt. The wafer was then diced and individual chips were used for GNR transfer and further device processing. The process is summarized in Figure 3.1.

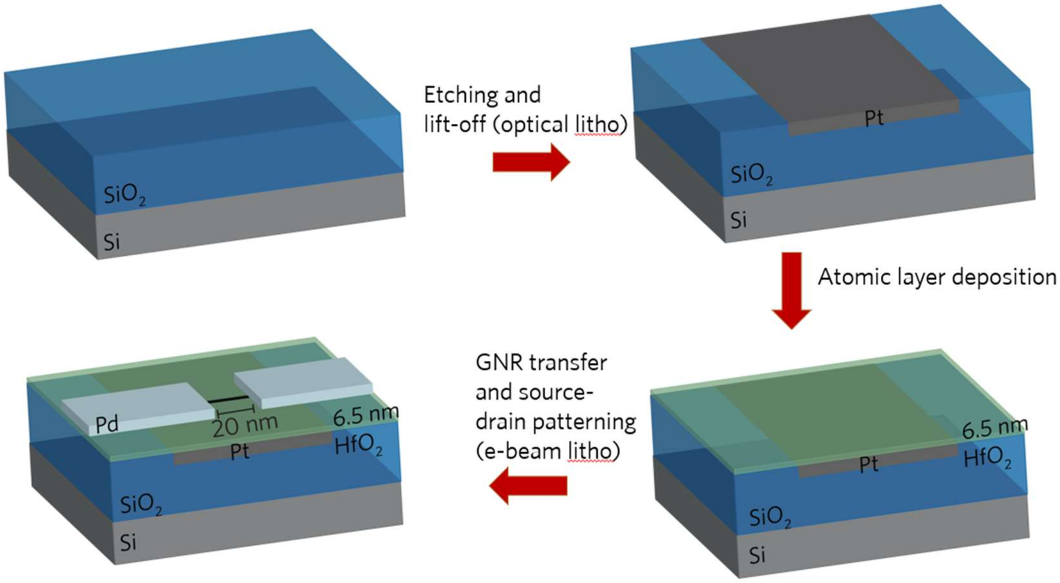

Figure 3.1 | Fabrication of local back gate GNR FET. A trench in a bare, oxidized wafer is first etched then filled with Pt that serves as the local back gate. The thin HfO_2 gate dielectric was grown

via atomic layer deposition. Then, GNRs were transferred and source drain electrodes patterned with electron beam lithography.

3.2 GNR transfer

The transfer of GNRs from Au(111) to the device substrate can be performed by a layer transfer of the Au film from the mica onto the device substrate and a Au etch. As shown in Figure 3.2, the GNR/Au/mica was floated in 38% HCl in water, which caused the mica to delaminate with the Au film remaining floating on the surface of the acid[1]. The floating gold film was picked up with the target substrate, with the GNRs facing the dielectric surface. Subsequent gold etching in KI/I_2 yielded isolated, randomly distributed GNRs with sub-monolayer coverage on the target substrate.

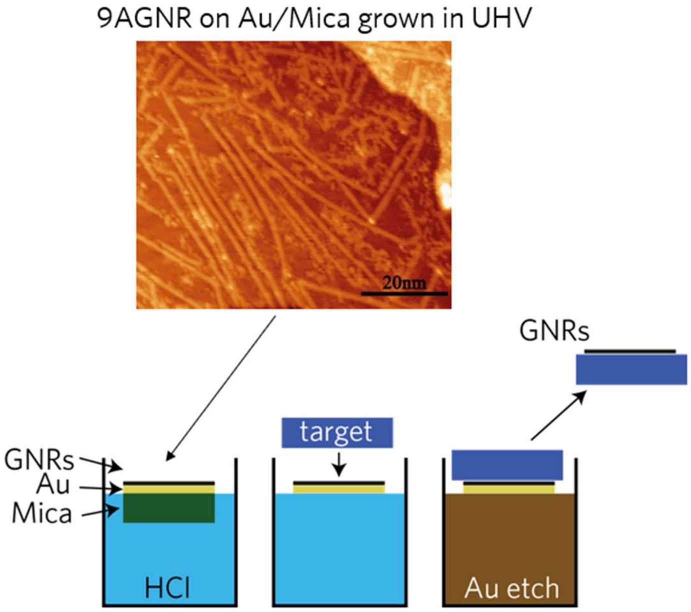

Figure 3.2 | GNR transfer from Au/mica onto an arbitrary substrate. GNRs are grown on Au/mica films, then floated on HCl which cleaves off the mica. The target substrate is used to pick up the Au film. The film is etched and GNRs are left on the substrate.

To track the efficiency and whether the transfer damages the GNRs, the Raman spectrum of the GNRs was taken before and after transfer and confirmed to show little change, as shown in Figure 3.3. Raman measurements were made with a Horiba Jobin Yvon LabRAM ARAMIS Raman microscope using 532 nm and 785 nm diode lasers with 10 mW power each and a 50x objective lens, resulting in a 1-2 micrometer spot size. No thermal effects were observed under these measurement conditions and an average of 5 spectra from different points was made for each sample. More detailed discussion of Raman spectroscopy of GNRs is discussed in Chapter 4.

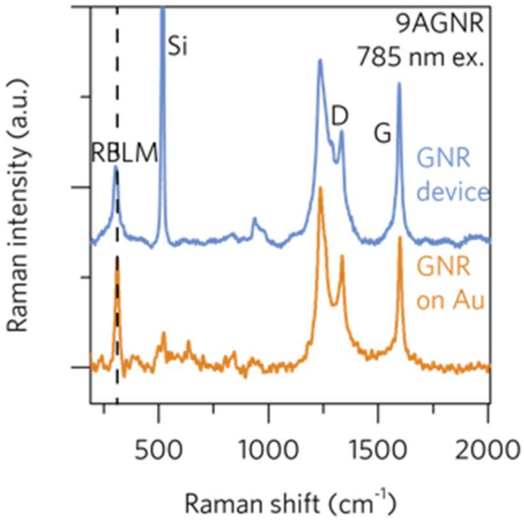

Figure 3.3 | Raman spectrum of 9AGNRs before and after transfer. Raman spectra of 9AGNRs on the Au(111) growth substrate and after device fabrication shows that the GNRs remain intact.

3.3 Electron beam lithography

The critical patterning step in the device fabrication process is the electron beam lithography since it will determine the device yield and the resulting performance. The requirements for this process are quite strict, (1) the resolution of this process needs to be in the order of 20 nm due to the short GNR length, which isn't trivial for the average electron beam lithography setup ,(2) there needs to be little variability from pattern to pattern on each individual chip, and (3) the writing speed of the patterns needs to be fast so that a whole chip can be patterned in a reasonable amount of time. There are trade-offs between speed, variability and resolution, so a few tricks can be employed to be able to meet all these requirements in the patterning. First, a thin electron beam resist layer minimizes the amount of scattering as the electron beam exposes the PMMA, reducing proximity effects as well as broadening of the beam as it travels through the film. Second, a high electron beam energy ensures a more uniform beam at higher currents which allows for faster patterning of fine features with lower variability. Finally, resist development at low temperatures improves contrast and lowers variability of the pattern[5].

After the GNR transfer, poly-methyl methacrylate (PMMA, molecular weight 950K) was spun on the chips at 4 Krpm and followed by a 10 min bake at 180 °C. ~300 source drain electrodes (100 nm wide, 20 nm gaps) were patterned using a JEOL 6300-FS 100 kV e-beam lithography system and subsequently developed in 3:1 IPA:MIBK at 5 °C. 10 nm Pd was deposited using e-beam evaporation and lift-off was completed in Remover PG at 80 °C. A typical source-drain electrode pair is shown in Figure 3.4.

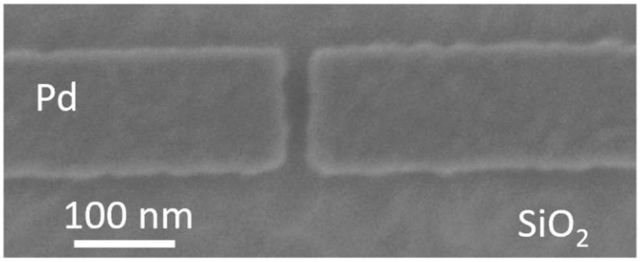

Figure 3.4 | Micrograph of electrode pair patterned with electron beam lithography. The high-resolution electron beam lithography patterning yields gaps that are ~20 nm long which is sufficient for contacting some GNRs.

3.4 Conclusion

In this chapter, the strategy for successfully yielding GNR FETs was presented. The process consists of mixed lithography patterning in which large features are patterned via standard optical lithography and the critical small features are patterned with electron beam lithography. Most importantly, the electron beam lithography process is the critical step in yielding high performance devices. A high speed, high resolution, and low variability electron beam process is ideal for GNR device patterning. In between the lithography steps, GNRs are transferred from their growth substrate to the patterned chips via a layer transfer process. After fabrication, devices are inspected and electrically characterized, as discussed in the next chapters.

3.5 References

1. Cai, J., Pignedoli, C. A., Talirz, L., Ruffieux, P., Söde, H., Liang, L., Meunier, V., Berger, R., Li, R., Feng, X., Müllen, K. & Fasel, R. Graphene nanoribbon heterojunctions. *Nat Nano* **9,** 896–900 (2014). https://doi.org/10.1038/nnano.2014.184

2. Llinas, J. P., Fairbrother, A., Barin, G. B., Shi, W., Lee, K., Wu, S., Choi, B. Y., Braganza, R., Lear, J., Kau, N., Choi, W., Chen, C., Pedramrazi, Z., Dumslaff, T., Narita, A., Feng, X., Müllen, K., Fischer, F., Zettl, A., Ruffieux, P., Yablonovitch, E., Crommie, M., Fasel, R. & Bokor, J. Short-channel field-effect transistors with 9-atom and 13-atom wide graphene nanoribbons. *Nature Communications* **8,** 633 (2017). https://doi.org/10.1038/s41467-017-00734-x

3. Bennett, P. B., Pedramrazi, Z., Madani, A., Chen, Y.-C., Oteyza, D. G. de, Chen, C., Fischer, F. R., Crommie, M. F. & Bokor, J. Bottom-up graphene nanoribbon field-effect transistors. *Applied Physics Letters* **103,** 253114 (2013). https://doi.org/10.1063/1.4855116

4. Jia, C., Migliore, A., Xin, N., Huang, S., Wang, J., Yang, Q., Wang, S., Chen, H., Wang, D., Feng, B., Liu, Z., Zhang, G., Qu, D.-H., Tian, H., Ratner, M. A., Xu, H. Q., Nitzan, A. & Guo, X. Covalently bonded single-molecule junctions with stable and reversible photoswitched conductivity. *Science* **352,** 1443–1445 (2016). https://doi.org/10.1126/science.aaf6298

5. Hu, W. (Walter), Sarveswaran, K., Lieberman, M. & Bernstein, G. H. Sub-10 nm electron beam lithography using cold development of poly(methylmethacrylate). *Journal of Vacuum Science & Technology B: Microelectronics and Nanometer Structures Processing, Measurement, and Phenomena* **22,** 1711–1716 (2004). https://doi.org/10.1116/1.1763897

4 Band gap of graphene nanoribbons

Introductory texts in semiconductor materials and devices discuss the band gap of a material as an intrinsic parameter that does not depend on the material's dielectric environment. A piece of silicon has the same band gap in vacuum as it does when it is placed on a conductive surface. Furthermore, the optical band gap of bulk materials like silicon tends to be very close to the transport band gap, making optical measurements quick and efficient methods for characterizing the band gap of bulk semiconductors. The band gap is such a critical parameter for semiconductor device design which makes optical measurement techniques a key part of material characterization. Furthermore, modern first principles calculations also give accurate values for the band gaps of bulk semiconductors[1].

For ultra-narrow GNRs, the optical, transport, and theoretical band gaps often do not match. The transport gap tends to depend strongly on the dielectric environment of the GNR (i.e. is the GNR on Au or on an insulator?), making the band gap analysis for GNRs more complex. Understanding the band gap of graphene nanoribbons is critical for design and development of devices but the reported band gap of the first bottom-up synthesized GNRs varied greatly: the band gap was measured to be ~2.4 eV on Au via scanning tunneling spectroscopy[2,3]. Meanwhile, the theorical band gap of the GNR in vacuum was closer to 3.8 eV[4] and the optical absorption on Au was measured to be 2.1 eV[5].

In this chapter, the different characterization techniques and sources of discrepancies in the reported bang gaps of GNRs are discussed, as well as the reasons why the theorical band gap is the best value to use for GNR device development in lieu of transport measurements on an insulating substrate.

4.1 Scanning Tunneling Spectroscopy

One of the biggest advantages of GNRs grown on atomically flat surfaces in UHV is that scanning tunneling spectroscopy (STS) can be used in-situ to measure the local density of states (LDOS) of the material, allowing for the characterization of the electronic structure of the pristine, as-grown GNRs. In STS, a metal tip is brought into close proximity to the sample so that a tunneling current can be measured from the tip to the substrate. The tunneling probability is proportional to the number of empty states available at an energy less than or equal to the chemical potential at the tip. Thus, the change in tunneling current versus the change in voltage (dI/dV) of the tip corresponds to the number of states at the chemical potential and location of the tip. The band gap can be read directly from the on-set of the conduction band and the valence band in the dI/dV spectrum.

After new GNRs are grown in STM UHV chambers and imaged, STS is used to characterize the LDOS of the GNR and STS maps can image energy eigenstates of the electronic wavefunctions and compared to theory (DFT). The STS and DFT band gaps of various GNRs is summarized in Table 1. The measured band gap on Au and DFT value agree but the STS band gap of 7AGNR depends on whether it is on Au or on NaCl (an insulator). For the theory to include the effect of the dielectric environment on the band structure, the multibody interactions must be considered. Au screens the electron-electron interactions in the GNR, causing the band gap to renormalize to a lower value than if the GNR were on vacuum. Therefore, the details of the GNR environment will affect the experimentally measured values and those values may not be applicable for device development, where the GNR is in a very different dielectric environment. Until experiments of GNR band gap can be performed on devices, theory can bridge this gap between experimental band gap values and optimizing GNR band gap for device development. In the next section, different levels of theoretical calculations will be discussed to understand the various parameters that affect the band gap in ultra-narrow GNRs.

Table 1 | Band gaps of armchair GNRs from experiment and theory.

	STS on Au	STS on NaCl	Absorption	DFT+LDA[4]	DFT+GW[4]
5AGNR	0.8 eV[6]	1.3 eV[6]	N/A	0.4 eV	1.7 eV
7AGNR	2.4 eV[3]	3.2 eV[7]	2.3 eV[8]	1.6 eV	3.8 eV
9AGNR	1.4 eV[9]	N/A	1.3eV[8]	0.7 eV	2.1 eV
13AGNR	1.4 eV[2]	N/A	N/A	1.5 eV	2.3 eV

4.2 First principles calculations

Confinement of electrons in graphene into a one-dimensional structure intuitively opens up a band gap. As follows from Dirac equation in a quantum well, the GNR or CNT band gap follows w^{-1} or d^{-1} relations[10], where w is the GNR width and d is the CNT diameter. Various models can be used to calculate the band gap in ultra-narrow GNRs but, as described earlier, multibody physics must be considered to fully capture the GNR bandgap in various dielectric environments. Nevertheless, it is useful to look at simpler band structure models, like tight binding (TB), and work towards more complete models, such as density functional theory with local density approximation (DFT-LDA) and DFT with multibody corrections (DFT-GW).

The TB model calculates the band structure by using the superposition of the single-atom electronic wavefunctions. These calculations predict the band gap for GNRs wider than a few nanometers and fit the w^{-1} relation. As shown in Figure 4.1, the band gap trend splits into three families, $N = 3p, 3p + 1, 3p + 2$, where N is the width of the GNR in number of atoms and p is a non-negative integer, 0, 1, 2, ...[4] Due to the quantization of the electronic wavevector across the GNR width, the $3p + 2$ family has zero band gap (e.g. 5AGNR), and the other two families have non-zero band gaps that vary with w^{-1} (e.g. 7AGNR or 13AGNR). This effect is analogous to the wavevector quantization leading to a third of CNTs being metallic, as described in Section 1.1. The

TB model illustrates how the band gap varies in GNRs and how it depends on the number of carbon atoms across the width. However, it does not capture all the physics required to accurately predict the absolute value of the band gap. The TB model assumes that the hopping parameters (i.e. bond lengths) are all equal in the GNR even though the carbon atoms at the edges are also bonded with hydrogen which will affect the carbon-carbon bond length. Also, electronic correlation is not considered in the model. Both bond length relaxation and electron correlation can be treated or at least approximated with DFT.

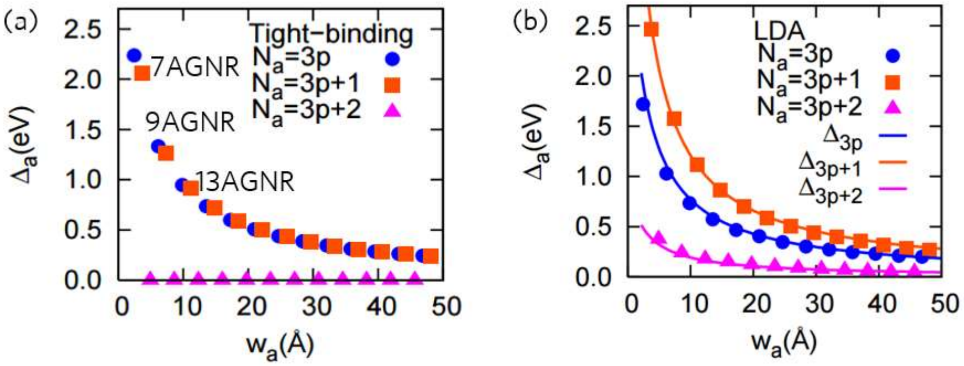

Figure 4.1 | Tight binding and DFT-LDA gaps. (a) Tight-binding model for the band gap of GNRs. (b) DFT+LDA calculation for the GNR band gap, where the relaxation of bond-lengths across the GNR corrects the TB calculation[11].

Bond length relaxation lifts the degeneracy of the two families of GNRs that follow the same trend (3*p* and 3*p*+1) and it opens the band gap in the 3p+2 family[11]. As shown in Figure 4.1, the calculated band gap now follows three different trends as a result of the bond length varying across the GNR. The bond length is shorter at the edges of the GNR, changing the boundary conditions and the effective confinement width. In these calculations, the local density approximation (LDA) is used to estimate the exchange-correlation term. LDA is a mean field approach to estimate the effect of the electron bath on an electron's energy. With the bond length relaxation and LDA, DFT more accurately predicts the band gap of the GNR on a conductor like Au.

In a system that has very low screening such as high localized 1D chain such as GNRs, individual electrons interact strongly with each other thereby making the mean field approximation invalid and the band structure will depend very strongly not only on the structure and doping of the material but also on the dielectric environment. As the GNR is lifted from the Au and placed on an insulator, an individual electron's effect on the electronic bath is no longer screened out and the band gap becomes renormalized to a higher energy[7]. The GW approximation (GWA) is used to treat this effect and calculate the band gap of the GNR in vacuum[4], where the self-energy effect will be the strongest, as shown in Figure 4.2.

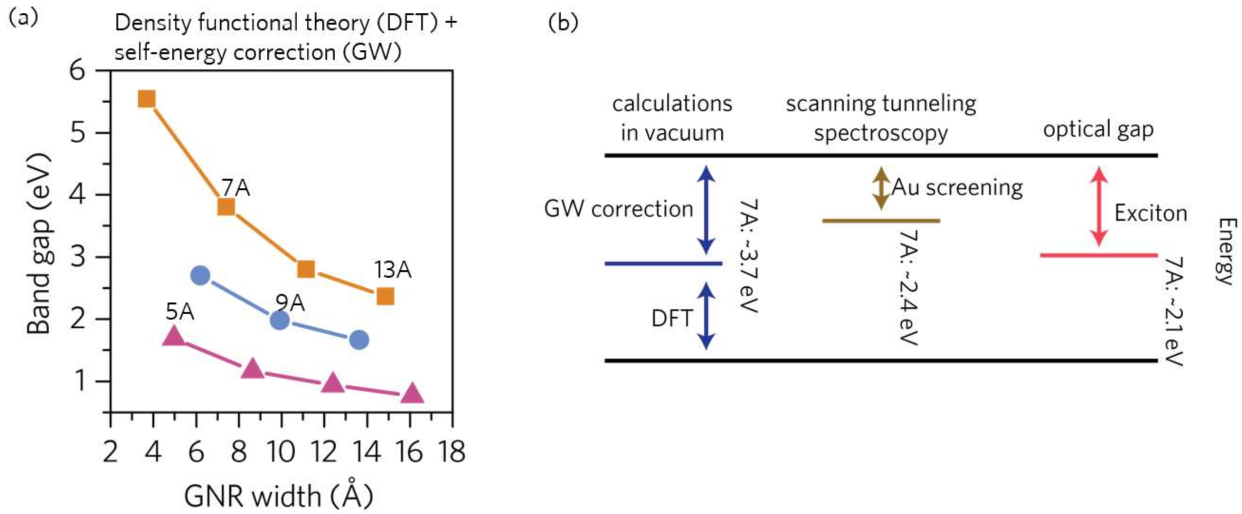

Figure 4.2 | DFT-GW calculation of GNRs in vacuum. (a) DFT with GWA of the band gap of GNRs shows a large self-energy correction from DFT+LDA[4]. (b) DFT-GW is accurate estimating the band gap of GNRs on an insulator, while the optical or STS on Au techniques give the GNR band gap on conductive surfaces.

DFT with GWA calculations performed by Yang et. al. [4] show that GNRs with widths less than 2 nm in the $3p + 2$ family tend to have the smallest band gaps (e.g. the 11-atom wide GNR has a band gap of 0.90 eV). On the other hand, GNRs in the $3p + 1$ family tend to have the largest band gaps: 2.35 eV for the 13-atom wide GNR or 3.80 eV for the 7-atom wide GNR. The trend in the band gap of GNRs in the $3p$ family tends to fall in between the $3p$ + 1 and $3p$ + 2 families. It is likely that band gap values calculated from DFT with GWA give the closest value of the actual GNR band gap on an insulator. Until there are reliable experimental methods to measure the transport gap of GNRs on an insulator, GNR device design should be guided by the DFT with GWA band gaps.

Understanding of the optical band gap of the GNR is of importance for optoelectronic device development and it is an important value to compare to the theoretical gap as well as the experimental gaps. As will be discussed in the next two sections, GNR optical transitions are excitonic in nature (i.e. atom-like). Photoluminescence-emission spectroscopy and resonant Raman spectroscopy were used to probe these optical transitions.

4.3 Photoluminescence-emission spectroscopy of solution GNRs

Solution synthesized GNRs are difficult to manipulate and place on surfaces. However, they provide a large quantity of GNRs that if suspended in solution, can be characterized with a variety of optical techniques. One of such techniques is photoluminescence-emission (PLE) spectroscopy, where the spectrum of light emission from a sample is measured at varying excitation energies. Figure 4.3 shows the technique in a CNT, which is dominated by excitonic transitions. As long as the lowest lying excited level decays radiatively, the PLE emission vs excitation map shows a peak centered at the energy of the lowest lying excited level (first optical transition) in the emission axis and the energy of the second optically accessible transition in the excitation axis.

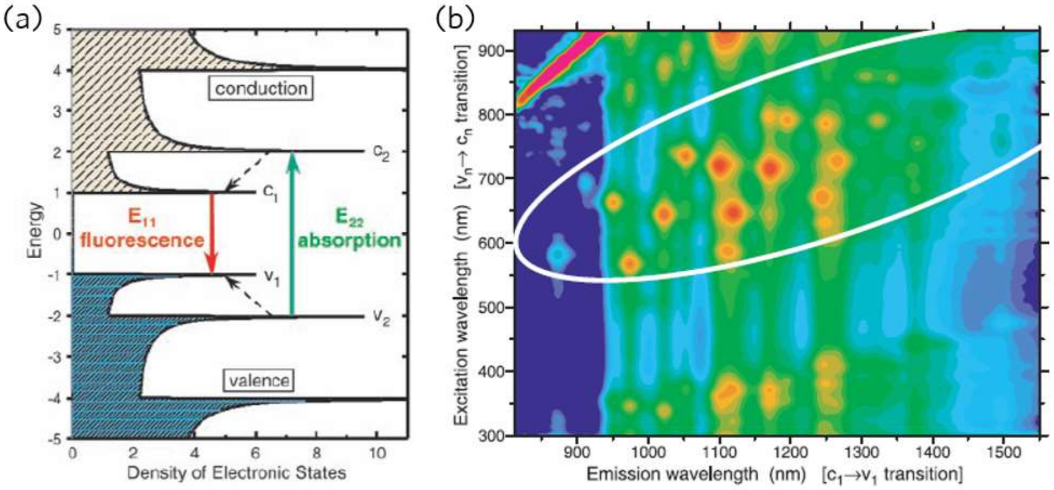

Figure 4.3 | Photoluminescence-emission spectroscopy of a CNT ensemble. (a) DOS of a CNT. CNT absorbs photons when the excitation energy hits the E_{22} absorption, then carriers recombine radiatively through the E_{11} fluorescence, resulting in the map in (b)[12]. Each peak in the map corresponds to a CNT of a different chirality.

Since a bulk semiconductor typically has a continuum of accessible optical states, the PLE map would show bright emission of the band gap energy for any excitation above the band gap (if the semiconductor has a direct band gap). While the GNR is a direct gap semiconductor, the electron-hole interactions are so strong that they form excitons as soon as an optical transition occurs. This lowers the energy of the optical transitions since the electrons are still spatially bound near the hole, and it causes the transitions to be discrete, corresponding the exciton binding energy[5], similar to CNTs shown in Figure 4.3.

The chevron GNR can be fabricated both on a surface and in solution[13,14]. When the GNRs are synthesized in solution, it forms a powder that can then be suspended in a solution. GNRs readily aggregate in solution and limit the concentration that can be successfully suspended. Concentrations of a few micrograms per mL will suspend in THF with the help of ultra-tip sonication. After suspension, the sample is placed in the PLE set-up and measured. The excitation-emission map shown in Figure 4.4 shows a single, broad peak. The peak may be broad due to fast carrier recombination at the ends of the GNRs or inhomogeneous broadening due to GNR aggregation. Despite these effects, the center of the peak corresponds well with the DFT-LDA values as shown in Figure 4.4. Since there is a discrete peak and not a continuum in the excitation-emission map, the GNR transitions are excitonic and dominated by electron-hole interactions. The first optical transition should be close to the DFT-LDA gap. The transport gap subtracted by the exciton binding energy (electron-hole interactions) corresponds to the first optical transition, E_{11}. The transport gap and the exciton binding energy both change by similar amounts (due to the equal effective mass of holes and electrons in GNRs) when the GNR is placed in different dielectric environments, thereby compensating and keeping the optical gap independent on the dielectric environment. Not surprisingly, the STS and DFT-LDA gap values agree for the chevron GNRs and the optical gap is only a few hundred meV smaller.

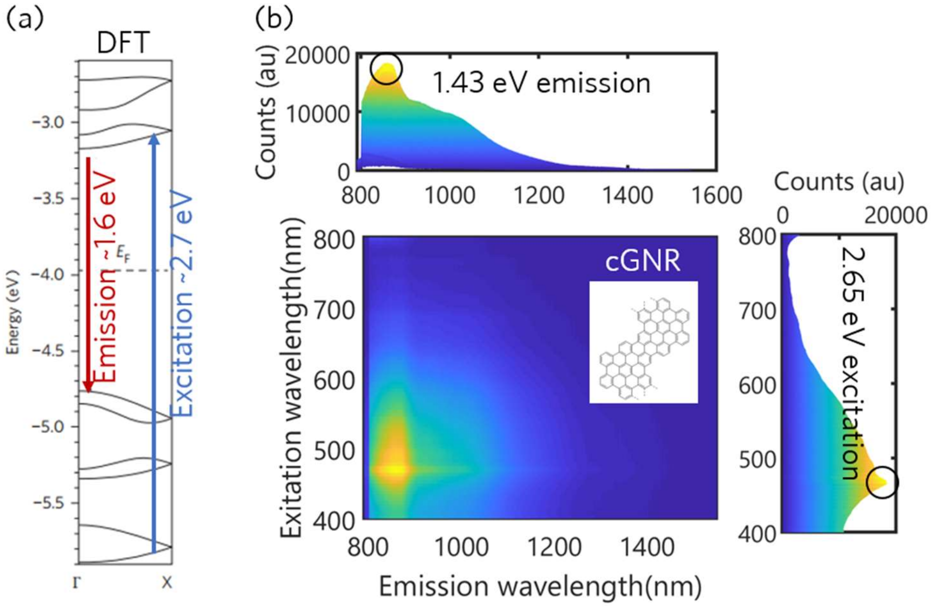

Figure 4.4 | Photoluminescence-emission spectroscopy of cGNRs. (a) DFT calculation of the band structure of cGNRs[13]. (b) PLE map of cGNRs suspended in THF. The peak is centered at 1.43 eV emission and 2.65 eV excitation. The emission is close to the DFT band gap with a small correction from excitonic effects. The excitation likely corresponds to the transition shown in (a) corresponding to E_{31} absorption. Note this transition is optically allowed if the light polarization is perpendicular to the cGNR axis. The light is unpolarized and the GNRs randomly oriented in this experiment.

The optical properties of GNRs on surfaces might differ from those in solution. Furthermore, the surface-grown GNRs may prove to be useful for a variety of applications and understanding their optical properties is critical for optoelectronic devices. PLE of GNRs on the surface has been challenging due to the shorter length of surface-grown GNRs and the presence of the substrate. Both the substrate and the short length of the GNRs cause non-radiative pathways that quench the emission in the GNRs and kill the emission signal. The signal in Raman spectroscopy is immune to non-radiative pathways due to the fast dynamics of Raman scattering.

4.4 Resonant Raman spectroscopy of 7AGNRs

Raman spectroscopy is a powerful tool that has been used in the study of graphene like materials for decades. Commercial systems are available that allow for fast and reliable Raman spectra to be obtained from samples on surfaces and in solution. The sensitivity of the Raman spectrum to the molecular structure of the material studied allows for studies such as single point defects in graphene or determining the exact chirality of CNTs[15]. In GNRs, Raman spectroscopy can track the quality of the GNRs during device processing[16] or determine the type of GNR grown by monitoring the radial-like breathing mode (RBLM)[17,18].

Raman spectroscopy probes the inelastic process called Raman scattering, where an electron is optical excited and scatters with a phonon then decays back to the ground state emitting a photon of energy equal to the incoming photon plus the change in energy in the phonon(s) scattered. strong dependence of the phonon band structure to the local molecular configuration gives Raman spectroscopy its sensitivity to defects. In graphene, this corresponds to a series of peaks including the G, D, 2D. For GNRs and CNTs, more peaks arise due to the lower symmetry in these systems. Most notably, the RBLM/RBM in GNRs/CNTs come from the phonon mode that arises from the breathing motion of the material along its width/diameter. As the width of the GNR is varied, the phonon energy and the RBLM shifts. The RBLM is so sensitive that a difference between 7AGNRs and 9AGNRs can be easily measured even though the 9AGNRs is only a couple of atoms wider[17].

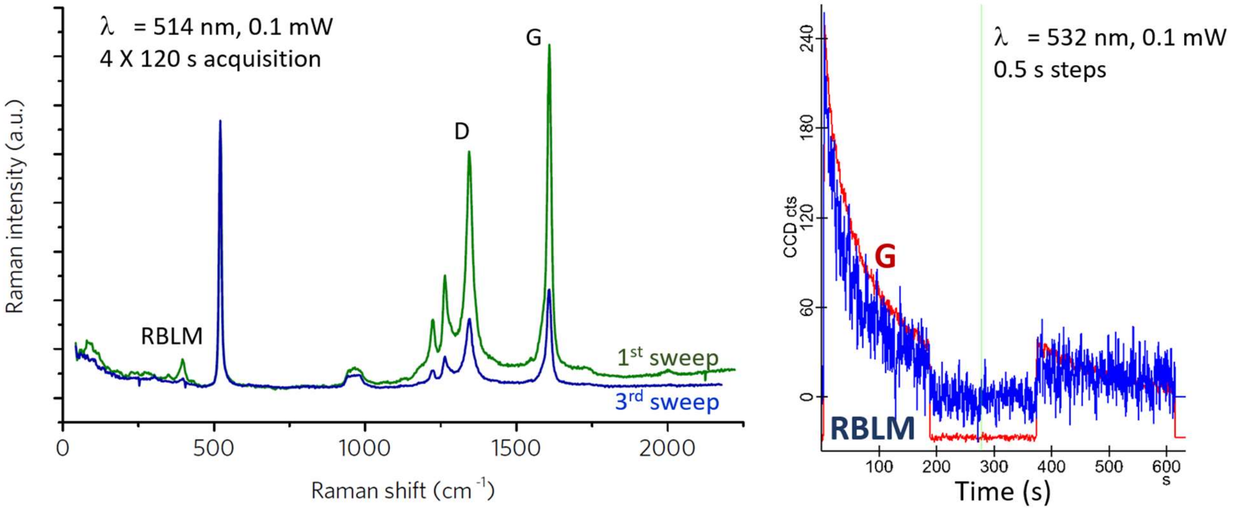

Figure 4.5 | GNR degradation during Raman acquisition. (a) First and third Raman spectrum of 7AGNRs on Si/SiO_2 shows degradation due to the laser excitation. (b) Raman peak intensity drops exponentially fast in the first 200 seconds or so. This must be minimized to obtain a reliable peak normalization.

While the peaks in the Raman spectrum of GNRs are expected to be non-dispersive, their amplitudes will change as the Raman excitation energy is varied due to the discrete nature of the excitonic transitions in the GNR. The Raman amplitude will peak when the excitation energy is near an optical absorption (with a difference of the phonon energy). Tracking the Raman amplitude by varying the excitation energy is called resonant Raman spectroscopy. Resonant Raman spectroscopy is significantly more challenging than standard Raman spectroscopy since it typically requires use of multiple laser sources (to obtain required linewidth and brightness) as well as realignment of the optics after every scan. Another challenge in characterizing GNRs with Raman is the degradation of GNRs under illumination, as shown in Figure 4.5. The effect of degradation is minimized by confirming sample uniformity and then averaging the spectra over multiple spots on the sample.

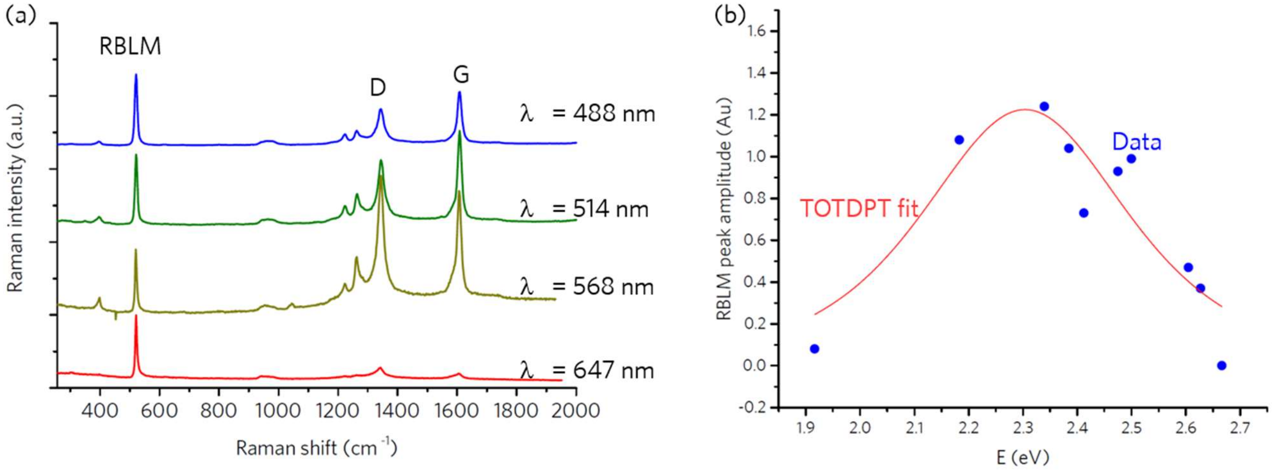

Figure 4.6 | Resonant Raman spectroscopy of 7AGNRs. (a) The Raman spectra intensity varies strongly for various excitation wavelengths in the visible range. (b) Resonant Raman profile taken from the RBLM peak amplitude in (a) with a third-order time dependent perturbation theory (TOTDPT) fit that shows a peak centered at around 2.3 eV, corresponding to the first optical transition in the 7AGNR.

A surface-grown 7AGNR sample was transferred to SiO_2/Si and characterized with Raman spectroscopy. As shown in Figure 4.6, the intensity of the Raman spectrum changed with varying excitation energies. By tracking the RBLM peak intensity versus excitation energy, the plot in Figure 4.6 is obtained. The peak is broad mainly due to the inhomogeneous broadening in the sample. The doping and length variations of GNRs along the sample can affect the optical transition energies. Length can affect optical transitions because ultra-short GNRs (<10 nm) will confine electron into a quantum dot and will upshift optical transition energies. The peak center roughly corresponds to the first optical transition in the system which happens to be near 532 nm, a common laser wavelength used in Raman spectroscopy set-ups. In this case, this energy value lines up well with other optical experiments on surfaces and the calculated DFT-LDA value. The technique was also employed for samples with 9AGNRs and 13AGNRs but unfortunately these GNRs do not appear have an optical transition available within the range of energies available in the measurement system (1.9 eV-2.6 eV eV) as shown in Figure 4.7. Resonant Raman spectroscopy can probe the JDOS in the GNRs and as GNR growth becomes more uniform and controlled, resonant Raman could be used for understanding of electron-photon interactions in GNRs.

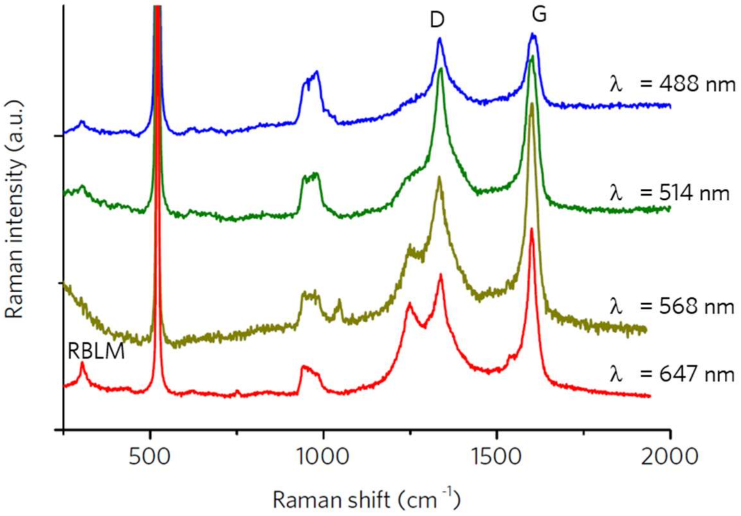

Figure 4.7 | Resonant Raman spectroscopy of 9AGNRs. Spectra peak height does not vary much over the range measured, indicating that 9AGNRs do not have an optical transition in this range.

4.5 Conclusion

The transport band gap of GNRs varies dramatically with the dielectric environment while the optical gap is less sensitive to the environment of the GNR. STS measures LDOS and it involves single electron transport in the GNR, and PLE and resonant Raman probe the JDOS which involves both electron and holes in the optical transitions in the GNR. The discrepancies in the experimental band gaps can be explained by theoretical calculations, such as DFT, and by an understanding of the effect of environmental screening on charge carriers in the GNR. The DFT with GWA approximation provides band gap values that are expected to be close to the values of the GNR band gap on insulators, which is critical for the understanding of the performance of the GNR devices described in the next chapters.

4.6 References

1. Shishkin, M. & Kresse, G. Self-consistent GW calculations for semiconductors and insulators. *Phys. Rev. B* **75,** 235102 (2007). https://doi.org/10.1103/PhysRevB.75.235102

2. Chen, Y.-C., de Oteyza, D. G., Pedramrazi, Z., Chen, C., Fischer, F. R. & Crommie, M. F. Tuning the Band Gap of Graphene Nanoribbons Synthesized from Molecular Precursors. *ACS Nano* **7,** 6123–6128 (2013). https://doi.org/10.1021/nn401948e

3. Ruffieux, P., Cai, J., Plumb, N. C., Patthey, L., Prezzi, D., Ferretti, A., Molinari, E., Feng, X., Müllen, K., Pignedoli, C. A. & Fasel, R. Electronic Structure of Atomically Precise Graphene Nanoribbons. *ACS Nano* **6,** 6930–6935 (2012). https://doi.org/10.1021/nn3021376

4. Yang, L., Park, C.-H., Son, Y.-W., Cohen, M. L. & Louie, S. G. Quasiparticle Energies and Band Gaps in Graphene Nanoribbons. *Phys. Rev. Lett.* **99,** 186801 (2007). https://doi.org/10.1103/PhysRevLett.99.186801

5. Denk, R., Hohage, M., Zeppenfeld, P., Cai, J., Pignedoli, C. A., Söde, H., Fasel, R., Feng, X., Müllen, K., Wang, S., Prezzi, D., Ferretti, A., Ruini, A., Molinari, E. & Ruffieux, P. Exciton-dominated optical response of ultra-narrow graphene nanoribbons. *Nat Commun* **5,** 4253 (2014). https://doi.org/10.1038/ncomms5253

6. Lawrence, J., Brandimarte, P., Berdonces-Layunta, A., Mohammed, M. S. G., Grewal, A., Leon, C. C., Sánchez-Portal, D. & de Oteyza, D. G. Probing the Magnetism of Topological End States in 5-Armchair Graphene Nanoribbons. *ACS Nano* **14,** 4499–4508 (2020). https://doi.org/10.1021/acsnano.9b10191

7. Wang, S., Talirz, L., Pignedoli, C. A., Feng, X., Müllen, K., Fasel, R. & Ruffieux, P. Giant edge state splitting at atomically precise graphene zigzag edges. *Nat Commun* **7,** 1–6 (2016). https://doi.org/10.1038/ncomms11507

8. Zhao, S., Barin, G. B., Cao, T., Overbeck, J., Darawish, R., Lyu, T., Drapcho, S., Wang, S., Dumslaff, T., Narita, A., Calame, M., Müllen, K., Louie, S. G., Ruffieux, P., Fasel, R. & Wang, F. Optical Imaging and Spectroscopy of Atomically Precise Armchair Graphene Nanoribbons. *Nano Lett.* **20,** 1124–1130 (2020). https://doi.org/10.1021/acs.nanolett.9b04497

9. Talirz, L., Söde, H., Dumslaff, T., Wang, S., Sanchez-Valencia, J. R., Liu, J., Shinde, P., Pignedoli, C. A., Liang, L., Meunier, V., Plumb, N. C., Shi, M., Feng, X., Narita, A., Müllen, K., Fasel, R. & Ruffieux, P. On-Surface Synthesis and Characterization of 9-Atom Wide Armchair Graphene Nanoribbons. *ACS Nano* **11,** 1380–1388 (2017). https://doi.org/10.1021/acsnano.6b06405

10. Brey, L. & Fertig, H. A. Electronic states of graphene nanoribbons studied with the Dirac equation. *Phys. Rev. B* **73,** 235411 (2006). https://doi.org/10.1103/PhysRevB.73.235411

11. Son, Y.-W., Cohen, M. L. & Louie, S. G. Energy Gaps in Graphene Nanoribbons. *Physical Review Letters* **97,** (2006). https://doi.org/10.1103/PhysRevLett.97.216803

12. Bachilo, S. M., Strano, M. S., Kittrell, C., Hauge, R. H., Smalley, R. E. & Weisman, R. B. Structure-Assigned Optical Spectra of Single-Walled Carbon Nanotubes. *Science* **298,** 2361–2366 (2002). https://doi.org/10.1126/science.1078727

13. Cai, J., Pignedoli, C. A., Talirz, L., Ruffieux, P., Söde, H., Liang, L., Meunier, V., Berger, R., Li, R., Feng, X., Müllen, K. & Fasel, R. Graphene nanoribbon heterojunctions. *Nat Nano* **9,** 896–900 (2014). https://doi.org/10.1038/nnano.2014.184

14. Vo, T. H., Shekhirev, M., Kunkel, D. A., Morton, M. D., Berglund, E., Kong, L., Wilson, P. M., Dowben, P. A., Enders, A. & Sinitskii, A. Large-scale solution synthesis of narrow graphene nanoribbons. *Nat Commun* **5,** (2014). https://doi.org/10.1038/ncomms4189

15. Fantini, C., Jorio, A., Souza, M., Strano, M. S., Dresselhaus, M. S. & Pimenta, M. A. Optical Transition Energies for Carbon Nanotubes from Resonant Raman Spectroscopy: Environment and Temperature Effects. *Phys. Rev. Lett.* **93,** 147406 (2004). https://doi.org/10.1103/PhysRevLett.93.147406

16. Bennett, P. B., Pedramrazi, Z., Madani, A., Chen, Y.-C., Oteyza, D. G. de, Chen, C., Fischer, F. R., Crommie, M. F. & Bokor, J. Bottom-up graphene nanoribbon field-effect transistors. *Applied Physics Letters* **103,** 253114 (2013). https://doi.org/10.1063/1.4855116

17. Vandescuren, M., Hermet, P., Meunier, V., Henrard, L. & Lambin, Ph. Theoretical study of the vibrational edge modes in graphene nanoribbons. *Phys. Rev. B* **78,** 195401 (2008). https://doi.org/10.1103/PhysRevB.78.195401

18. Verzhbitskiy, I. A., Corato, M. D., Ruini, A., Molinari, E., Narita, A., Hu, Y., Schwab, M. G., Bruna, M., Yoon, D., Milana, S., Feng, X., Müllen, K., Ferrari, A. C., Casiraghi, C. & Prezzi, D. Raman Fingerprints of Atomically Precise Graphene Nanoribbons. *Nano Lett.* **16,** 3442–3447 (2016). https://doi.org/10.1021/acs.nanolett.5b04183

5 Field effect transistors with atomically precise armchair graphene nanoribbons

The short length and wide band gap of chemically synthesized GNRs have prevented the fabrication of devices with the desired performance and switching behaviour. By fabricating short channel (L_{ch} ~20 nm) devices with a thin, high-κ gate dielectric and a 9-atom wide (0.95 nm) armchair GNR as the channel material, FETs with high on-current (I_{on} >1 μA at V_d = -1 V) and high I_{on}/I_{off} ~10^5 at room temperature are demonstrated. The performance of these devices is limited by tunnelling through the Schottky barrier (SB) at the contact and the transparency of the barrier is increased by maximizing the gate field near the contacts.

9AGNRs and 13AGNRs were studied in the development of high-performance FETs. With a predicted band gap of 2.10 eV for the isolated 9AGNR[1] and 2.35 eV for the 13AGNR[2], these are the narrowest band gap GNRs that have been synthesized on a surface with useful length for device fabrication (5AGNRs have a smaller band gap but are only ~10 nm long with current synthetic methods on Au(111)[3]). To synthesize the GNRs, the requisite monomer was evaporated onto a Au(111) surface under ultra-high vacuum and heated until it polymerized. Heating the substrate further causes individual polymers to planarize into GNRs, as detailed in Chapter 2. The high quality of the GNRs is verified by high-resolution scanning tunnelling microscope (STM) imaging as shown in Figure 5.1.

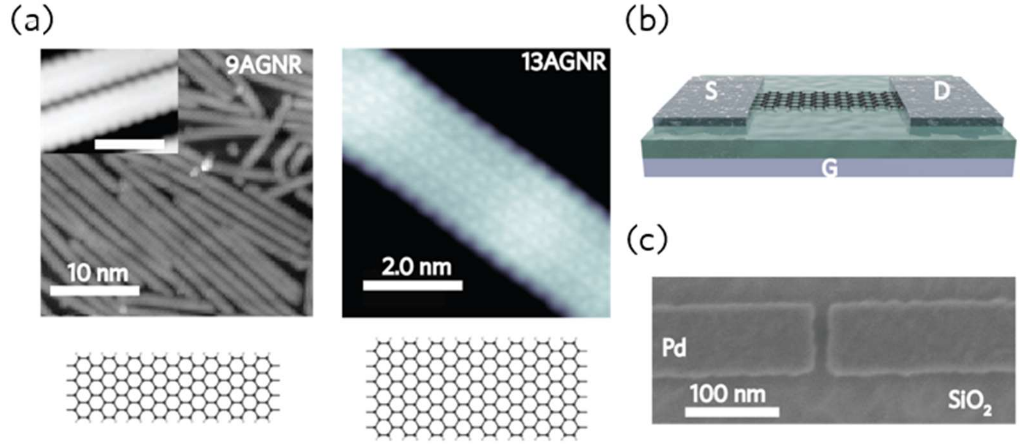

Figure 5.1 | High resolution STM GNR characterization and FET structure. (a) STM image of synthesized 9AGNR on Au (V_s = 1 V, I_t = 0.3 nA). Inset: High resolution STM image of 9AGNR on Au (V_s = 1 V, I_t = 0.5 nA) with a scale bar of 1 nm (b) High resolution STM image of 13AGNR on Au (V_s = -0.7 V, I_t = 7 nA). (c) Schematic of the short channel GNRFET with a 9AGNR channel and Pd source-drain electrodes (d) Scanning electron micrograph of the fabricated Pd source-drain electrodes.

9AGNRs are synthesized from 3',6'-dibromo-1,1':2',1''-terphenyl precursor monomers[1]. First, the Au(111)/mica substrate (200 nm Au; PHASIS, Geneva, Switzerland) is cleaned in ultra-high vacuum by two sputtering/annealing cycles : 1 kV Ar^+ for ten minutes followed by a 470 °C anneal for ten minutes. Next, the monomer is sublimed onto the Au(111) surface at a temperature of 60-70 °C, with the substrate held at 180 °C. After 2 minutes of deposition (resulting in approximately half monolayer coverage), the substrate temperature is increased to 200 °C for ten minutes to induce polymerization, followed by annealing at 410 °C for ten minutes in order to cyclodehydrogenate the polymers and form 9-AGNRs.

13AGNRs were synthesized using 2,2'-Di((1,1'-biphenyls)-2-yl)-10,10'-dibromo-9,9'-bianthracene building blocks.[4] Similar to the 9AGNR substrate, the Au(111)/mica substrate (200 nm Au; PHASIS, Geneva, Switzerland) is cleaned in ultra-high vacuum by two sputtering/annealing cycles : 1 kV Ar^+ for ten minutes followed by a 450 °C anneal for ten minutes. The monomer was sublimed at 222 °C onto the clean substrate held at room temperature. The sample was then slowly annealed stepwise to 340 °C to form 13AGNRs.

5.1 Fabrication of FETs with 50 nm back gates

Fabrication of GNRFETs requires the transfer of GNRs from the Au growth surface onto an insulating surface and subsequent device fabrication steps, as shown in Figure 5.1 and as described in Section 3.2. Unfortunately, standard imaging techniques (atomic force microscopy, scanning electron microscopy, transmission electron microscopy, etc.) were not useful in imaging single GNRs on insulating surfaces due to the GNR's small dimensions (~30 nm long, ~1 nm wide and <1 nm thick). Instead, Raman spectroscopy is performed in order to verify that the structural integrity of the GNRs is maintained throughout the transfer and device fabrication process. As shown in Figure 5.2, the Raman spectrum with 785 nm wavelength excitation of the processed 9AGNRs looks identical to the spectrum taken of the as-grown 9AGNRs on Au. The presence of the radial breathing-like mode (RBLM) peak (311.5 cm^{-1}) is evidence that the GNR width and edge structure is intact throughout device processing[5,6]. Unlike 9AGNRs, the RBLM is not visible for the 13AGNR spectrum for either 532 nm or 785 nm excitation wavelengths due to off-resonance of the excitation. Still, the 13AGNRFETs were processed with the same fabrication steps as the 9AGNRFETs and both types of devices exhibit similar transport characteristics Figure 5.3.

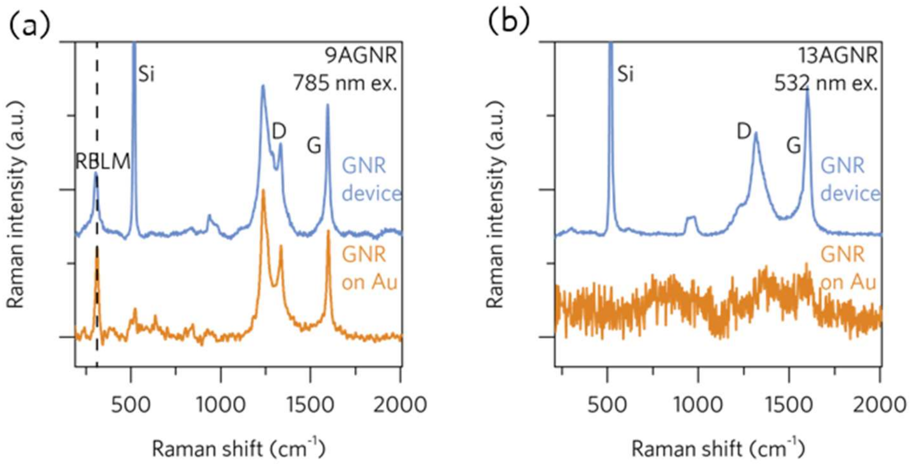

Figure 5.2 | Raman spectra of as-grown GNRs and after transfer. Raman spectra of (a) 9AGNRs and (b) 13AGNRs on the Au(111) growth substrate and after device fabrication shows that the GNRs remain intact. Since the excitation is off-resonance with the 13AGNR absorption, the Raman signal is weak on Au and the RBLM is not visible.

First, devices with a nominal 20 nm channel length and a 50 nm SiO_2 gate dielectric were fabricated as described in Chapter 3 and illustrated in Figure 5.3. Using identical fabrication recipes, two different types of devices were fabricated: one with 9AGNRs and one with 13AGNRs. After patterning ~300 pairs of electrodes in the transferred GNR area, each defined channel was biased and tested for gate modulation of the current to find devices bridged by a GNR. Of the 300 devices, 28 devices and 29 devices were successfully fabricated for 9AGNR and 13AGNRs, respectively. This ~10% ratio of bridged contacts to open devices indicates that almost all of the devices found contain one GNR in the channel as demonstrated by Figure 2.7.

Devices were first screened in ambient conditions using a cascade probe station and an Agilent B1500A parameter analyser. Vacuum and variable temperature measurements were then performed in a Lakeshore probe station. Ionic liquid devices were measured with a V_g sweep speed of 50 mV/s.

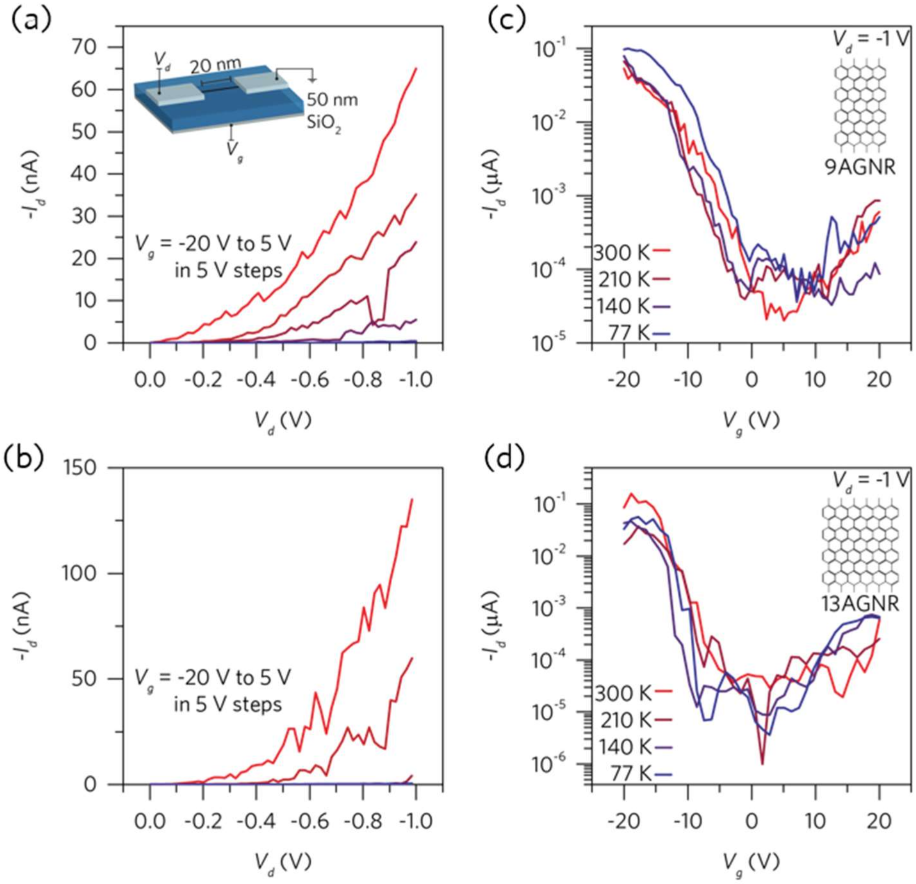

Figure 5.3 | Transfer characteristics of FETs with 9AGNRs and 13AGNRs. The presence of a SB is confirmed by non-linear current behaviour at low drain bias and lack of current saturation at high drain bias for both (a) 9AGNRs and (b) 13AGNRs. The weak temperature dependence in the I_d-V_g behaviour in (c) 9AGNRs and (d) 13AGNRs indicates that tunnelling through the Pd-GNR SBs is the limiting transport mechanism of the device.

5.2 9AGNRFET and 13AGNRFET characteristics and contact analysis

In SB devices (such as most FETs with one or two dimensional materials), the transport across the barrier can be limited by either thermionic emission, thermally assisted tunnelling, or direct tunnelling. All three effects can be present in a device, with one phenomenon dominating for different biasing conditions. Thermionic emission involves hot carriers on the source side contact overcoming the SB and drifting to the drain. The hot carriers follow a Boltzmann distribution, so a temperature dependence of $\log(I_d) \propto -1/T$ is evidence of thermionic emission and can be used to extract barrier height. Usually only devices with small or zero SB height show thermionic emission for most of the current range. In thermally assisted tunnelling, hot carriers that do not have enough energy to hop over the SB are able to drift to the drain after tunnelling near the top of the barrier, where it is thinner than near the Fermi level. The transfer curve will show some temperature dependence. Finally, direct tunnelling involves carriers near the Fermi level that directly tunnel across to the GNR and drift to the drain. Depending on the shape of the barrier at the contact, a device with a large SB will have suppressed thermionic emission and tunnelling effects will dominate as is the case for GNRFETs.

The 9AGNRFETs and 13AGNRFETs, as shown in Figure 5.3 and Figure 5.4, showed similar electrical behaviour due to their similar band gap. The presence of a SB at the Pd-GNR interface is evident by the non-linear behaviour at low bias in the $I_d - V_d$ characteristics, shown in Fig. 3a,b. To determine the contributions of thermionic vs tunnelling current across the SB, we measured the devices in vacuum at 77 K, 140 K, 210 K and 300 K. As demonstrated in Figure 5.3, there is no significant change in the characteristics at these different temperatures for either 13AGNRFETs or 9AGNRFETs and the off-state current is at the gate leakage level. The weak temperature dependence in the current-voltage characteristics suggests that the limiting transport mechanism is tunnelling through the barrier as opposed to thermionic emission over the barrier at the contacts. Furthermore, the ambipolar behaviour observed at low temperatures is only realistically possible with tunnelling contacts, since thermally activated current is suppressed for electrons in a semiconductor with a band gap of >2 eV. Tunnelling contacts with weak temperature dependence have been observed for carbon nanotube FETs and other low-dimensional materials and verified via simulations[7–9]. The SB height cannot be readily extracted for these devices since they are in the direct tunnelling regime for the current range measured. Thermionic emission would be expected. Unfortunately, the I_{on} = ~100 nA in the devices shown in Fig. 3 is too low for high-performance applications, so the transmission through the SBs must be enhanced to improve the current.

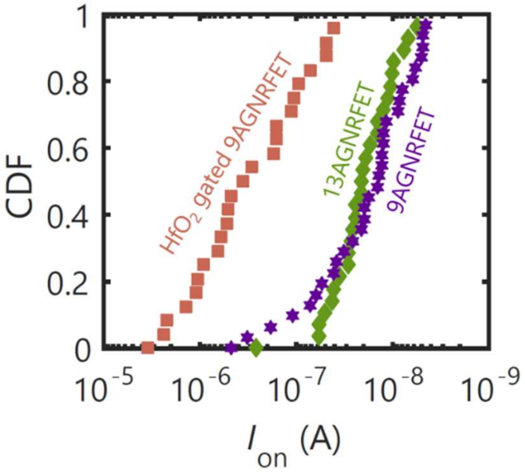

Figure 5.4 | Cumulative distribution function (CDF) of GNRFET I_{on}. I_{on} varies over an order of magnitude in 13AGNRFETs and 9AGNRFETs with 50 nm SiO_2 gate dielectrics and 9AGNRFETs with thin HfO_2 gate dielectrics. The CDF is defined as the total fraction of devices with on-current greater than the given value of I_{on}. Both 9AGNRFET and 13AGNRFETs have similar behavior due to the similar band gap and variations in on-state performance are most likely due to variations in the overlap length between the Pd and GNR and variations in the channel length.

An alternative parameter that affects the contact resistance in the device is the series resistance introduced by the short contact length in the device. This access resistance arises from the probabilistic nature of electron transmission from a contact to a material. It can be modelled as a transmission line made of resistors, where the parameters depend on the details of the materials used and the interface. The key parameter in the access resistance is the transfer length, L_T. The transfer length is the characteristic length where a contact length much larger than the transfer length will yield a minimum resistance that is independent of the access resistance. As the contact length decreases to values near the L_T, the resistance will increase as L_T / L[10]. The GNRs in the devices are short and the contact length is small as a result. It may be expected to have a large access resistance due to the small contact length. However, the transmission line model for access resistance does not accurately model transport in contacts with small lengths on the order of a few nanometers or edge contacts[11–13].

Edge contacts in CNTs show contact resistance that is lower than what is predicted by the transmission length model[12]. The CNT edge contact is formed by chemically bonding cobalt and carbon, enhancing the transmission of carriers into the CNT. Other work on ultra-short contact lengths in CNTs shows that the contact resistance of the lowest possible contact resistance in the CNT device with <10 nm long Pd-CNT contacts (like our Pd-GNR contacts)[13] is similar to the contact resistance of long contact and better than edge contact devices. The Pd-GNR contact length is also very short, so it follows that the contact resistance in the best GNR devices shown here is not limited by the short contact length, although it may be a limiting factor if the effect of the SB is minimized.

The power-law behaviour of the I_d - V_d curves indicates that the limiting factor is SB. The effect of the SB on the transmission must be mitigated to improve contact resistance and device performance. Lowering the SB via changing the contact metal or changing the material band gap could be viable options. However, both approaches prove challenging for the GNR devices given the yield constraints and difficulty in growing new types of narrow band gap GNRs. The yield in these devices is sensitive to the contact material used. If a contact material does not wet the GNR well or it has a thin oxide, it may not be able to contact the GNR sufficiently well at the short contact length, thereby not yielding a device. There is another way to improve the contact resistance in the GNR FETs: minimizing the contact resistance, which depends on the transmission probability across the barrier and can be enhanced by sharpening the barrier[14]. This is achieved in FETs with bulk semiconductors by degenerately doping the material under the contact. No suitable substitutional doping exists for GNRs due to their sensitivity to molecular structure. However, electrostatic doping is effective on the GNRs given their ultra-thin body. By modifying the gate stack with a high-k dielectric, the gate will naturally thin the barrier and improve conduction across the barrier, as shown in Figure 5.5.

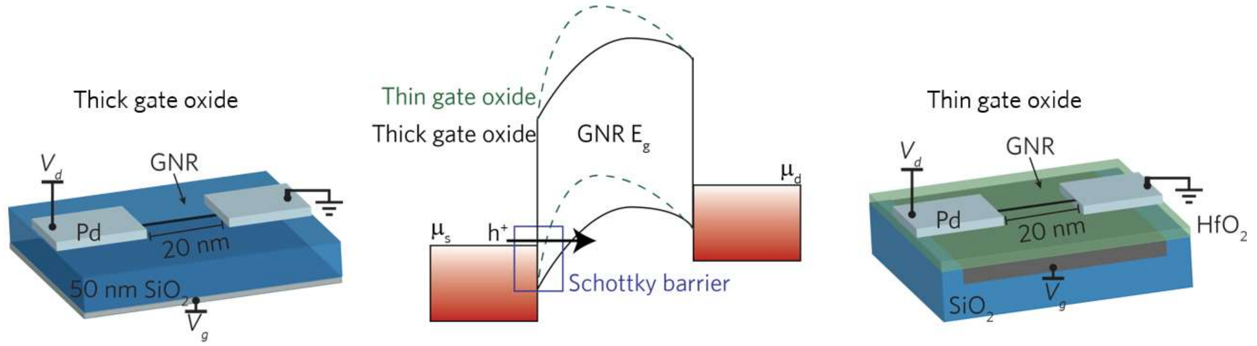

Figure 5.5 | Band diagram comparing devices with different gate oxide thickness. The gate stacks on thick oxide and silicon gate (left) and thin HfO_2 dielectric with metal back gate (right) determine the modulation of the SB width, which determines the tunnelling probability of holes in the device (middle).

5.3 Improving transmission across Schottky barrier via efficient electrostatic gating

Ionic liquid (IL) gating has been previously used to improve the transparency of the SBs in MoS_2[15]. Thus, we used the IL N,N-diethyl-N-(2-methoxyethyl)-N-methylammonium bis(trifluoromethylsulphonyl-imide (DEME-TFSI) to improve the electrostatic coupling between the gate electrode and the GNR channel, increase the field at the Pd-GNR interface and improve the transmission through the barriers. The $I_d - V_g$ behaviour of a 9AGNRFET with IL gating is shown in Figure 5.6. This device shows clear enhancement in the on-current to ~200 nA at -0.2 V drain bias (as opposed to 3 nA at -0.4 V for the 50 nm SiO_2 dielectric device presented in Figure 5.3). The transistor also switches at smaller gate voltages due to the high gate efficiency of the IL.

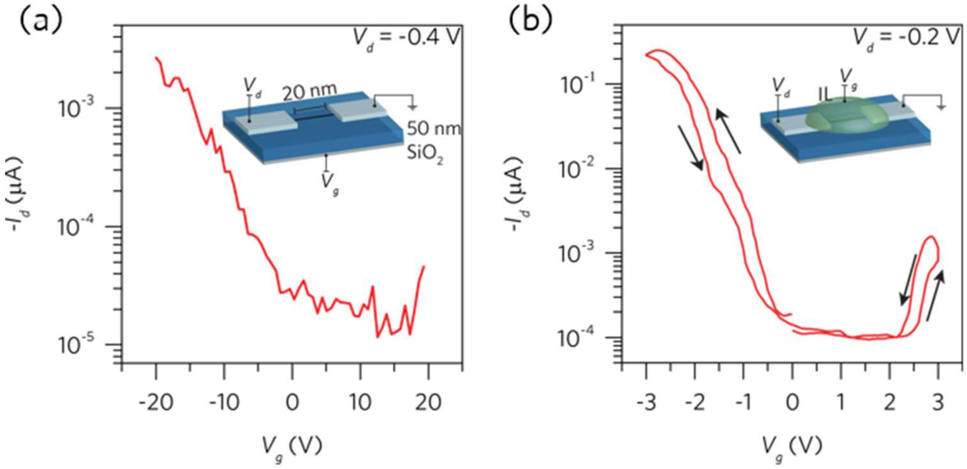

Figure 5.6 | Ionic liquid gating of a 9AGNRFET at room temperature. (a) I_d-V_g characteristics of the device gated by the thick 50 nm SiO_2 gate oxide (b) I_d-V_g characteristics of the device gated with the ionic liquid which shows clear ambipolar behaviour and improved on-state performance. Inset: ionic liquid (DEME-TFSI) gated 9AGNRFET device schematic.

Since solid dielectric gates are more suitable for large scale logic circuits, we fabricated scaled 9AGNR devices with a thin HfO_2 gate dielectric (effective oxide thickness of around 1.5 nm) as shown in Figure 5.7. HfO_2 local back gate device substrates were fabricated as described in Chapter 3. Resembling the IL device, the local HfO_2 back gate is more efficient at improving transmission through the SB than the thick SiO_2 global back gate[14]. As demonstrated by the I_d-V_g characteristics shown in Figure 5.7, the device exhibits excellent switching characteristics, I_{on}/I_{off} ~10^5, and a high I_{on} ~1 μA at V_d = -1 V[16]. This corresponds to a GNR-width (0.95 nm) normalized current drive of ~1000 μA/μm at -1 V drain bias, superior to previously reported top-down GNR devices[17–19]. Therefore, the scaled device structure with the improved gate efficiency allows for ultra-narrow bottom-up GNRs to outperform the narrow band gap top-down GNRs by mitigating the impact of the SBs on the contact resistance.

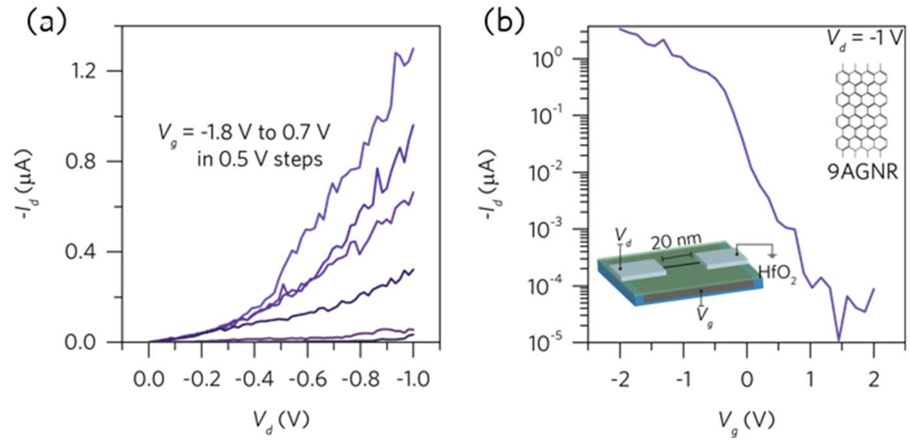

Figure 5.7 | Transfer characteristics of a scaled, high performance 9AGNRFET. (a) I_d-V_d characteristics of the scaled 9AGNRFET. (b) I_d-V_g of the devices show high I_{on} >1 ⌠A for a 0.95 nm wide 9AGNR and high I_{on}/I_{off} ~10^5. Inset: scaled 9AGNRFET schematic.

Thus, high performance short-channel FETs with bottom-up synthesized armchair GNRs are demonstrated. These GNRFETs have excellent switching behaviour and on-state performance after aggressively scaling the gate dielectric. Bottom-up GNR devices are therefore good candidates for high-performance logic applications, especially with advances in densely aligned GNR synthesis[20] as well as narrow band gap GNR growth[3]. The device fabrication methodology can be applied to other exotic device structures as well, such as tunnel FETs, which incorporate atomically precise GNR heterostructures[21–23].

5.4 Device yield and variability

Improving the yield of the GNR devices would enable more parameters to be varied in the device fabrication, including contact metal and device geometry. For instance, if the variability in contact length did not affect the device yield, the metal contact could be varied to find a contact that perhaps would perform better than Pd. Unfortunately, contact metals attempted so far either yielded no devices or did not show an improvement over Pd. This includes Au, Pt, Ti, Al, Cr, Ag, Co, among others. Varying the device geometry could entail integration of multiple gates or controllably changing contact length to experimentally verify how much the contact length affects (or does not affect) device performance. The devices shown in this chapter all were obtained with a yield of ~10%. This value depends on the length of the GNRs grown, transfer yield, and device geometry. Understanding how these parameters affect yield and optimizing them was an important part in yielding GNR devices.

A Monte Carlo simulation was used to estimate the number of GNRs in the device channels based on the device yield, GNR distribution, and channel length. Assuming a uniform spatial distribution of GNRs, the expected device yield and distribution of number of GNRs in the channel. The input parameters of the simulation were the GNR number density on the surface, GNR length, and channel length. Varying these parameters yields the plot shown in Figure 2.7. With the experimentally obtained yield of ~10%, the percentage of devices with more than 1 GNR in the channel goes as high as 8% for higher surface density and 4% for low surface density. Out of the devices with multiple GNRs, an insignificant percentage has more than 2 GNRs/channel. Thus, only 1-3 devices out of ~30 fabricated devices are likely 2 GNRs in the channel. However, due to the tendency for GNRs to be locally aligned to each other, as shown in the STM image, the number of GNRs in the channel is underestimate. The devices are not likely to account of the high tail end of the on-current distribution shown in Figure 5.4, since both GNRs would have to have good contact length under the Pd contacts to improve conduction over a single GNR channel with a large contact length or low contact resistance.

Understanding device yield also provides some insight into the device-device variability. As shown in Figure 5.4, the device on-current varies by more than an order of magnitude. The benefit of using atomically precise GNRs is supposed to be the improved control of device performance due to the “perfect” uniformity of GNR width and edge structure (i.e. band gap). While the data shown in Figure 5.4 appears to conclude that GNRs are not uniform, there are other factors that are likely to impact device to device variation that must be considered: FETs on the same CNT and with identical dimensions show large device-to-device variations[24].

Franklin, *et. al.* fabricated FETs with identical channel lengths and contact lengths on the same CNT[24]. They observed large device to device variation that cannot be explained by variations in CNT diameter. The variability is reduced when the surface is passivated with HMDS, indicating that the variability arises partly due to random traps on the surface of the oxide. Given the GNRFETs are also using bulk oxides, the variability due to this effect will be present even if the GNRs are perfect. The GNRFETs also do not have the same exact device geometry as each other. The channel length and contact length cannot be controlled in this process since it depends on randomly bridging an electrode gap with randomly oriented GNRs. Contact length and channel length variations correspond to large variations in performance given the small dimensions of the device. Finally, small defects could still be introduced during transfer or device processing which will affect performance depending on the distribution of those defects. Raman spectroscopy may not be sensitive to such defects.

5.5 Conclusion

The on-state performance of GNRFETs is improved by four orders of magnitude over the first reported 7AGNRs by exploiting the smaller band gap of 9AGNRs and integrating a thin, high-k local back gate that efficiently thins the barrier at the contact. Devices with 9AGNRs and 13AGNRs showed similar behavior, highlighting the counterintuitive, mod 3 dependence of ultra-narrow GNR band gap with atomic width. The device fabrication process can be implemented for any surface-grown chemically stable GNRs, which motivates the development of narrow band gap GNR synthesis. A SB limits transport at low bias causing a large contact resistance, so intrinsic transport properties of the GNR cannot be discerned from the SB devices in this chapter.

As narrow band gap GNRs are contacted and the SB becomes Ohmic, the current in the device will be mainly dominated by the properties of the channel, and the effects of contact and channel resistances can finally be decoupled. For example, if the carriers in the GNR have a longer mean free path than the channel length, then the device will show ballistic transport behavior as explained in the FET transport model in Section 8.3. Otherwise, devices with channel lengths longer than the mean free path will show diffusive transport and the carrier mobility could be extracted by fabricating devices with various channel lengths[10]. Therefore, experimental study of the intrinsic GNR transport properties requires GNRs with narrow band gaps to minimize the effect of the SB and long enough GNRs (> 50 nm) to yield devices with varying channel lengths to extract contact resistance and carrier mobility.

Devices with individual GNRs are an important step in the development of high-performance devices, but integration will likely require devices with parallel arrays of GNRs. Furthermore, the device yield and variability must also be improved to understand transport in the GNRs further and to take advantage of the molecular precision of the GNRs. Aligned GNRs can be used to both improve yield and to study a technologically relevant device configuration, where the device current scales with the electrode width.

5.6 References

1. Talirz, L., Söde, H., Dumslaff, T., Wang, S., Sanchez-Valencia, J. R., Liu, J., Shinde, P., Pignedoli, C. A., Liang, L., Meunier, V., Plumb, N. C., Shi, M., Feng, X., Narita, A., Müllen, K., Fasel, R. & Ruffieux, P. On-Surface Synthesis and Characterization of 9-Atom Wide Armchair Graphene Nanoribbons. *ACS Nano* **11,** 1380–1388 (2017). https://doi.org/10.1021/acsnano.6b06405
2. Yang, L., Park, C.-H., Son, Y.-W., Cohen, M. L. & Louie, S. G. Quasiparticle Energies and Band Gaps in Graphene Nanoribbons. *Phys. Rev. Lett.* **99,** 186801 (2007). https://doi.org/10.1103/PhysRevLett.99.186801

3. Kimouche, A., Ervasti, M. M., Drost, R., Halonen, S., Harju, A., Joensuu, P. M., Sainio, J. & Liljeroth, P. Ultra-narrow metallic armchair graphene nanoribbons. *Nat Commun* **6,** 10177 (2015). https://doi.org/10.1038/ncomms10177

4. Chen, Y.-C., de Oteyza, D. G., Pedramrazi, Z., Chen, C., Fischer, F. R. & Crommie, M. F. Tuning the Band Gap of Graphene Nanoribbons Synthesized from Molecular Precursors. *ACS Nano* **7,** 6123–6128 (2013). https://doi.org/10.1021/nn401948e

5. Verzhbitskiy, I. A., Corato, M. D., Ruini, A., Molinari, E., Narita, A., Hu, Y., Schwab, M. G., Bruna, M., Yoon, D., Milana, S., Feng, X., Müllen, K., Ferrari, A. C., Casiraghi, C. & Prezzi, D. Raman Fingerprints of Atomically Precise Graphene Nanoribbons. *Nano Lett.* **16,** 3442–3447 (2016). https://doi.org/10.1021/acs.nanolett.5b04183

6. Vandescuren, M., Hermet, P., Meunier, V., Henrard, L. & Lambin, Ph. Theoretical study of the vibrational edge modes in graphene nanoribbons. *Phys. Rev. B* **78,** 195401 (2008). https://doi.org/10.1103/PhysRevB.78.195401

7. Chen, Z., Appenzeller, J., Knoch, J., Lin, Y. & Avouris, P. The Role of Metal−Nanotube Contact in the Performance of Carbon Nanotube Field-Effect Transistors. *Nano Lett.* **5,** 1497–1502 (2005). https://doi.org/10.1021/nl0508624

8. Appenzeller, J., Radosavljević, M., Knoch, J. & Avouris, Ph. Tunneling Versus Thermionic Emission in One-Dimensional Semiconductors. *Phys. Rev. Lett.* **92,** 048301 (2004). https://doi.org/10.1103/PhysRevLett.92.048301

9. Perebeinos, V., Tersoff, J. & Haensch, W. Schottky-to-Ohmic Crossover in Carbon Nanotube Transistor Contacts. *Phys. Rev. Lett.* **111,** 236802 (2013). https://doi.org/10.1103/PhysRevLett.111.236802

10. Franklin, A. D., Farmer, D. B. & Haensch, W. Defining and Overcoming the Contact Resistance Challenge in Scaled Carbon Nanotube Transistors. *ACS Nano* **8,** 7333–7339 (2014). https://doi.org/10.1021/nn5024363

11. Wang, L., Meric, I., Huang, P. Y., Gao, Q., Gao, Y., Tran, H., Taniguchi, T., Watanabe, K., Campos, L. M., Muller, D. A., Guo, J., Kim, P., Hone, J., Shepard, K. L. & Dean, C. R. One-Dimensional Electrical Contact to a Two-Dimensional Material. *Science* **342,** 614–617 (2013). https://doi.org/10.1126/science.1244358

12. Cao, Q., Han, S.-J., Tersoff, J., Franklin, A. D., Zhu, Y., Zhang, Z., Tulevski, G. S., Tang, J. & Haensch, W. End-bonded contacts for carbon nanotube transistors with low, size-independent resistance. *Science* **350,** 68–72 (2015). https://doi.org/10.1126/science.aac8006

13. Pitner, G., Hills, G., Llinas, J. P., Persson, K.-M., Park, R., Bokor, J., Mitra, S. & Wong, H.-S. P. Low-Temperature Side Contact to Carbon Nanotube Transistors: Resistance Distributions Down to 10 nm Contact Length. *Nano Lett.* **19,** 1083–1089 (2019). https://doi.org/10.1021/acs.nanolett.8b04370

14. Franklin, A. D., Luisier, M., Han, S.-J., Tulevski, G., Breslin, C. M., Gignac, L., Lundstrom, M. S. & Haensch, W. Sub-10 nm Carbon Nanotube Transistor. *Nano Lett.* **12,** 758–762 (2012). https://doi.org/10.1021/nl203701g

15. Zhang, Y., Ye, J., Matsuhashi, Y. & Iwasa, Y. Ambipolar MoS2 Thin Flake Transistors. *Nano Lett.* **12,** 1136–1140 (2012). https://doi.org/10.1021/nl2021575

16. Llinas, J. P., Fairbrother, A., Barin, G. B., Shi, W., Lee, K., Wu, S., Choi, B. Y., Braganza, R., Lear, J., Kau, N., Choi, W., Chen, C., Pedramrazi, Z., Dumslaff, T., Narita, A., Feng, X., Müllen, K., Fischer, F., Zettl, A., Ruffieux, P., Yablonovitch, E., Crommie, M., Fasel, R. & Bokor, J. Short-channel field-effect transistors with 9-atom and 13-atom wide graphene nanoribbons. *Nature Communications* **8,** 633 (2017). https://doi.org/10.1038/s41467-017-00734-x

17. Jiao, L., Zhang, L., Wang, X., Diankov, G. & Dai, H. Narrow graphene nanoribbons from carbon nanotubes. *Nature* **458,** 877–880 (2009). https://doi.org/10.1038/nature07919

18. Li, X., Wang, X., Zhang, L., Lee, S. & Dai, H. Chemically Derived, Ultrasmooth Graphene Nanoribbon Semiconductors. *Science* **319,** 1229–1232 (2008). https://doi.org/10.1126/science.1150878
19. Wang, X. & Dai, H. Etching and narrowing of graphene from the edges. *Nat Chem* **2,** 661–665 (2010). https://doi.org/10.1038/nchem.719
20. Linden, S., Zhong, D., Timmer, A., Aghdassi, N., Franke, J. H., Zhang, H., Feng, X., Müllen, K., Fuchs, H., Chi, L. & Zacharias, H. Electronic Structure of Spatially Aligned Graphene Nanoribbons on Au(788). *Phys. Rev. Lett.* **108,** 216801 (2012). https://doi.org/10.1038/ncomms10177
21. Zhao, P., Chauhan, J. & Guo, J. Computational Study of Tunneling Transistor Based on Graphene Nanoribbon. *Nano Lett.* **9,** 684–688 (2009). https://doi.org/10.1021/nl803176x
22. Cai, J., Pignedoli, C. A., Talirz, L., Ruffieux, P., Söde, H., Liang, L., Meunier, V., Berger, R., Li, R., Feng, X., Müllen, K. & Fasel, R. Graphene nanoribbon heterojunctions. *Nat Nano* **9,** 896–900 (2014). https://doi.org/10.1038/nnano.2014.184
23. Chen, Y.-C., Cao, T., Chen, C., Pedramrazi, Z., Haberer, D., Oteyza, D. G. de, Fischer, F. R., Louie, S. G. & Crommie, M. F. Molecular bandgap engineering of bottom-up synthesized graphene nanoribbon heterojunctions. *Nat Nano* **10,** 156–160 (2015). https://doi.org/10.1038/nnano.2014.307
24. Franklin, A. D., Tulevski, G. S., Han, S.-J., Shahrjerdi, D., Cao, Q., Chen, H.-Y., Wong, H.-S. P. & Haensch, W. Variability in Carbon Nanotube Transistors: Improving Device-to-Device Consistency. *ACS Nano* **6,** 1109–1115 (2012). https://doi.org/10.1021/nn203516z

6 Field effect-transistors with dense, aligned graphene nanoribbons

Logic circuit designers control device dimensions to obtain the required performance out of individual circuit elements. Current increases in traditional FETs by increasing the width of the device, which can be used in the elements that will be driving large capacitances in the circuit. Control of device width in planar FETs is trivial. However, it remains a challenge to optimally integrate one dimensional semiconductors into devices that have current scaling with electrode width.

One dimensional semiconductors must be placed in parallel arrays with a optimize pitch, which poses the challenge of growing the material (or placing the material) with high spatial control. The optimal density in CNTs (and likely GNRs) is 200 CNTs/µm[1,2], where the GNR density is high enough to drive high current densities of >1 µA/mm but there is little CNT-CNT screening that hampers gate control. CNTs suffer from either being grown too sparsely aligned (e.g. on quartz), forcing the use of multiple transfer to obtain a decrease in pitch[3], or solution deposition techniques where the pitch is often too small which negatively impacts gate control[4]. GNRs grown on Au(111) are randomly oriented, as described in the previous chapters, but using a different type of surface, Au(788), has shown to yield parallel arrays of GNRs[5], albeit with a pitch that is likely too small (< 1nm or >1000 GNR/um). In the development of GNRFETs it is still important to integrate aligned growth into the process and to optimize the pitch by modifying the growth surface or growth conditions.

The GNR growth can be templated by the growth substrate. For instance, a mis-cut bulk Au crystal with a (788) surface contains aligned Au(111) steps with width of a few nanometers. Deposited GNR monomers on Au(788) are confined to polymerize along the direction of these steps, yielding GNRs that grow in parallel arrays as shown in Figure 2.5. Integrating GNRs grown on bulk Au requires the previously described device fabrication process with a major modification to the transfer process. The bulk Au is costly and difficult to replace so a transfer process must be implemented that preserves the integrity of the Au.

6.1 Aligned GNR transfer and device fabrication

Transfer techniques developed for GNRs grown on Au(111)/mica are not practical to for Au(788) bulk crystals. First, the Au(111) thin film serves as both a sacrificial and mechanical support layer. It is thin and mechanically flexible which enables the transfer process without a polymer. In contrast, the bulk Au(788) must be preserved for future growths due to its high cost and complex surface preparation. Fortunately, bulk crystals have been used for growth of graphene and other two dimensional materials and various transfer methods have been developed that aim to preserve the integrity of the growth substrate. One such method is the bubble transfer technique, first demonstrated to work on 7AGNRs grown on Au(788) by Senkovskiy, *et. al.*[6]. Figure 6.1 shows the bubble transfer process. First, the surface of the GNR/Au sample is coated by PMMA then placed in an electrolytic cell. The cell contains an electrolyte and a high work function counter electrode (Pt in this case). The Au and the Pt serve as the anode and cathode in the cell, respectively. As the electrodes are biased, electrons flow from the Au to the Pt, causing hydrogen gas to form at the surface of the Au via electrolysis. The hydrogen forms bubbles under the GNR/PMMA stack and delaminates it from the Au, leaving the Au surface (and crystal) intact. The GNR/PMMA film bubbles to the surface of the electrolyte and then is picked up with a clean Si substrate and placed in a sequence of DI baths to rinse off electrolyte and contaminants. Finally, the GNR/PMMA film is picked up with the target substrate and characterized with Raman spectroscopy.

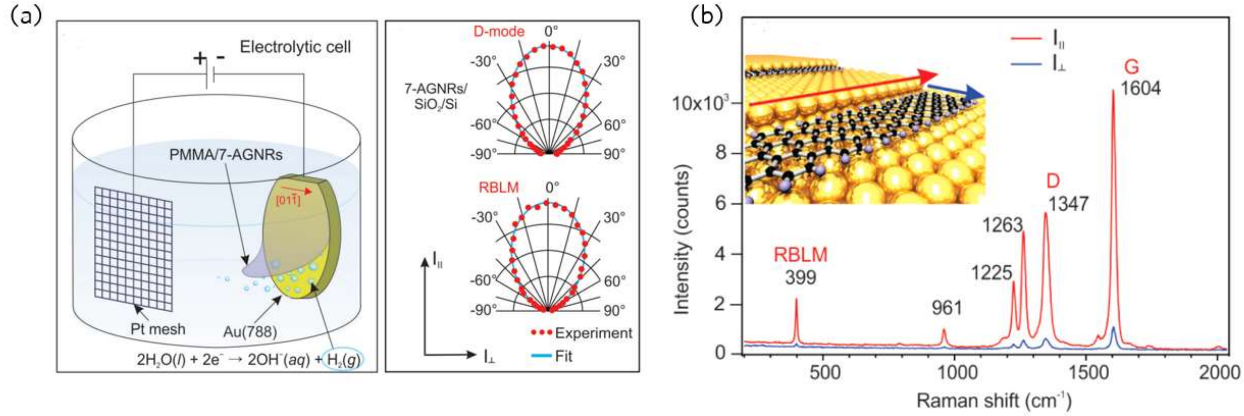

Figure 6.1 | Aligned GNR bubble transfer and Raman spectroscopy. (a) Bubble transfer of GNRs using a PMMA film as mechanical support and electrolytic cell to bubble hydrogen gas under the GNRs. (a, b) Strong polarization dependence in the Raman spectroscopy indicates GNRs are well aligned before and after transfer[6].

As described in section 4.4, optical absorption of 7AGNRs modulates the intensity of the Raman spectrum. One dimensional systems absorb optical energy depending on the linear polarization of the incoming light. Linearly polarized light along the GNR length absorbs more readily than linearly polarized light perpendicular to the GNR length. Zhao, *et. al.* exploited this to obtain the absorption spectra for various GNRs[7]. It follows that the Raman intensity will depend on the light polarization. As shown in Figure 6.1, polarized Raman on GNRs grown on Au(788) shows a strong polarization angle dependence. The angular dependence and overall peak integrity of the Raman spectrum is preserved during the GNR transfer process, indicating GNRs are transferred from Au(788) while maintaining their linear alignment.

Different types of aligned GNR samples were transferred to device substrates. Subsequently, electron beam lithography and lift-off was used to pattern source-drain electrodes with various electrode widths and electrically characterized and analyzed for width dependence. Devices showed some evidence of transport behavior that is limited by either electrostatic screening (7AGNRs) or GNR network transport (9AGNRs and 5AGNRs).

6.2 Transfer characteristics of FETs with parallel arrays of 7AGNRs

When a new type or GNR device fabrication process developed, 7AGNRs are the choice for the type of GNR used because of their strong Raman spectroscopy signal at 532 nm (a commonly used wavelength), widely available monomers, and simple growth that yields long GNRs. The development of FETs with aligned GNRs followed this idea by first demonstrating a growth and transfer process that yielded aligned arrays of GNRs on the surface as proven by polarized Raman spectroscopy. The device yield in the transferred area was close to 100%, illustrating the impact of integrating aligned GNRs. Transfer characteristics of a device with aligned 7AGNRs and a width of 200 nm is plotted in Figure 6.2.

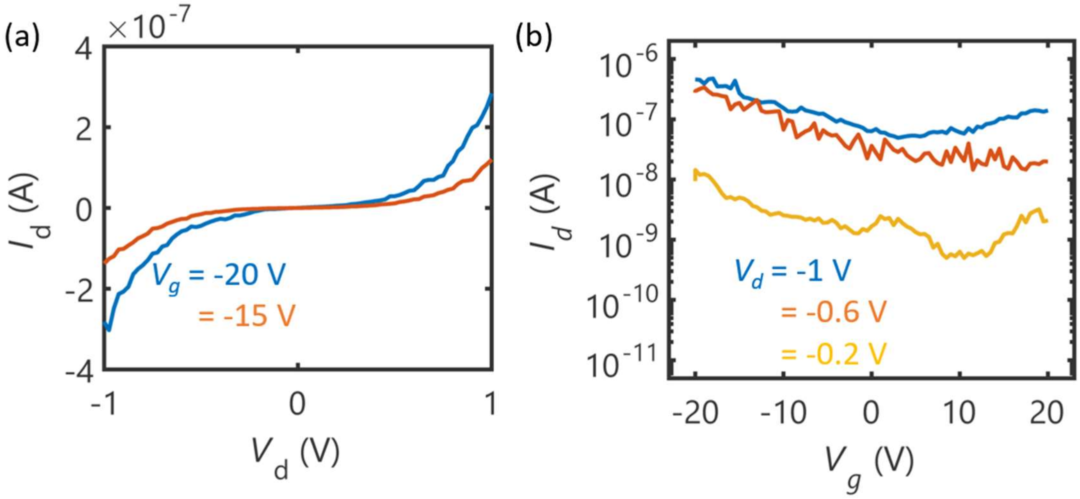

Figure 6.2 | Transfer characteristics of FETs with aligned 7AGNRs. (a) I_d-V_d characteristics of a ~20 nm channel length, 200 nm width, and 50 nm SiO_2 back gate and aligned 7AGNRs bubble transferred from Au(788). The power-law behavior indicates the current is SB limited. (b) I_d-V_g characteristics in the device show low on-off ratio due to likely GNR-GNR screening but high current from the parallel array of GNRs.

There is some current versus width dependence given that the current scaled with the device width, but the device-to-device variation remains large due to the issues described in Section 5.4. It is encouraging that the on-current scaled all the way to 100s of nA for devices with 200 nm width. Given the short pitch (< 1 nm) shown in Figure 2.5, as many as 200 could be present in the channel with each individual GNR contributing around 1 nA, the on-current in a FET with individual 7AGNRs. However, the on-off ratio of the aligned GNR devices is significantly smaller than that of the individual GNR devices: The aligned 7AGNR devices exhibit an on-off ratio that is around 10 while the individual 7AGNR devices exhibit an on-off ratio that is more than 10^3. The likely reason for this effect is GNR-GNR electrostatic screening of the gate. With such a short GNR-GNR pitch, charges in one GNR will modulate the potential of neighboring GNRs, mitigating the effect of the gate on those GNRs. This has the unintended consequence of decreasing the gate control in the device as shown in CNT devices with short pitch. Devices with CNT arrays with small pitch also show a degradation in on-off ratio. Simulations on CNT array FETs show that device performance is hampered by screening when the pitch < 5 nm[2]. Therefore, the Au surface or growth conditions may have to be modified to obtain films with 5 nm GNR pitch (200 GNR/um).

6.3 Transfer characteristics of 9AGNR and 5AGNRFETs

Both 5AGNRs and 9AGNRs have predicted band gaps of 1.6 eV and 2.1 eV respectively, significantly smaller than the wide 3.7 eV band gap of 7AGNRs[8]. The SB should be smaller in devices incorporating these ribbons than the 7AGNR and the on-state performance should improve as shown in Chapter 5. Furthermore, the smaller band gap of the 5AGNRs over the 9ANGRs should lead to devices that improve on the highest performing GNR devices reported in Chapter 5. The growth of 5AGNRs is more challenging than that of the 9AGNRs mainly due to difficulty in purifying the monomer and the monomer's interaction with the surface which both cause short GNRs that grow in small islands on Au(111), as shown in Figure 6.3. The longest GNRs are only up to 10 nm in length, so the standard GNR device fabrication with ~20 nm gaps is insufficient for contacting and yielding 5AGNR devices. The yield improves by growing aligned 5AGNRs on Au(788). As shown by the STM image in Figure 6.3, the growth of 5AGNRs on Au(788) causes the unusual effect of step bunching on the Au surface due to the interaction of the monomer with the surface.

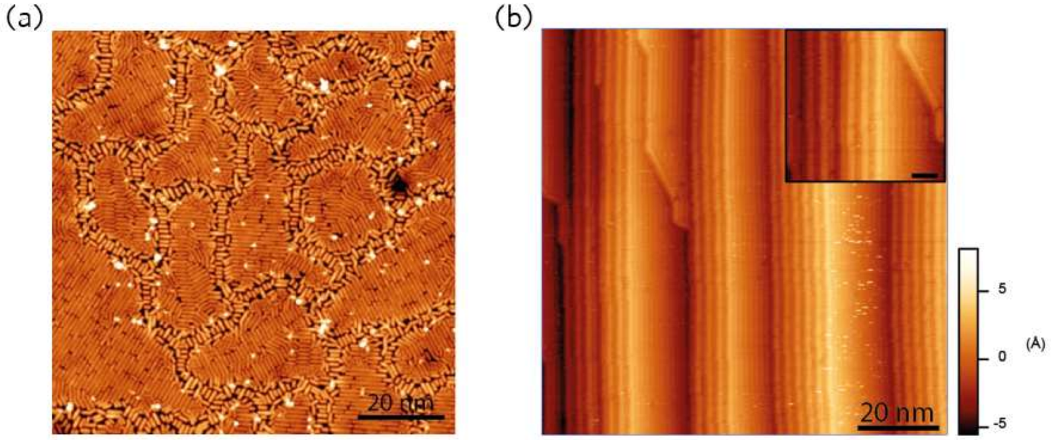

Figure 6.3 | STM of 5AGNRs grown on Au(111) and Au(788). (a) 5AGNRs grown on Au(111) arrange in small islands with individual GNRs being <10 nm long. (b) 5AGNR growth on Au(788) appears to grow uniform GNRs but the GNR length is difficult to measure due to the proximity of neighboring GNRs. Step bunching caused by the interaction of the 5AGNR molecule and the Au(788) surface is apparent.

5AGNRs were grown on Au(788), transferred to device substrates (with local back gates), and patterned in the same way as the 7AGNR devices. The transfer characteristics, shown in Figure 6.4, show on-current that is unexpectedly similar to that of the aligned 7AGNR devices, given the narrow band gap of the 5AGNRs. The devices also show higher on-off ratio than the 7AGNR devices, indicating that there might be a different transport mechanism at play where the on-off ratio is not affected by the GNR screening or the screening is not present in the 5AGNRs. The 5AGNRs are significantly shorter than the 7AGNRs, so it is likely that the GNRs in the channel are not bridging the electrodes, which would also explain the lower on-current. Finally, there is no apparent dependence in the on-current with the electrode width. To further study these effects, devices are fabricated with 9AGNRs which have a smaller band gap than 7AGNRs but could grow longer than 5AGNRs.

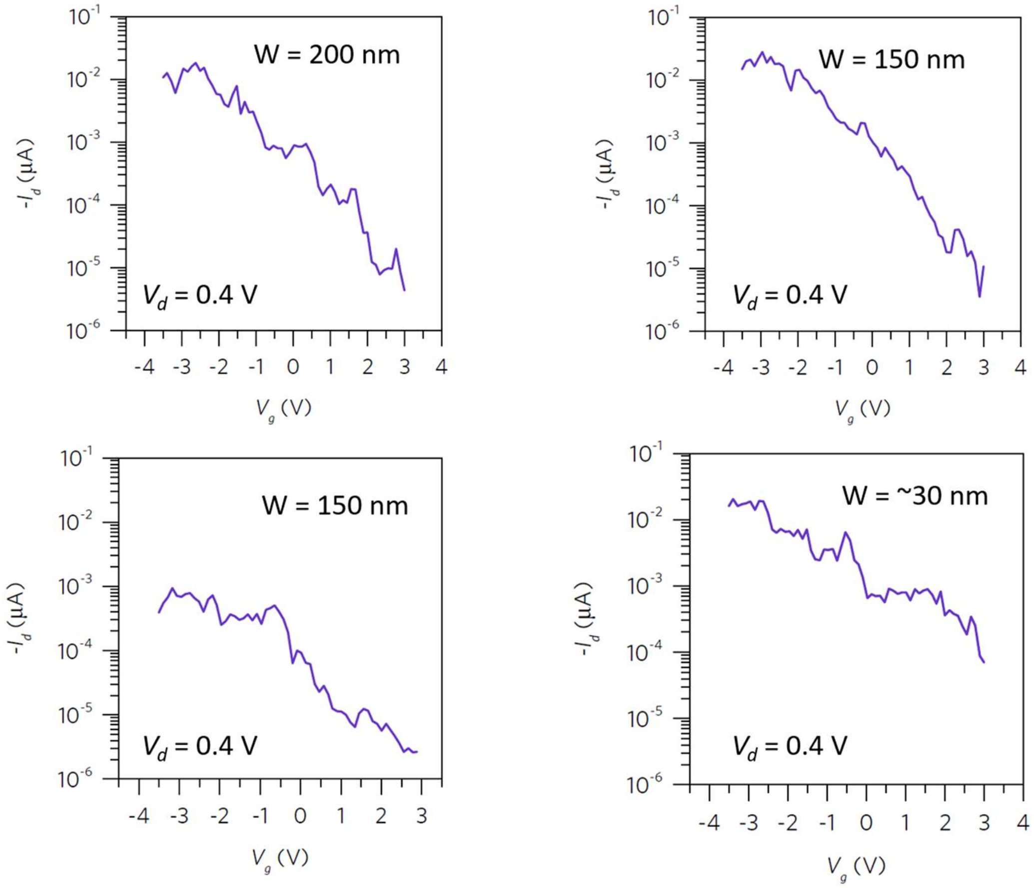

Figure 6.4 | I_d-V_g characteristics of FETs with aligned 5AGNRs. (a-d) Devices with varying electrode width show variation in on-current and switching behavior that does not show a clear dependence on the width of the device.

Aligned 9AGNRs are grown by similar conditions to the other types of GNRs on Au(788) then transferred to device substrates and patterned with electrodes of varying widths. As is the case for the 5AGNRs, the aligned 9AGNR devices show lower than expected on-current of ~1 uA and lower (but still relatively high) on-off ratio of 10^3, as shown in Figure 6.5. These devices may be in the middle ground of the 7AGNR and 5AGNR devices, where the length is longer than the 5AGNRs but shorter than the 7AGNRs. As a result, both the short length and screening could be playing a role in limiting the performance in these GNR devices. When the GNRs are short but aligned, it is still possible for charges to conduct from GNR to GNR as shown by Passi, *et. al.*[9], with transport going from band-like transport in a individual GNR to hopping-like (network) transport in the aligned GNR film. Looking at the device variability and modeling the yield in these devices provides some insight into how many single GNR bridges are expected in the ~20 nm channel and how that would affect performance.

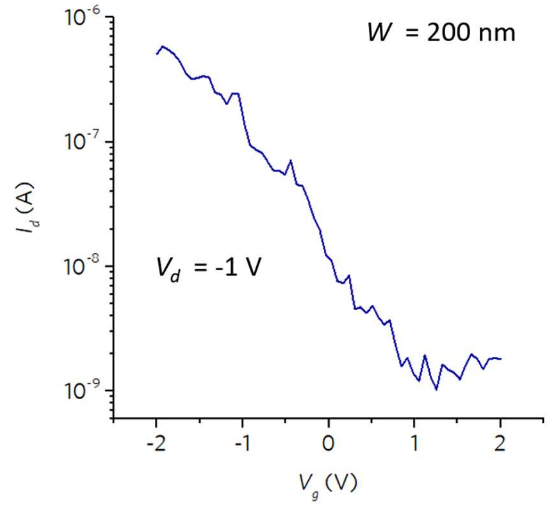

Figure 6.5 | I_d-V_g characteristics of a FET with aligned 9AGNRs. Devices with aligned 9AGNRs show lack of scaling behavior in on-current. For a 200 nm wide device, at least 10s of uA would be expected. Switching behavior is lower than the single GNR device but higher than the aligned 7AGNR devices.

6.4 Device yield and variability modeling

Ideally, there should be a linear dependence of the on-current versus the electrode width. The devices made with 7AGNRs show some dependence, but the devices made with 5AGNRs and 9AGNRs do not appear to show any relationship between electrode width and current. The statistics of on-current versus electrode width for 5AGNRFETs are plotted in Figure 6.6. The device-to-device variation of the on-current for a particular electrode width is already so large that it would be difficult to discern any current versus width relationship that may be present. Still, the average values of on-current taken over each electrode width does not show a clear trend. Furthermore, the 5AGNRs do not show an improvement in the on-current over the 9AGNRs as shown in Figure 6.6. The device to device variability could be arising from variations in contact length, line edge roughness in the electrode pattern, sensitivity to oxide traps, etc., like the device to device variation in individual GNR devices. However, another type of variation present in the aligned GNRs is the number of GNRs in the channel that bridge the electrodes. This value depends on the GNR length distribution and channel length and can be calculated by a Monte Carlo model similar to the one used for the yield calculations in Section 5.4.

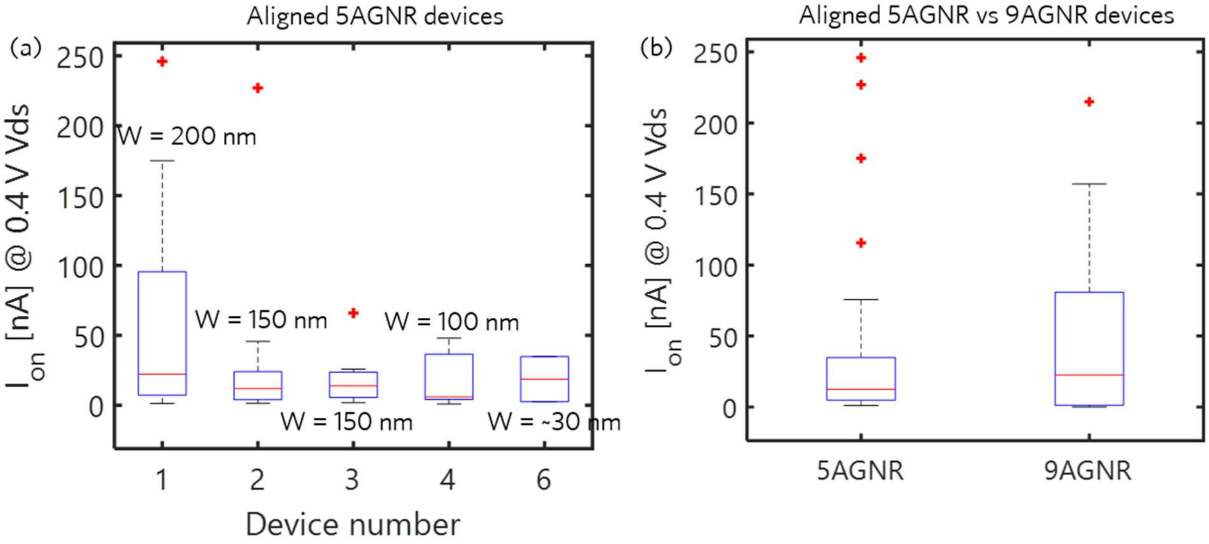

Figure 6.6 | Statistics of aligned 5AGNR and 9AGNR FETs. (a) 5AGNRFETs I_{on} distributions for different device widths. The red line corresponds to the median current, while the box bounds 25 and 75 percentiles with whiskers at 1 and 99 percentiles and red crosses signifying outliers. No clear dependence of current on device width is observed. (b) I_{on} distributions for aligned 5AGNR and 9AGNR devices show 9AGNR have higher I_{on}, which might be unexpected due to the narrow band gap of the 5AGNR.

The model used for the randomly oriented GNRs is modified so that the physical location and orientation in the gap of the GNR is fixed but a length distribution is modeled after the length distribution observed for 9AGNRs grown on Au(111). The length distribution of the 9AGNRs or 5AGNRs grown on Au(788) cannot be simply obtained from room temperature STM images since it is difficult to know when a GNR ends and the next one begins, effectively overestimating the length of individual GNRs. The experimental length distribution is fitted as an exponential distribution, like the one in Figure 2.7, and sampled for the Monte Carlo calculation. Number of GNRs that may bridge the gap depends on the electrode width and the GNR pitch. For simplicity, the pitch can be assumed to be small and the GNR density on the surface to be 1000/μm, as shown in the STM images of GNRs on Au(788). The number of successful GNRs in the channel is counted over multiple iterations to form the distribution of GNRs in the channel in the model, as shown in Figure 6.7.

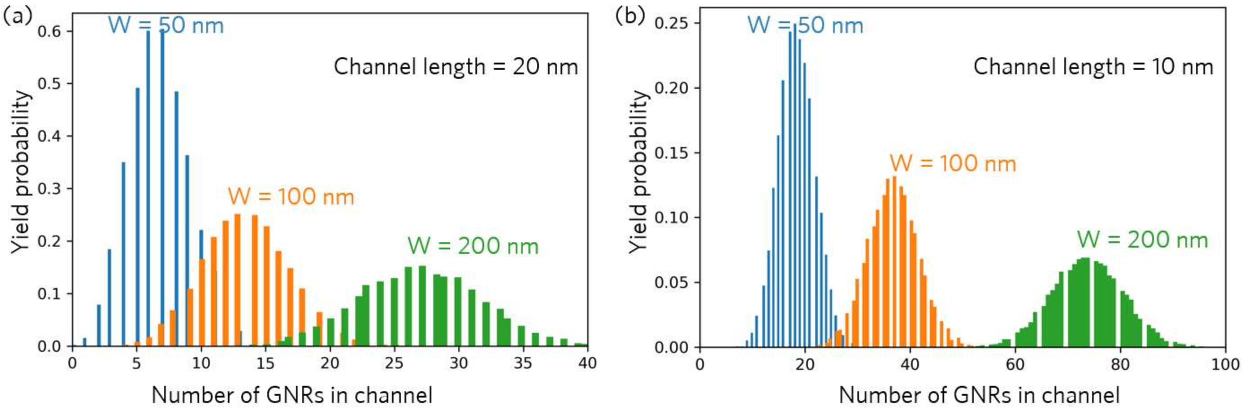

Figure 6.7 | Monte Carlo calculation of device yield with aligned GNRs. (a) The expected number of GNRs in the 20 nm channel increases linearly with electrode width, but the distributions overlap and if device to device variability is high, the variation may not be observed. (b) Distributions become significantly tighter and shift upward when the channel is scaled to 10 nm.

For the channel length of 20 nm, the devices have large variations of number of GNRs in the channel which will contribute further to the device to device variation discussed previously. The distribution of devices with various widths (50 nm, 100 nm, and 200 nm) overlap but the average value still depends on the electrode width. It is possible that the large intrinsic variation would broaden the distributions further and make it difficult to observe the width versus current relationship. Solving the large variation in number of GNRs bridging the gap could be done by improving the length distribution. However, the length distribution used in this calculation is already a best-case scenario length distribution in a growth that has been optimized. As an alternative, if the channel length can be scaled down to 10 nm instead of 20 nm, it may be possible to observe whether the length distribution is limiting the device performance and width dependence, as shown in Figure 6.7. The distribution peaks become tighter and the average GNRs in the channel increase as the channel length is reduced. The channel length is already optimized in the electron beam lithography and lift-off process used, but a different approach for patterning the gaps could potentially yield the desired 10 nm gaps.

6.5 Conclusion

Aligned GNRs can be grown by using a stepped Au(788) surface and then transferred via a bubbling technique that preserve the Au crystal. 7AGNR devices fabricated with aligned GNRs show improved on-current due to the increase in number of GNRs in the channel but the on-off ratio drops dramatically to ~10 due to the likely GNR-GNR screening present in the devices. For aligned 5AGNR devices that have much shorter GNRs, the transport may be limited by network transport, where the benefit of the smaller SB would not be observed due to the dominance of the GNR-GNR junction resistance. The 9AGNR devices likely contain GNRs that are longer than the 5AGNRs and shorter than the 7AGNRs, so both electrostatic screening and hopping transport may be present. Much longer GNRs need to be grown (> 50 nm) or shorter channels patterned (< 10 nm) to fully show that the length distribution is the limiting factor in these devices and not a process or other device issue.

Devices that have linear width versus current dependence are necessary for integration into logic systems, but the performance of the devices with individual GNRs must also be improved by using narrow band gap GNRs that limit the effect of the SB on the contacts.

6.6 References

1. Franklin, A. D. Electronics: The road to carbon nanotube transistors. *Nature* **498,** 443–444 (2013). https://doi.org/10.1038/498443a
2. Léonard, F. Crosstalk between nanotube devices: contact and channel effects. *Nanotechnology* **17,** 2381–2385 (2006). https://doi.org/10.1088/0957-4484/17/9/051
3. Shulaker, M. M., Pitner, G., Hills, G., Giachino, M., Wong, H.-S. P. & Mitra, S. High-performance carbon nanotube field-effect transistors. in *2014 IEEE Int. Electron Devices Meet.* 33.6.1-33.6.4 (2014). https://doi.org/10.1109/IEDM.2014.7047164
4. Cao, Q., Han, S., Tulevski, G. S., Zhu, Y., Lu, D. D. & Haensch, W. Arrays of single-walled carbon nanotubes with full surface coverage for high-performance electronics. *Nat. Nanotechnol.* **8,** 180–186 (2013). https://doi.org/10.1038/nnano.2012.257
5. Linden, S., Zhong, D., Timmer, A., Aghdassi, N., Franke, J. H., Zhang, H., Feng, X., Müllen, K., Fuchs, H., Chi, L. & Zacharias, H. Electronic Structure of Spatially Aligned Graphene Nanoribbons on Au(788). *Phys. Rev. Lett.* **108,** 216801 (2012). https://doi.org/10.1038/ncomms10177
6. Senkovskiy, B. V., Pfeiffer, M., Alavi, S. K., Bliesener, A., Zhu, J., Michel, S., Fedorov, A. V., German, R., Hertel, D., Haberer, D., Petaccia, L., Fischer, F. R., Meerholz, K., van Loosdrecht, P. H. M., Lindfors, K. & Grüneis, A. Making Graphene Nanoribbons Photoluminescent. *Nano Lett.* **17,** 4029–4037 (2017). https://doi.org/10.1021/acs.nanolett.7b00147
7. Zhao, S., Barin, G. B., Cao, T., Overbeck, J., Darawish, R., Lyu, T., Drapcho, S., Wang, S., Dumslaff, T., Narita, A., Calame, M., Müllen, K., Louie, S. G., Ruffieux, P., Fasel, R. & Wang, F. Optical Imaging and Spectroscopy of Atomically Precise Armchair Graphene Nanoribbons. *Nano Lett.* **20,** 1124–1130 (2020). https://doi.org/10.1021/acs.nanolett.9b04497
8. Yang, L., Park, C.-H., Son, Y.-W., Cohen, M. L. & Louie, S. G. Quasiparticle Energies and Band Gaps in Graphene Nanoribbons. *Phys. Rev. Lett.* **99,** 186801 (2007). https://doi.org/10.1103/PhysRevLett.99.186801
9. Passi, V., Gahoi, A., Senkovskiy, B. V., Haberer, D., Fischer, F. R., Grüneis, A. & Lemme, M. C. Field-Effect Transistors Based on Networks of Highly Aligned, Chemically Synthesized N = 7 Armchair Graphene Nanoribbons. *ACS Appl. Mater. Interfaces* **10,** 9900–9903 (2018). https://doi.org/10.1021/acsami.8b01116

7 Towards high performance FETs: narrow band gap graphene nanoribbons

Devices with narrow band gap (≤ 1 eV) GNRs would be anticipated to show Ohmic contact, high current, and ideal transfer characteristics. The devices shown in the previous chapters are all SB limited and integrate GNRs with wide band gaps, with the 5AGNR having the smallest band gap of 1.7 eV in vacuum[1]. In contrast, the highest performing CNTFETs show Ohmic contacts and ballistic behavior at low bias, taking advantage of narrow band gap CNTs (≤ 1 eV)[2]. Given the similarities in the electronic properties of CNTs and GNRs, narrow band gap GNRs must be integrated into devices to compete with the performance of state of the art CNTFETs. Tremendous progress has been made in the demonstration of armchair GNR synthesis, both on surface and in solution[3,4]. However, the narrow band gap armchair GNRs still remain a challenge to synthesize. Among the ultra-narrow GNRs, the GNRs belonging to the $3p + 2$ family are the most promising given their narrow band gap, but of their precursors pose significant synthesis challenges. Yet, on-surface synthesis teams have been able to engineer the electronic properties of GNRs by modifying a parameter other than the GNR width: the edge structure of the GNRs.

Notoriously, isolated zigzag edges in GNRs (and graphene), contain states that lie near the Fermi level[5]. Introduction of zigzag edges into GNRs then allows for these metallic states to interact and become the dominant states in the electronic transport in the GNR. These states happen to be topologically protected[6]. Specifically, GNR heterojunctions of different topological character will contain zigzag edges and metallic states at their interface. Various types of these topologically engineered GNRs (TE-GNRs) have been demonstrated and show relatively narrow band gaps when measured with STS[7–9]. Integration of TE-GNRs could lead to solving the large SB issue in the contact to the GNRs and finally unlock the intrinsic properties of the GNR for transport studies as well as development of high-performance logic devices. As will be presented here, unfortunately, topologically protected states appear to be chemically reactive, posing a significant challenge in fabricating devices while preserving the integrity of the TE states.

7.1 Band gap engineering using topological protected states in GNRs

7AGNRs measured with STS show a band gap of ~2.4 eV on Au but show a state near the middle of the gap at the zigzag ends of the GNR[10]. The state corresponds to an unpaired electron present at the zigzag edge of the GNR that arises from the zigzag edge symmetry. Recently, topological invariance was successfully used to explain the nature of this state[6]. Localized metallic states arise in the interface of two insulators with different topological invariance. The topological invariant in a one dimensional material ($\mathbf{Z}_2$) is either 0 for a topologically trivial material or 1 for a non-trivial material, which is determined by the termination in GNRs. At the interface of two materials where one has a $\mathbf{Z}_2$ of 0 and the other has a $\mathbf{Z}_2$ of 1, a metallic state will arise. 7AGNR with zigzag termination are topologically non-trivial materials that contain a metallic state at the ends since vacuum is a topologically trivial insulator. If, instead, the end of the 7AGNR was terminated with an armchair edge, the 7AGNR would be topologically trivial and would not host a metallic state. Then, embedding topologically protected states into GNRs narrows the band gap due to the metallic nature of these states.

In short GNRs with zigzag ends, the states at the ends will interact and cause splitting away from the Fermi level[10], similar to two electrons forming bonding/anti-bonding configurations when they are in close proximity. As the GNR gets longer, the interaction energy from one zig zag end to the other decreases and causes the splitting to decrease. This effect was not well understood when the growth of 5AGNRs was first reported[11]. As a result, the authors assigned the band gap of the GNR to correspond to the position of the interacting end states. The authors claimed the GNR to be almost metallic with a very small band gap of ~100 meV that should decrease even further as the GNR length is increased. However, the expected value of the bulk band gap in 5AGNRs from DFT-LDA calculations is ~500 meV and has been confirmed by STS on Au. The GNRs the authors measure is only ~2 nm long and the ends are zigzag. Therefore, it is more likely that the states closest to the Fermi level that are measured and assigned as the band edges arise from the topologically protected end states interacting[12]. In a long GNR, the interaction decreases, and the states may not contribute to the bulk conductive properties of the GNR. But, if topologically protected states are introduced throughout the GNR, the states will form a one dimensional chain of electrons that will form bonding/anti-bonding bands with properties depending on the periodicity and distance between states, creating TE-GNRs[7–9].

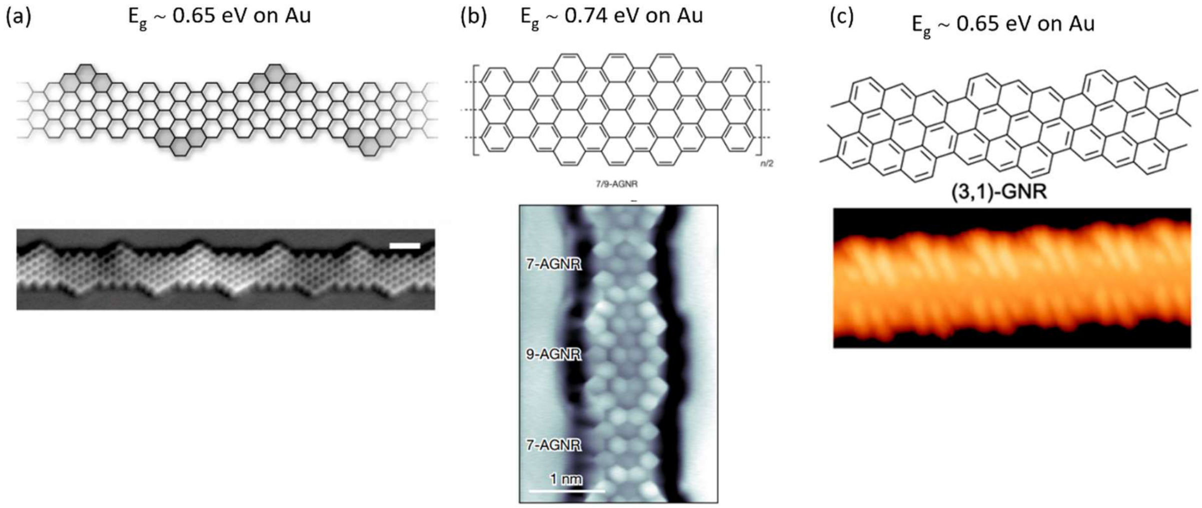

Figure 7.1 | STM of topically engineered GNRs. Narrow band gap GNRs have been developed with different approaches to topological band engineering: (a) super lattice of zigzag edges[9] (b) 7-9 AGNR superlattice with topologically protected states[8], and (c) chiral GNRs[7].

Various types of TE-GNRs have been synthesized since the topology theory of GNRs was first presented. Some examples of these GNRs are shown in Figure 7.1. The conduction and valence bands in TE-GNRs arise from the topologically protected states at the zigzag edges. Since the periodicity of the topologically protected states is longer (larger lattice constant) than that of the GNR backbone, the band properties of the GNR can be understood from the perspective of a superlattice, where the interface states form a minigap near the Fermi level and minibands of finite bandwidth. As the proximity of neighboring states decreases their interaction becomes stronger and the width of the minigap (the band gap) and the minibands increase. Effectively, the band structure of the GNR can be designed for a specific bandgap by tuning the periodicity of these states, providing an alternative technique to the synthesis of narrow band gap GNRs. TE-GNRs have a narrow band gap that can minimize the size of the SB at the TE-GNR-metal contact and the finite bandwidth could be exploited to create exotic superlattice devices, as discussed in Chapter 8.

7.2 Field-effect transistors with a TE-GNR

Most TE-GNRs that were integrating into the standard AGNR process did not yield any working devices. The topologically protected states at the zigzag edges are likely too chemically active and become passivated after removing the GNRs from their UHV growth chambers or during the device fabrication process where they come in contact with various solvents. One of the TE-GNRs that did yield working FETs is shown in Figure 7.1(a).

The TE-GNR was first synthesized on a standard Au(111)/mica substrate and imaged as shown in Figure 7.2. The band gap of the GNR using STS was measured to be 0.65 eV[9]. Then once the GNR was removed from the UHV chamber, Raman spectroscopy was performed over a period of a few days to track changes in the GNR structure over time. While the Raman spectrum did not change much over time, it is important to note that the Raman spectrum in GNRs might not be sensitive to small changes in the edge structure. For example, if molecules passivate the edges of the GNR, the Raman spectrum may not show visible changes. The TE-GNR could have chemically reacted as soon as it was removed from the STM chamber.

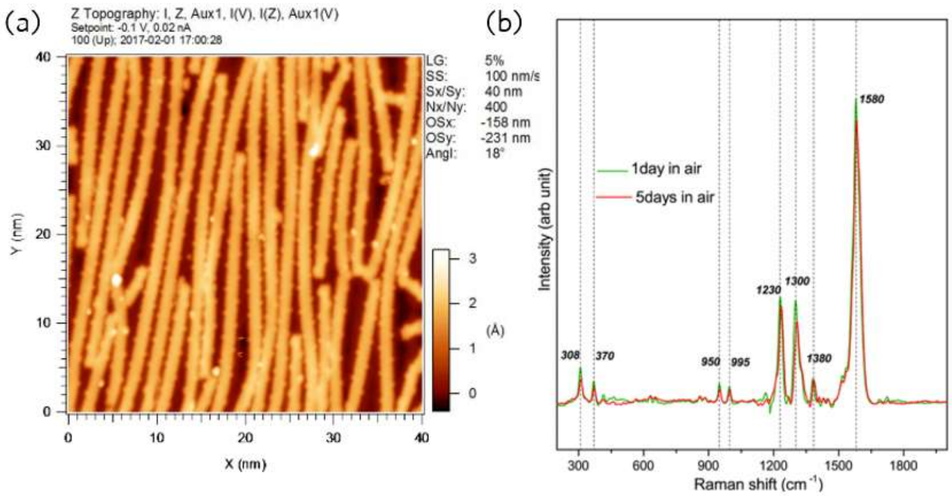

Figure 7.2 | TE-GNR STM and Raman spectroscopy for device fabrication. (a) Room temperature STM of the TE-GNR shows long GNRs, ideal for device fabrication. (b) Raman spectroscopy of the sample in (a) after removal and exposure to air remains stable.

After confirming the Raman spectrum is stable, the TE-GNR sample is then transferred to the device substrate with the standard HCl transfer shown in Chapter 3. Then, source-drain electrodes are patterned with the same process used for the fabrication of the AGNR devices in Chapter 5. The devices are then electrically characterized and analyzed.

7.3 TE-GNR FETs

Integration of the TE-GNR into the FET should provide a smaller SB at the contact and improved on-state performance. However, this was not the case for the TE-GNRFETs fabricated. As shown in Figure 7.3, the Raman spectrum is still present but the on-state performance of the GNRFET is poor, with an on-current of ~10 nA. With a smaller SB and pristine GNR, an on-current of ~10 uA would be expected. Most likely, the TE-GNR is more reactive than the pristine AGNRs, and the topologically protected states that form the frontier bands in the TE became passivated. The transfer curves also show a high on-off ratio which indicates that the GNR is still semiconducting. The device appears to still be SB limited and the on-current is significantly smaller than that of the best 9AGNRFET reported in Chapter 5. Instead, it appears closer to the performance of the 7AGNRFET, which contains 7AGNRs with a band gap of ~3.7 eV. This is not necessarily surprising if the structure of the TE-GNR is analyzed closely.

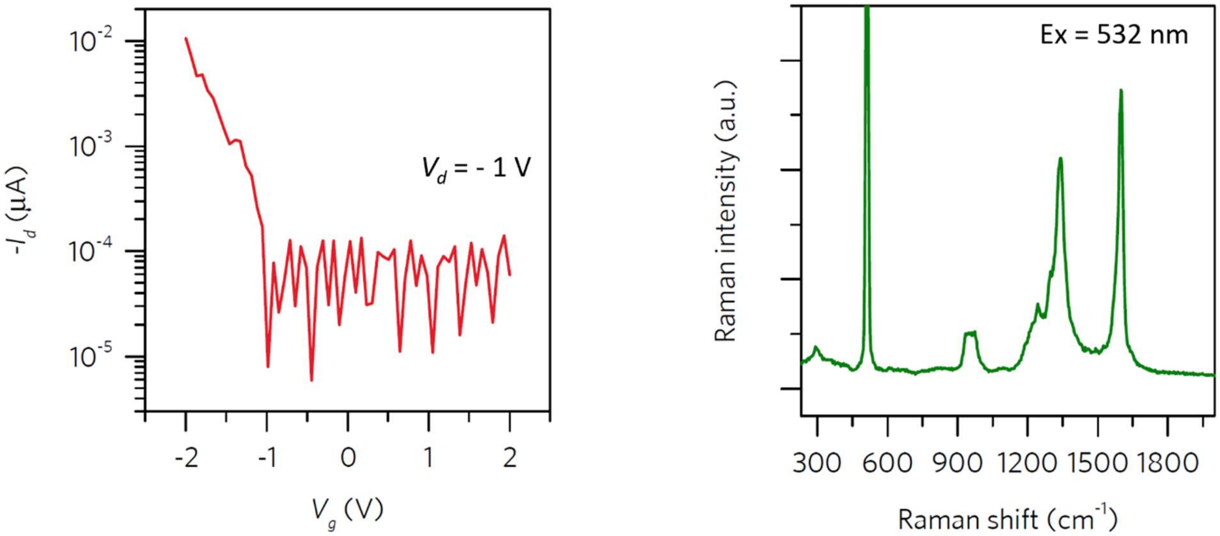

Figure 7.3 | TE-GNRFET transport characteristics. (a) I_d-V_g characteristics of the TE-GNRFET shows low on-current and moderate on-off ratio. The behavior is similar to that of the wide band gap 7AGNR. (b) Raman spectrum of the sample after device fabrication shows that the GNRs did not decompose to the point where the Raman spectrum would disappear.

Given that zigzag edges in GNRs and graphene are chemically reactive, it is possible that the zigzag edges that host the topologically protected states became passivated during the fabrication process. In Figure 7.4, the band structures of the TE-GNR is shown, where the conduction and valence bands correspond to the bands formed by the topologically protected states. The second conduction band and valence band correspond to the 7AGNR backbone. At some point after removal from UHV or during the fabrication process, these states reacted with air or solven molecules and no longer contribute to the TE bands. Therefore, the SB device would operate by having to inject charge into the transport bands which are now the bulk 7AGNR bands, and the SB height would be similar to the SB in the 7AGNRFETs. Then, it is not surprising that the on-state performance is almost the same of the 7AGNRFET.

In order to demonstrate high-performance FETs with TE-GNRs, the passivation of the topologically protected states must be prevented. This could involve designing a new type of TE-GNR that is not as chemically active. Although that may prove to be impossible if the chemical activity and the electronic character of the TE states are intrinsically linked. Another approach might be to design a new fabrication procedure that minimizes GNR exposure to air and solvents. This new process could involve a new GNR transfer in UHV or in a glovebox onto electrodes that are pre-patterned and planar. Unfortunately, the TE-GNRs may be reactive with trace amounts of atmospheric molecules and even a glove box process may be insufficient in preserving their electronic structure.

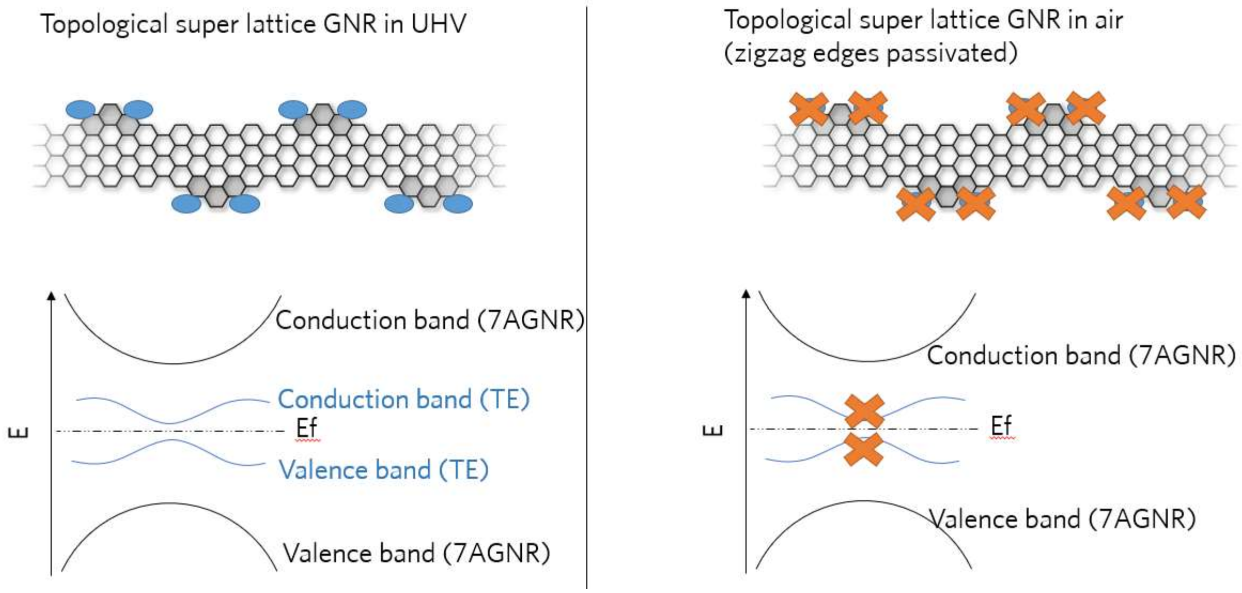

Figure 7.4 | Chemical passivation of TE bands. The narrow band gap of pristine TE-GNR arises from topologically protected states at the zigzag edges forming the two bands near the Fermi level (left). Once the sample is moved out of the UHV chamber, the zigzag edges likely react with molecules in the air that passivates their radical character (right), quenching the conductive bands near the Fermi level, and forcing charge conduction through the bulk 7AGNR bands.

7.4 Conclusion

Synthesis of narrow band gap AGNRs is challenging but new types of GNR morphologies that exploit the topological invariance of GNRs to create metallic states have shown to be promising. Various types of TE-GNRs have been developed but most do not yield devices with the standard GNR transfer and device fabrication process. The one type of TE-GNR that did yield devices shows poor on-current, which would not be expected for a narrow band gap GNR. It is likely that the topologically protected states are reacting as soon as removed from UHV or during device processing and becoming passivated. The GNR would lose its TE character and become a wide gap GNR, as was likely the case for the TE-GNR FET shown in this chapter. Other than the narrow band gap, the narrow bandwidth of the frontier bands offers a unique band structure for exotic devices. The narrow bandwidth arises from the superlattice nature of these GNRs and can theoretically be exploited to create sharp switching devices that show negative differential resistance, as shown in the next chapter.

7.5 References

1. Yang, L., Park, C.-H., Son, Y.-W., Cohen, M. L. & Louie, S. G. Quasiparticle Energies and Band Gaps in Graphene Nanoribbons. *Phys. Rev. Lett.* **99,** 186801 (2007). https://doi.org/10.1103/PhysRevLett.99.186801

2. Franklin, A. D., Luisier, M., Han, S.-J., Tulevski, G., Breslin, C. M., Gignac, L., Lundstrom, M. S. & Haensch, W. Sub-10 nm Carbon Nanotube Transistor. *Nano Lett.* **12,** 758–762 (2012). https://doi.org/10.1021/nl203701g
3. Talirz, L., Ruffieux, P. & Fasel, R. On-Surface Synthesis of Atomically Precise Graphene Nanoribbons. *Adv. Mater.* 6222–6231 (2016). https://doi.org/10.1002/adma.201505738
4. Narita, A., Feng, X., Hernandez, Y., Jensen, S. A., Bonn, M., Yang, H., Verzhbitskiy, I. A., Casiraghi, C., Hansen, M. R., Koch, A. H. R., Fytas, G., Ivasenko, O., Li, B., Mali, K. S., Balandina, T., Mahesh, S., De Feyter, S. & Müllen, K. Synthesis of structurally well-defined and liquid-phase-processable graphene nanoribbons. *Nat Chem* **6,** 126–132 (2014). https://doi.org/10.1038/nchem.1819
5. Nakada, K., Fujita, M., Dresselhaus, G. & Dresselhaus, M. S. Edge state in graphene ribbons: Nanometer size effect and edge shape dependence. *Phys. Rev. B* **54,** 17954–17961 (1996). https://doi.org/10.1103/PhysRevB.54.17954
6. Cao, T., Zhao, F. & Louie, S. G. Topological Phases in Graphene Nanoribbons: Junction States, Spin Centers, and Quantum Spin Chains. *Phys. Rev. Lett.* **119,** 076401 (2017). https://doi.org/10.1103/PhysRevLett.119.076401
7. de Oteyza, D. G., García-Lekue, A., Vilas-Varela, M., Merino-Díez, N., Carbonell-Sanromà, E., Corso, M., Vasseur, G., Rogero, C., Guitián, E., Pascual, J. I., Ortega, J. E., Wakayama, Y. & Peña, D. Substrate-Independent Growth of Atomically Precise Chiral Graphene Nanoribbons. *ACS Nano* **10,** 9000–9008 (2016). https://doi.org/10.1021/acsnano.6b05269
8. Rizzo, D. J., Veber, G., Cao, T., Bronner, C., Chen, T., Zhao, F., Rodriguez, H., Louie, S. G., Crommie, M. F. & Fischer, F. R. Topological band engineering of graphene nanoribbons. *Nature* **560,** 204–208 (2018). https://doi.org/10.1038/s41586-018-0376-8
9. Gröning, O., Wang, S., Yao, X., Pignedoli, C. A., Barin, G. B., Daniels, C., Cupo, A., Meunier, V., Feng, X., Narita, A., Müllen, K., Ruffieux, P. & Fasel, R. Engineering of robust topological quantum phases in graphene nanoribbons. *Nature* **560,** 209–213 (2018). https://doi.org/10.1038/s41586-018-0375-9
10. Wang, S., Talirz, L., Pignedoli, C. A., Feng, X., Müllen, K., Fasel, R. & Ruffieux, P. Giant edge state splitting at atomically precise graphene zigzag edges. *Nat Commun* **7,** 1–6 (2016). https://doi.org/10.1038/ncomms11507
11. Kimouche, A., Ervasti, M. M., Drost, R., Halonen, S., Harju, A., Joensuu, P. M., Sainio, J. & Liljeroth, P. Ultra-narrow metallic armchair graphene nanoribbons. *Nat Commun* **6,** 10177 (2015). https://doi.org/10.1038/ncomms10177
12. Lawrence, J., Brandimarte, P., Berdonces-Layunta, A., Mohammed, M. S. G., Grewal, A., Leon, C. C., Sánchez-Portal, D. & de Oteyza, D. G. Probing the Magnetism of Topological End States in 5-Armchair Graphene Nanoribbons. *ACS Nano* **14,** 4499–4508 (2020). https://doi.org/10.1021/acsnano.9b10191

8 Super-lattice graphene nanoribbon field effect transistors

The narrow bandwidth and narrow band gap in TE-GNRs and other types of super-lattice (SL) GNRs can be utilized to develop sharp switching transistors. One of the key challenges in advanced nanoelectronics for digital systems is developing transistors that can operate at very low voltage (well below 0.5 V) while maintaining a high on-off ratio, in order to engineer increasingly functional computing systems that operate at low power. This can enable more powerful mobile computing devices that run on batteries, swarms of wireless sensors that are scattered throughout an area or on the human body and run on energy scavenged from the environment, as well as more powerful supercomputers and data centers that do not require their own dedicated power plants.

A variety of efforts around the world are devoted to the development of heterostructure devices based on tunneling that can switch current with an on/off ratio of 10^4 and a sub threshold swing (SS) beyond 60 mV/dec (the theoretical limit in a MOSFET at room temperature). By developing a device that can switch efficiently in the order of 1 mV (~10^3 times better than today), the power consumption in logic circuits would be decreased by a factor of a million. However, successful demonstration of such devices has remained elusive. Compound semiconductor heterostructures have been extensively explored as candidates from the tunnel FET (TFET)[1]. However, even a few defects near the heterojunctions degrade SS to more than 60 mV/dec[2]. That is, controlled growth of semiconductors at the atomic scale is required in order to experimentally demonstrate the a viable TFET that lives up to this promise. Chemically synthesized GNRs offer significant promise as an alternative, where the GNR heterojuctions with atomic precision can be realized[3,4] by co-deposition of the precursor molecules as described in Chapter 2.

When the monomers of the 7AGNRs and 13AGNRs are co-deposited on a surface and annealed, copolymerization and cyclodehydrogenation yields heterostructure GNRs that have sections containing 7AGNRs and sections containing 13AGNRs, as shown in Figure 8.1. The band gap varies with the GNR width and the interface has theoretically zero defects. The heterostructures do not suffer from the high defect density present in heterostructure bulk semiconducting materials, such as III-V systems. Analogous to III-V heterojunction quantum wells, A GNR that has 7AGNR sections at the end and a 13AGNR section in the middle, as shown in Figure 8.1, serves as quantum dot, where the 7AGNR serves as the wide band gap barrier and the 13AGNR as the narrow band gap dot center. STS maps and theory show a state that lies bound to the dot with an energy lower than the 7AGNR conduction band, and a state that extends the length of the GNR with an energy higher than the conduction band. When an ensemble of bound states are placed along the GNR in a chain, they form bonding and antibonding bands that cause minibands and minigaps to form, similar to the bands in TE-GNRs that arise from bound topologically protected states. These type of GNRs are called super-lattice (SL) GNRs and can be synthesized on surfaces and in solution. Unlike TE-GNRs, the isolated, bound states have an energy that is higher than the conduction band of the quantum dot GNR element (not at mid-gap).

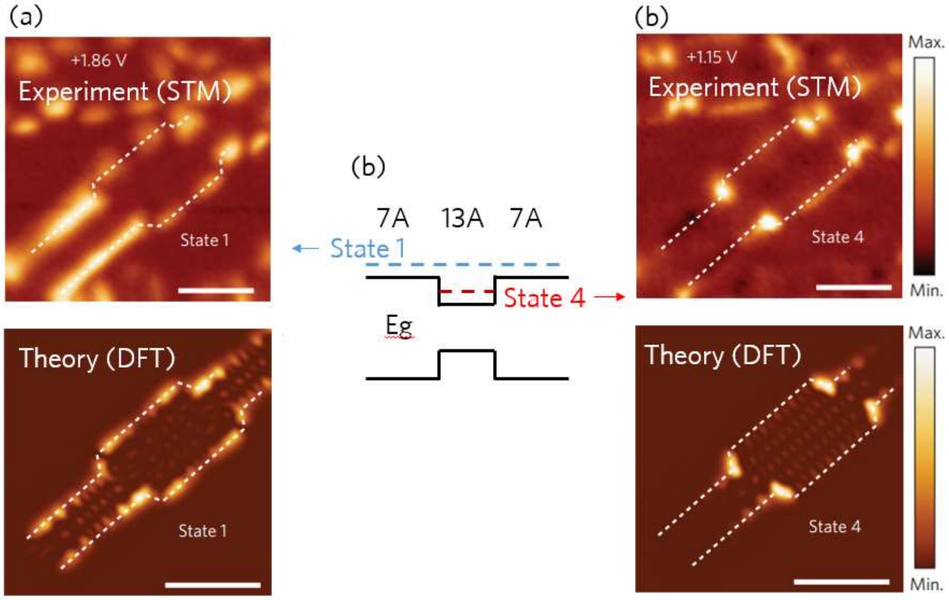

Figure 8.1 | 7-13-7 AGNR quantum dot. GNR quantum dot synthesized by co-deposition of 7AGNR and 13AGNR precursors during growth. (a,c) STS maps and DFT calculations showing a delocalized state (State 1) and a state bound to the 13AGNR section (State 2).[3] (b) Sketch of the band diagram of the heterostructure.

8.1 Band structure of SL-GNRs

A periodic potential with periodicity larger than that of the underlying material lattice causes the electronic bands in the material to split into minibands and minigaps. A hypothetical 7-13 AGNR superlattice would show this behavior. The bound states in neighboring 13AGNR sections interact and bond/anti-bond, forming minibands and minigaps. While the 7-13 AGNR superlattice has not been synthesized yet, various types of SL-GNRs have been demonstrated by including both units of the superlattice into the precursor. The first reported example was demonstrated at the same time as the first 7AGNR grown: the chevron GNR (cGNR).

The cGNR can readily be grown in solution[5] (like for the optical experiments performed in Chapter 4) and on a surface[4]. Both STS and DFT can be used to observe the superlattice properties of the cGNR[6]. In the conduction and valence bands, where quasi-infinite bands are expected, the bands split into minibands and minigaps, where the bandwidth corresponds to the periodicity of the chevron structure, as shown in Figure 8.3. The minibands and minigaps are on the order of 200 meV in the cGNR.

Minibands and minigaps in III-V bulk superlattices are often used in optoelectronic devices by engineering the epitaxial layer thickness of each subunit. In the case of the cGNR, the miniband

and minigap bandwidth is instead determined by the GNR precursor and the superlattice is in the lateral direction. Since all precursors are around the same size (~1 nm), the periodicity in most SL-GNRs will be similar and their miniband and minigap splitting on the order of 100s of meV. It turns out that the ultra-thin body of cGNRs allows for efficient electrostatic control, which is not easily attainable in bulk, superlattice III-V materials, and it enables superlattice nanoscale electronic devices that show sharp switching and negative differential resistance (NDR).

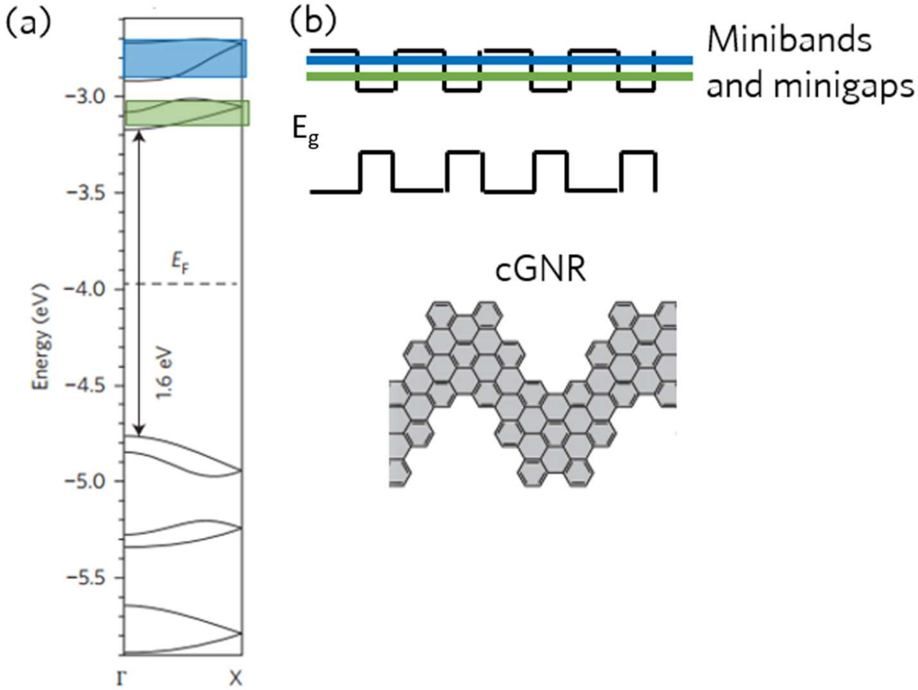

Figure 8.2 | Chevron GNR band structure. (a) DFT calculation of the band structure of a cGNR shows minibands (first conduction miniband in green, second conduction miniband in blue), with minigaps in between. The bands arise from bonding/antibonding of bound states along the GNR as shown in the band diagram in (b).

8.2 Atomistic calculations of a SL-GNR FET

The cGNRs have an intriguing electronic structure that arises from their super-lattice structure, but the band gap is >3 eV on an insulator. Contacting the cGNR will likely lead to large SB that will limit transport like it does in 7AGNRs. However, atomistic calculations such as, non-equilibrium Green's functions (NEGF), can be used to calculate the expected behavior in a device with cGNR with Ohmic contacts. A robust NEGF device calculation relies on a self-consistent calculation of the current and charge density in a material[7]. It is particularly useful for nanoscale devices that are expected to be in the ballistic transport regime, like GNR or CNT devices with short channel lengths. NEGF was used to calculate the transfer curves and density of states of the cGNRFET[8], as shown in Figure 8.3 and Figure 8.4. The cGNRFET simulated assumes perfect contacts and a n-doped source and drain regions, as well as an intrinsic channel with an ultra-thin high-k gate.

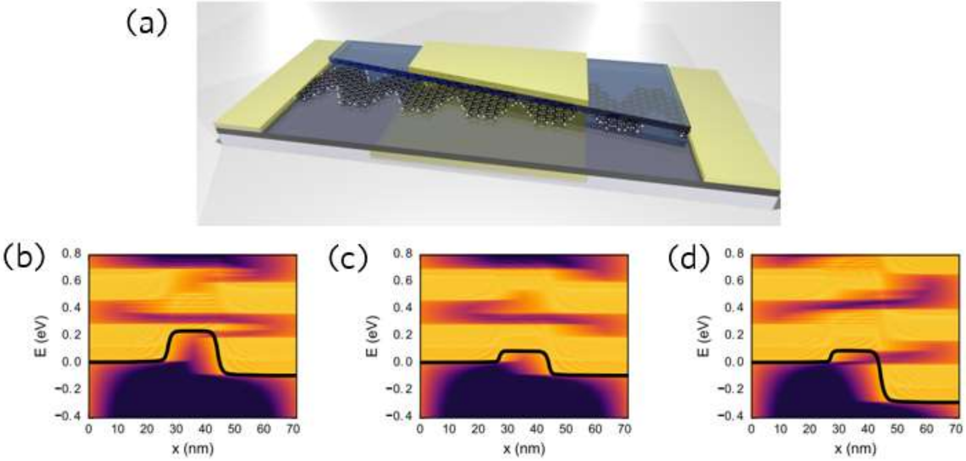

Figure 8.3 | DOS and device structure of a chevron GNR FET calculated via NEGF. (a)Double gate structure with nearly ideal gate control and doped source-drain regions simulated with NEGF. (b-d) Band diagrams showing the DOS (yellow is available states, black is forbidden states). Device is biased with (b) $V_g = 0.55$ V, $V_d = 0.10$ V, (c) $V_g = 0.70$ V, $V_d = 0.10$ V, and (d) $V_g = 0.70$ V, $V_d = 0.30$ V[8]. (a) The minigap on the drain side blocks leakage in the off-state, which leads to sharp switching. (c) The device is turned on and carriers can transmit from source to drain over the barrier. (d) Second miniband in the drain comes in resonance with the source leading to an increase in current after the first NDR valley.

The band diagram of the device under various biasing conditions is shown in Figure 8.3. At a low gate bias of 0.55 V and moderate drain bias of 0.10 V, the device is in the off-state and electrons populating states from the source side that are higher than the barrier cannot transport across the channel since there is no state available on the drain side. The minigap on the drain side lines up with the barrier, causing the states on the source and drain side to be off resonance, which filters the leakage current and leads to sharp switching behavior. As the gate bias is increased, the barrier is lowered and there are now populated states on the source side that can transmit electrons to the empty states on the drain side, turning the transistor on. As the drain bias increased, the minigap aligns with the source side states and the current decreases, leading to negative differential resistance (NDR), an effect not seen in traditional MOSFETs.

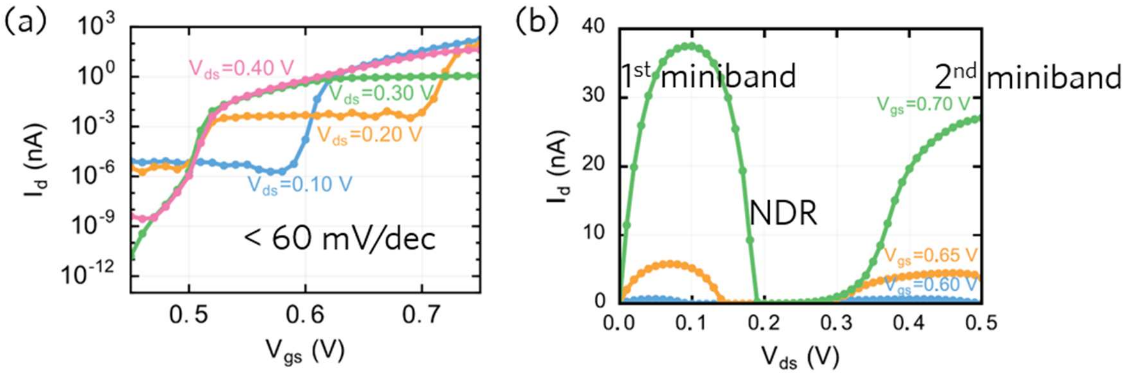

Figure 8.4 | NEGF calculation of transfer curves of chevron GNRFET. (a) I_d-V_g characteristics of the cGNRFET shows switching sharper than 60 mV/dec, with a threshold voltage dependent on the drain bias. (b) I_d-V_d characteristics show NDR as the first miniband comes off-resonance by applying a higher drain bias and an onset of a second peak corresponding to the second miniband coming on-resonance[8].

The transfer curves showing the various regimes are shown in Figure 8.4. Sharp switching (<60 mV/dec) and NDR can be observed in the I_d-V_g and the I_d-V_d curves, respectively. Sharp switching is intriguing for low-power logic applications since it enables transistors to operate at low voltage. NDR has many applications in analog circuits, where it can be exploited for high-gain stages at microwave frequencies. Practical sharp switching or NDR devices still require high on-current. However, the current values in the simulated FETs is small (~1 nA) because the device parameters are not optimal. Optimizing the device parameters is not practical using NEGF, since it is a costly calculation. Instead, an analytical model would be advantageous to understanding the underlying transport behavior, optimizing the device parameters, and providing a compact model for circuit simulations.

8.3 Analytical transport model using Landauer formalism

The first step in building the analytical model is picking a suitable theory that explains the transport behavior observed in the atomistic calculations. Landauer formalism accurately describes transport in ballistic materials sandwiched by two contacts by simply counting how many states in the material are injected by the left contact and how many states are injected by the right contact, at a specific bias[9]. The ballistic current in an arbitrary conductor can be modeled by

$$(8.1)\ I = -\frac{Me}{L}\left[\sum_{k_x>0,k_y} f_k v_k^x - \sum_{k_x<0,k_y} f_k v_k^x\right],$$

where M is the multiplicity of the band (2 for a single, spin degenerate band), L is the length of the conductor, k is the wave vector of the carriers in the material, f is the occupation probability given by the density of states and Fermi level of the contacts, and v is the velocity given by the band structure of the conductor. The left sum calculates the current injected from the left contact, while the right sum calculates the current injected from the right contact. As a positive bias is applied to the right contact, the chemical potential of the right contact drops and the probability of populating back-propagating states decreases, causing a net current from left to right.

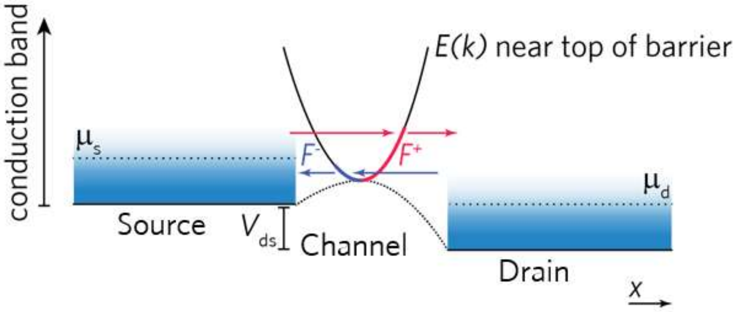

Figure 8.5 | Top of the barrier model band diagram. States from the source (drain) transmit to the drain (source) through bands in the *E*-*k* at the top of the barrier in the channel shown in red (blue). As the drain is biased, the back-injection of current decreases and a net current is flows through the device.

To illustrate this, the top-of the barrier (TOB) approximation can be used to model a transistor, which implies only the transport is limited by the band at the top of the barrier in the channel, as shown in Figure 8.5. States that populate the band from the left contact (the source) are assumed to all transmit to the right contact (the drain), and vice versa. The position of the TOB depends on the gate voltage. At positive gate bias, the barrier decreases. At a non-zero source-drain bias, there is a higher population of charges with positive wavevectors than with negative vectors, so a net electron current flows from the source to drain, as expected.

If the effective mass approximation is used by fitting parabolic bands to the band structure, the ballistic conductance, G_{max}, can be obtained in a two dimensional material from (8.1):

$$(8.2)\ G_{max,2D} \approx W\frac{2e^2}{h}\sqrt{\frac{2n_s}{\pi}} \propto \sqrt{m^*},$$

where n_s is the density of states and m^* the effective mass of the material. Not surprisingly, the maximum conductance increases linearly with width. It also increases with effective mass because the number of states (density of states) that can conduct increases. Furthermore, ballistic carriers do not scatter, so an increase in effective mass does not negatively impact transport as it does in diffusive transport.

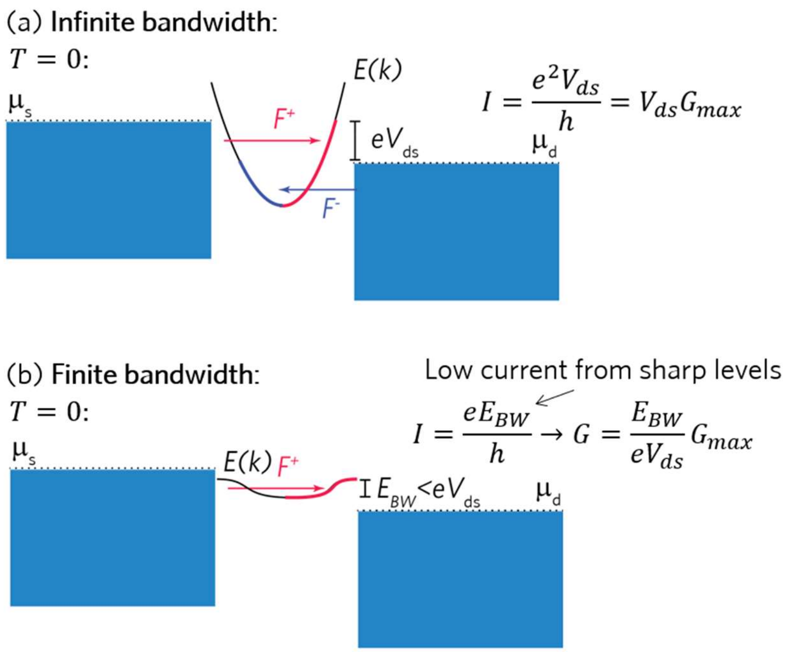

Figure 8.6 | Ballistic conduction through finite and infinite bandwidth at 0 K. (a)With a band that has infinite bandwidth, the maximum conductance at any drain bias is the quantum conductance and the current remains linear for sufficiently high gate bias. (b) The finite bandwidth case has a current that saturates once the drain bias overcomes the bandwidth.

For one dimensional semiconductors, such as GNRs, equation (8.1) has a closed form solution without the need for an approximation of the band structure. As shown in Figure 8.6, a ballistic one dimensional conductor at 0 K would have a maximum current corresponding to the quantum conductance limit, G_{max}, which is independent on the band structure of the material as long as there is a quasi-infinite band available for conduction:

$$(8.3)\ I = -\frac{Me}{h}\left[\int_E f(E-\mu_s)dE - \int_E f(E-\mu_d)dE\right] \to G_{max} = \frac{Me^2}{h},$$

where the integral is taken from the chemical potential of the right contact of the chemical potential of the left contact. For the case of the cGNR, the bands are finite and narrow. Therefore, at low bias the conduction follows the quasi-infinite band case. At higher bias, there is no more electronic bandwidth available for conduction and the current saturates as shown in Figure 8.6. The conductance saturates to

$$(8.4)\ I = \frac{eE_{BW}}{h} \to G = \frac{E_{BW}}{eV_{ds}} G_{max},$$

where E is the electronic bandwidth, and G_{max} is the ballistic limit of conductance[9]. That is, the maximum conductance per one dimensional channel. The final ingredient needed to capture the NEGF calculations is temperature dependence. The integral in (8.3) is given by

$$(8.5)\ \int f(E-\mu_s)dE = E - k_B T \log\left(e^{(E-\mu_s)/k_B T} + 1\right).$$

This closed form solution has the 0 K term minus the back-injection term introduced by the thermal carriers. Therefore, the current is given by

$$(8.6)\ I = -\frac{Me}{h}\left[k_B T \log\left(\frac{e^{(E-\mu_d)/k_BT}+1}{e^{(E-\mu_s)/k_BT}+1}\right)\right]_{Bottom\ of\ band}^{\text{Top of band}},$$

where E is evaluated from the bottom of the band to the top of the band. This relation is valid for any 1D ballistic channel if careful consideration is taken when determining the bounds of E and (8.6) is calculated for every sub-band. E is evaluated from 0 (or wherever the bottom of the band is defined relative to the chemical potentials) to infinity in the quasi-infinite band system, but it is evaluated from the bottom of the band to E_{BW} for the finite bandwidth system.

Using the closed form solution to the transport derived here and given in (8.6), the transfer characteristics of the cGNR device studied with NEGF can be calculated and compared to the atomistic results. The contacts are assumed to be doped cGNR sections with a Fermi level corresponding to the doping and the electrostatic properties of the device are ideal, with a perfect gate efficiency. The doping is taken to be identical to the doping in the NEGF calculation, where the Fermi level at the source and drain sits exactly on the conduction band edge. The electronic bandwidth is 272 meV taken from Figure 8.2. And the initial channel potential which defines the threshold voltage is 790 meV, just like in the NEGF calculation. As shown in Figure 8.7, the analytic model fits the NEGF calculation quite well with no fitting parameters used.

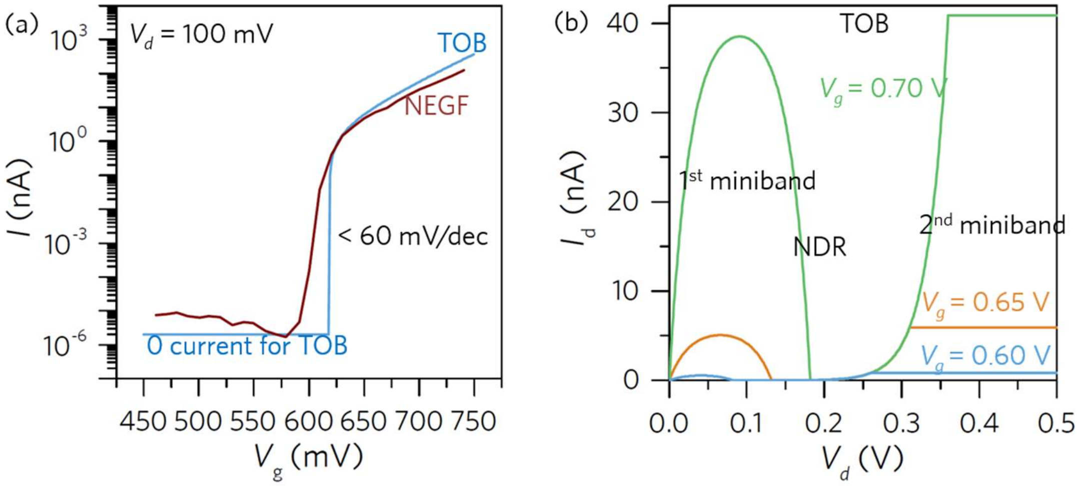

Figure 8.7 | Validation of analytical transport model of SLFET. (a) I_d-V_g characteristics of the cGNRFET calculated with the NEGF and the TOB model. (b) I_d-V_d characteristics of the cGNRFET calculated with the TOB model models shows the same current range and behavior as NEGF except for the current of the 2nd miniband, where perfect transmission from one sub-band to another is assumed in the TOB model. The models agree well except in parts of the subthreshold regime, where infinitely sharp band edges are assumed in the TOB model.

With a validated analytical model, the device parameters, such as bandwidth and doping, can be optimized. A more ideal SL-GNR could be one that has a single miniband near the Fermi level, far from the neighboring bands, since it would limit the influence the 2nd miniband could have on the conduction and prevent the steps in the I_d-V_g curve in Figure 8.4. Moreover, the bandwidth must be wide enough to support a large current. The boron "doped" 7AGNR fulfills these requirements. The structure and density of states of the GNR are shown in Figure 8.8. With a bandwidth of 200 meV arising from the boron superlattice, the maximum current this band can transmit is 15 μA, given by (8.4), and the band is mid-gap, near the Fermi level. The band diagrams of transistors operating using the miniband (SL-GNRFET) and a transistor operating using the bulk 7AGNR band (GNRFET behaving like a MOSFET) are shown in Figure 8.8 with optimized doping level at the contacts. The sharp switching in the SL-GNRFET is apparent as the subthreshold leakage is blocked by the gap on the drain side of the device. In the typical GNRFET, which behaves like a typical MOSFET, the quasi-infinite bands allow for transmission of leakage given by the Boltzmann distribution of carriers (60 mV/dec limit).

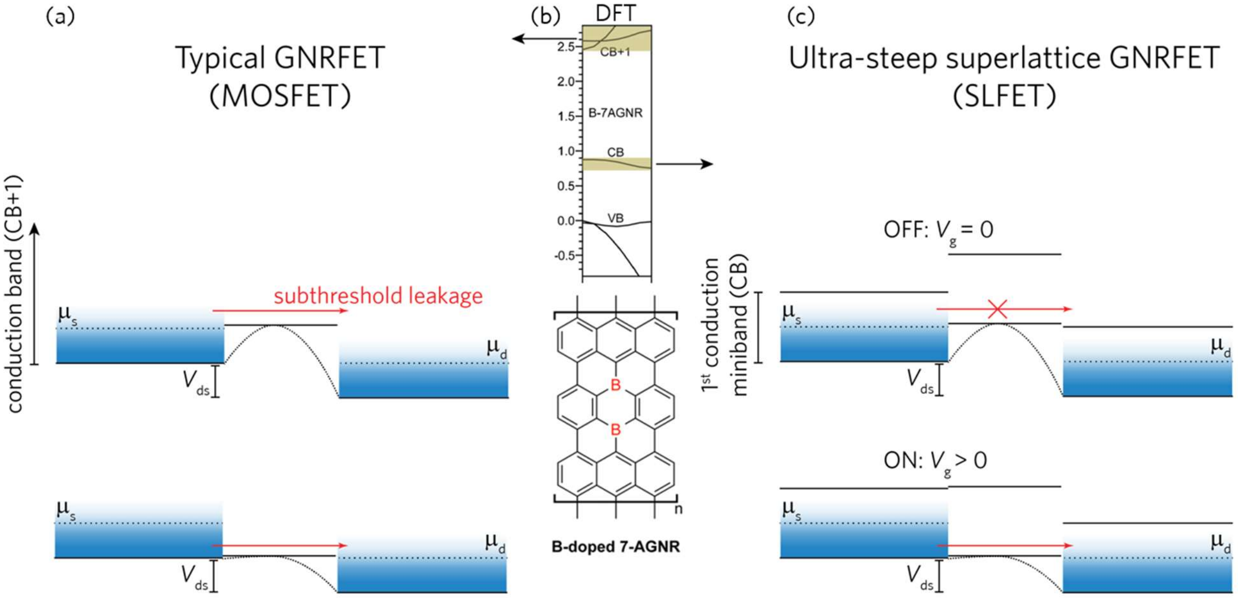

Figure 8.8 | Band diagrams of SL-GNRFET with B-doped 7AGNRs. (a) Band diagram of the MOSFET operation in the B-7AGNR, where transport occurs at the bulk 7AGNR bands. (b) DFT calculation of the band structure showing bulk 7AGNR bands with one narrow band mid-gap corresponding the B superlattice. (c) Band diagram of SL-FET operation, where transport occurs at the narrow super-lattice band near the Fermi level.

Note that if scattering and non-ideal band edges are considered, the subthreshold swing in the device will increase and the NDR will decrease. The effect of optical phonon scattering, for example, was shown to limit the subthreshold swing and NDR in NEGF calculations, although the subthreshold swing remains <60 mV/dec and quantitative effect of scattering on the swing must be confirmed experimentally.

The SL-GNRFET (SLFET) and standard GNRFET (MOSFET) transfer curves are calculated with (8.6) and shown in Figure 8.9. The curves are displayed up to 120 mV bias for both the drain and the gate to show devices under a technologically relevant low bias and to highlight the differences between the two systems. With a perfect gate efficiency, the MOSFET is limited in the switch slope (G vs V_g) by the Boltzmann limit of 60 mV/dec, as anticipated. The SLFET, in contrast, shows very sharp switch <60 mV/dec due to the leakage filtering occurring on the drain side. Finally, the $I_d - V_d$ curves for the MOSFET first show a linear region at low bias then plateau, approaching saturation. The SLFET shows a linear region and then peaks, leading to a region with NDR. The threshold voltage in the SLFET shifts towards zero as the drain bias is increased. This is similar to a common effect in short channel MOSFETs, drain induced barrier lowering (DIBL), that causes the threshold voltage to shift away from zero and is a parasitic effect in scaled logic systems. Unlike DIBL, the threshold shift in the SLFET depends on the voltage on the drain and not the electric field across the channel. That means the SLFET will not suffer from threshold voltage roll-off due to variations in the patterning of the channel length. It could still suffer from the standard DIBL at short channel lengths and perhaps the device could be engineered so that the threshold shift from the sharp switching and the DIBL balance out.

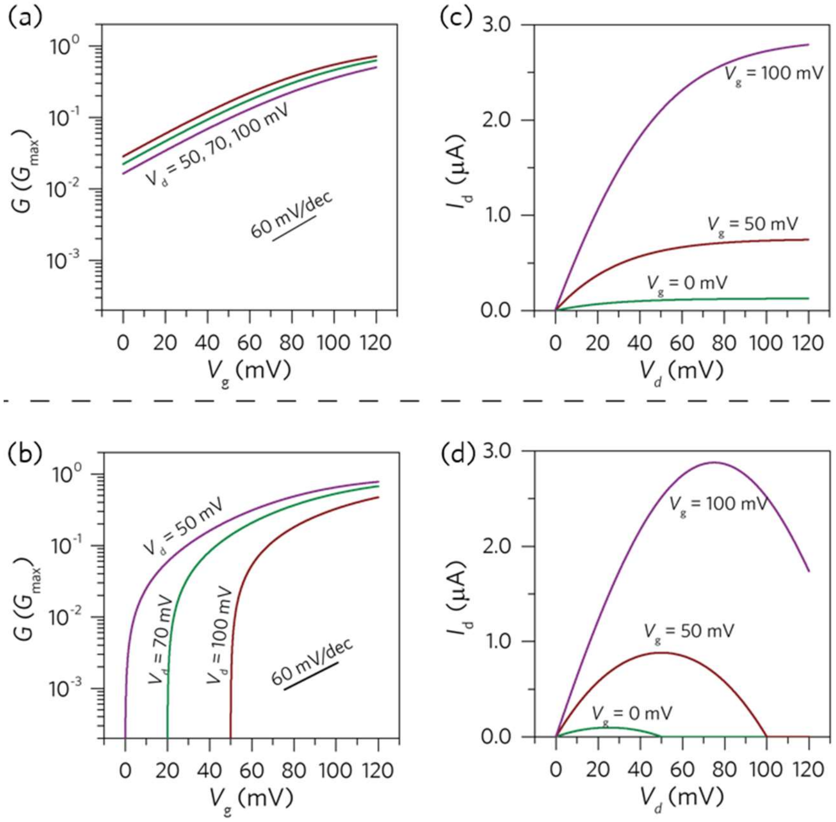

Figure 8.9 | Transfer characteristics of B-doped 7AGNR SL-FET from analytical model. MOSFET transfer curves (a,c) and SL-FET transfer curves (b,d). The MOSFET is limited by the 60 mV/dec switching despite the perfect gate efficiency. Sharp switching, negative DIBL, and NDR can be observed in the SL-FET.

While the steep switching characteristics of the SLFET are intriguing for overcoming the Boltzmann limit, both the NDR and threshold shift in the SLFET are undesired for classical CMOS logic integration, where the current ideally saturates at higher drain bias and the threshold voltage is independent on the drain bias. That is, a SL-FETs cannot be simply used to replace the transistors in a CMOS logic circuit without affecting the behavior or stability of the circuit. Regardless, logic designers may be able to design circuits that account for these effects and exploit the steep switching and NDR of the SLFET. Since the model given here is given in a closed form analytical solution, it is compact and can be used in circuit simulations. The simplest CMOS logic circuit, an inverter, was calculated with (8.6) and nodal analysis. Bistable behavior was observed which is not present in traditional CMOS inverters.

8.4 Bistable inverter with SL-GNR FETs

Two SLFETs are connected in a CMOS inverter configuration, shown in Figure 8.10, and the transfer curves of the circuit calculated by using the analytical transfer characteristics of the SL-FETs, (8.6). The calculated transfer curves are shown in Figure 8.10, where the output state of the circuit is tracked by the charge state of the load capacitor. A traditional CMOS inverter would show a single step transition from high V_{out} to low V_{out} at around $V_{DD}/2$. In SLFET inverter, the curve shows hysteretic behavior with a transition from when V_{in} is swept from zero to V_{DD} at 250 mV (5 $V_{DD}/6$) and a transition from V_{DD} to zero at 50 mV ($V_{DD}/6$).

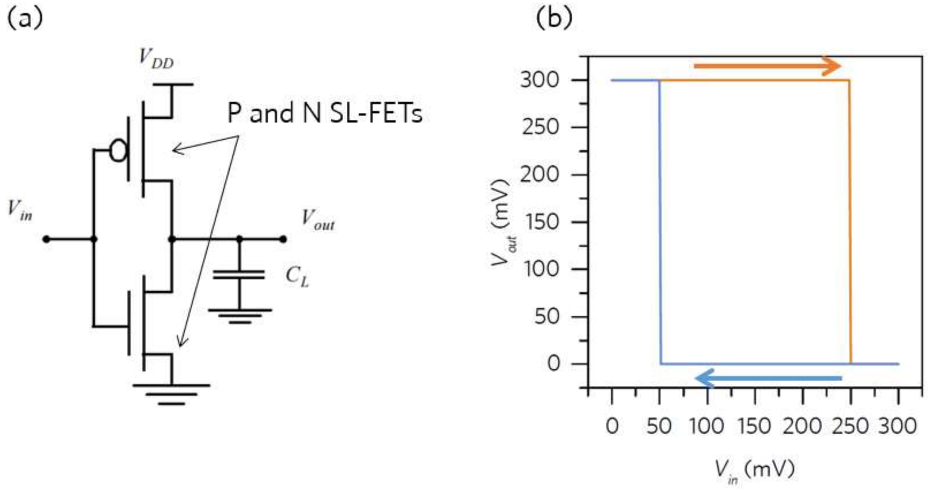

Figure 8.10 | SL-FET inverter transfer curves from compact model. (a) and (b)

In traditional logic design, the hysteretic behavior is detrimental to the noise margin, with the result that the SLFET inverter may not offer a big benefit to the traditional CMOS inverter despite its low V_{DD}. However, in the range of 50 mV to 250 mV, the circuit shows bistable behavior that can be exploited to make an oscillator or a SRAM cell with only two transistors. There is a lot of potential for circuit designers to create novel topologies that take advantage of the exotic SLFET properties. But, to realize these circuits requires experimental demonstration of the SLFET, which has been elusive so far.

8.5 Requirements for experimental demonstration of SL-GNR FETs

As shown in this chapter, the ideal SL-GNR has a band near the Fermi level that is few hundred meV wide. The band needs to be near mid-gap for minimizing SB effects and for isolation from neighboring bands that may affect the transport. A few GNRs have been synthesized with the required conditions: the boron doped GNR and some TE-GNRs such as the 7A-9A GNR super lattice. Both GNRs do not appear to be chemically stable enough to survive device fabrication, as discussed in Chapter 7, thus a new fabrication process or chemically stabilization method must be developed before SLFETs can be realized with these GNRs. On the other hand, cGNRs are chemically stable but the band gap is very wide (>3 eV), so large SB at the contacts prevent the observation of any SLFET behavior.

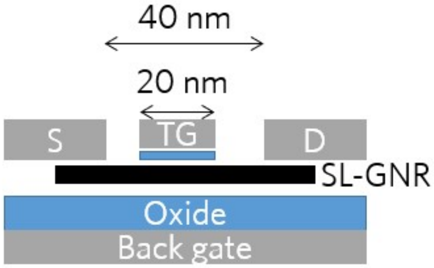

Figure 8.11 | SL-FET structure for experimentally demonstrating NDR and sharp switching. The SL-GNR has to be long enough to induce doped source-drain regions (gaps between SD electrodes and gate), with the back gate electrostatically doping the source and drain and the top gate modulating the channel.

Once a suitable, chemically stable GNR is found, it must be grown long enough to introduce doping into the GNR ends that will serve as the source and drain contacts in between the gate. This can be done by using a double gate structure shown in Figure 8.11, but requires long GNRs (>100 nm) for patterning and efficient electrostatic gating. The device shown with a suitable GNR with Ohmic contact could yield the desired SL-FET behavior.

8.6 Conclusion

Atomically precise heterojunctions are accessible in GNR synthesis by either co-deposition or rational design of a suitable precursor. The heterojunctions can be arranged to create quantum wells or super-lattice potentials that open minibands and minigaps in the band structure in SL-GNRs. Atomistic calculations on SL-GNR devices showed negative differential resistance (NDR) and steep, sub 60 mV/dec switching, which are both very attractive for circuit design. A closed form solution to a ballistic SL-FET was derived to understand and optimize the parameters in the device that affect transport. The model was then used to show that SL-FETs placed in a standard CMOS inverter configuration behave as bistable circuits which could be used as oscillators or memory cells. To experimentally demonstrate a SL-FET, a chemically stable SL-GNR with a narrow band gap (<1 eV) and moderate bandwidth (~200 meV) must be grown long enough (>100 nm) and integrated into a double gate device structure. The SL-GNRs and GNR heterostructures provide an intriguing platform for design and implementation of exotic electronic devices but more work must be done in the GNR synthesis and device fabrication to be able to realize SLFETs.

8.7 References

1. Avci, U. E., Morris, D. H. & Young, I. A. Tunnel Field-Effect Transistors: Prospects and Challenges. *IEEE Journal of the Electron Devices Society* **3,** 88–95 (2015). https://doi.org/10.1109/JEDS.2015.2390591
2. Sajjad, R. N., Chern, W., Hoyt, J. L. & Antoniadis, D. A. Trap Assisted Tunneling and Its Effect on Subthreshold Swing of Tunnel FETs. *IEEE Transactions on Electron Devices* **63,** 4380–4387 (2016). https://doi.org/10.1109/TED.2016.2603468
3. Chen, Y.-C., Cao, T., Chen, C., Pedramrazi, Z., Haberer, D., Oteyza, D. G. de, Fischer, F. R., Louie, S. G. & Crommie, M. F. Molecular bandgap engineering of bottom-up synthesized graphene nanoribbon heterojunctions. *Nat Nano* **10,** 156–160 (2015). https://doi.org/10.1038/nnano.2014.307
4. Cai, J., Pignedoli, C. A., Talirz, L., Ruffieux, P., Söde, H., Liang, L., Meunier, V., Berger, R., Li, R., Feng, X., Müllen, K. & Fasel, R. Graphene nanoribbon heterojunctions. *Nat Nano* **9,** 896–900 (2014). https://doi.org/10.1038/nnano.2014.184
5. Vo, T. H., Shekhirev, M., Kunkel, D. A., Morton, M. D., Berglund, E., Kong, L., Wilson, P. M., Dowben, P. A., Enders, A. & Sinitskii, A. Large-scale solution synthesis of narrow graphene nanoribbons. *Nat Commun* **5,** (2014). https://doi.org/10.1038/ncomms4189
6. Radocea, A., Sun, T., Vo, T. H., Sinitskii, A., Aluru, N. R. & Lyding, J. W. Solution-Synthesized Chevron Graphene Nanoribbons Exfoliated onto H:Si(100). *Nano Lett.* (2016). https://doi.org/10.1021/acs.nanolett.6b03709
7. Luisier, M., Lundstrom, M., Antoniadis, D. A. & Bokor, J. Ultimate device scaling: Intrinsic performance comparisons of carbon-based, InGaAs, and Si field-effect transistors for 5 nm gate length. in *Electron Devices Meeting (IEDM), 2011 IEEE International* 11.2.1-11.2.4 (2011). https://doi.org/10.1109/IEDM.2011.6131531
8. Smith, S., Llinás, J.-P., Bokor, J. & Salahuddin, S. Negative Differential Resistance and Steep Switching in Chevron Graphene Nanoribbon Field-Effect Transistors. *IEEE Electron Device Letters* **39,** 143–146 (2018). https://doi.org/10.1109/LED.2017.2772865
9. Landauer, R. Spatial Variation of Currents and Fields Due to Localized Scatterers in Metallic Conduction. *IBM Journal of Research and Development* **1,** 223–231 (1957). https://doi.org/10.1147/rd.13.0223

9 Conclusion

This dissertation demonstrates progress towards practical GNR electronic devices by studying the bottom-up growth, unique electronic structure, and charge transport of GNRs. An abundance of GNR types have been synthesized on metal surfaces and in solution. The key parameters in a successful GNR growth are summarized from the past decade of on-surface synthesis developments. Analysis of GNR electronic structure from experiments and theory details the source of discrepancy in the band gap values reported in literature and shows that the theoretical vacuum calculations with multi-body corrections give the most appropriate band structure calculation for electronic device design. Moreover, the GNR device fabrication strategy presented can be employed for a breadth of on-surface synthesized GNRs and other materials. The strategy was used to demonstrate the highest performance bottom-up GNR FETs to date, by integrating a 9AGNR with a thin, high-k local back gate structure into a FET. Integration of aligned GNRs into devices is also shown, but more data is needed to fully understand whether the pitch, transfer, or GNR heterogeneity is limiting the device performance. The path towards state-of-the-art logic FETs with GNRs is presented, requiring narrow band gap, long GNRs. Finally, the theoretical transport of novel, defect-free heterostructures shows that they can be used to create SL-FETs with exotic properties such as ultra-sharp switching and negative differential resistance.

While there is a path towards high performance logic circuits with GNRs presented here, more future work is required to realize GNR-based logic systems. Narrow band gap GNRs still need to be demonstrated that are chemically robust for device fabrication. More understanding of the aligned growth and transfer, which may require either longer GNRs or even shorter channel length FETs need to be developed. And, transport in super-lattice GNRs needs to be measured to confirm sharp switching and NDR.